To the Graduate Council:

I am submitting herewith a thesis written by Thomas Andreas Tietz entitled "Experimental Investigation of Flexible Wings." I have examined the final copy of this thesis for form and content and recommend that it be accepted in partial fulfillment of the requirements for the degree of Master of Science, with a major in Aerospace Engineering.

Jain-Ming Wu, Major Professor

We have read this thesis
and recommend its acceptance:

J C Reddy

Frank G. Collins

Accepted for the Council:

Vice Provost
and Dean of The Graduate School

STATEMENT OF PERMISSION TO USE

In presenting this thesis in partial fulfillment of the requirements for a Master's degree at The University of Tennessee, Knoxville, I agree that the Library shall make it available to borrowers under rules of the Library. Brief quotations from this thesis are allowable without special permission, provided that accurate acknowledgment of the source is made.

Permission for extensive quotation from or reproduction of this thesis may be granted by my major professor, or in his absence, by the Head of Interlibrary Services when, in the opinion of either, the proposed use of the material is for scholarly purposes. Any copying or use of the material in this thesis for financial gain shall not be allowed without my written permission.

Signature Thomas Tidh

Date March 5, 1986

EXPERIMENTAL INVESTIGATION OF FLEXIBLE WINGS

A Thesis

Presented for the

Master of Science

Degree

The University of Tennessee, Knoxville

Thomas Andreas Tietz

March 1986

ACKNOWLEDGMENTS

Special appreciation is expressed to Dr. Jain-Ming Wu, head of the Gasdynamics Division, advisor and committee chairman, for his guidance and support during this effort. He also deserves many thanks for his friendship and hospitality during the author's stay in America.

Sincere gratitude goes to Dr. Ahmad Vakili, Senior Research Engineer, for his advisement and time spent in overseeing the progress of this study.

The author is also indebted to Dr. Frank Collins, Professor of Aerospace Engineering, and Dr. K. C. Reddy, Professor of Mathematics, for their valuable assistance as committee members.

Appreciation is given to Mrs. Mary Lo, Librarian, for her special efforts in acquiring important articles pertinent to this study, and to Mrs. June Jarrell for her final preparation of the manuscript.

ABSTRACT

Various flexible wing models with different size, structure and profiles are investigated. The wing shapes of these models are based on a literature study taking into account aspects resulting from insect flight. The study was performed in a water tunnel and a low-speed wind tunnel to provide qualitative flow visualization to understand the flow physics and quantitative data to evaluate the performance of these various shapes. A four-component force balance was designed to measure aerodynamic forces on the wings in the wind tunnel tests. The wind tunnel free-stream velocity was in the range of 7.62 m/s to 10.7 m/s and the Reynolds number based on the root chord was $5.7 \cdot 10^4$ to $8 \cdot 10^4$.

The water tunnel tests gave incomplete results, whereas the force balance provided reasonably accurate measurements of the lift and drag values in the wind tunnel. The smoke visualization yielded flow patterns around the wing and in the wake. The flexible wing models showed a significant delay in stall at higher angles of attack. It is concluded that a pleated structure leads to improvements in the aerodynamic performance, and that the presence of unsteady effects leading to lift enhancement is a possibility. Finally, a comparison of

the performance of the various models with each other and with data available in the literature is presented.

TABLE OF CONTENTS

CHAPTER		PAGE
I.	INTRODUCTION	1
II.	EXPERIMENTAL DESCRIPTION	5
	Models	6
	Water Tunnel	16
	Wind Tunnel	19
	Wind Tunnel Description	19
	Smoke Generator	20
	Force Balance Description	22
III.	BALANCE DESIGN	25
	Force Balance	25
	Theoretical Description	25
	Design Details	36
	Mounting Support System	41
	Chuck Mounting	41
	Wing Mounting	42
	Balance Calibration	43
	Calibration Aids	43
	Theoretical Load Resolution Technique	44
	Actual Calibration	48
IV.	TESTING PROCEDURE	50
V.	RESULTS AND DISCUSSION	53
	Qualitative Testing	53
	Water Tunnel Testing	53

CHAPTER PAGE

V. (Continued)

Wind Tunnel Testing. 55

Measurements and Flow Visualization. 56

Model I (Flat Plate) 56

Model II 63

Model III. 67

Model IV and Model V 72

Comparative Evaluation 75

Comparison with the Literature Data. . . . 80

VI. COMMENTS AND CONCLUSIONS 84

BIBLIOGRAPHY 87

APPENDIXES 90

APPENDIX A. RESULTS OF MODEL I. 91

APPENDIX B. RESULTS OF MODEL II 98

APPENDIX C. RESULTS OF MODEL III. 104

APPENDIX D. RESULTS OF MODELS IV AND V. 112

VITA 119

LIST OF TABLES

TABLE PAGE

1. Lift Coefficient Gradient as a Function of the Reynolds Number 62

2. Aerodynamic Efficiency (c_L/c_D) at a Speed of 7.62 m/s (25 ft/s) 81

LIST OF FIGURES

FIGURE		PAGE
1.	Basic Wing Shape.	8
2.	Model D	11
3.	Model E	12
4.	Dragonfly Wing (from Reference [9])	13
5.	Model I through Model V	15
6.	Water Tunnel Facility (from Reference [14]) . .	17
7.	Smoke Generator	21
8.	Force Balance	23
9.	Schematic of the Test Setup	24
10.	Parts of the Force Balance.	26
11.	General Outline of the Force Balance.	27
12.	Forces and Moments.	28
13.	Coordinate System on Strain Gage Mounting Plates	30
14.	Strain Gage Locations	32
15.	Model Axes.	46
16.	Measured Lift of Model I at 7.62 m/s.	57
17.	Measured Drag of Model I at 7.62 m/s.	57
18.	Measured Efficiency of Model I at 7.62 m/s. . .	58
19.	Flow Field of Model I at $\alpha = 0°$	59
20.	Flow Field of Model I at $\alpha = 15°$.	59
21.	Measured Lift of Model II at 7.62 m/s	64
22.	Measured Drag of Model II at 7.62 m/s	64

FIGURE PAGE

23. Flow Field of Model II at $\alpha = 0°$. 65

24. Flow Field of Model II at $\alpha = 30°$ 65

25. Measured Lift of Model III at 7.62 m/s. 68

26. Measured Drag of Model III at 7.62 m/s. 68

27. Flow Field of Model III at $\alpha = 10°$. 69

28. Flow Field of Model III at $\alpha = 20°$. 69

29. Measured Lift of Model IV at 7.62 m/s 73

30. Measured Drag of Model IV at 7.62 m/s 73

31. Measured Lift of Model V at 7.62 m/s. 74

32. Measured Drag of Model V at 7.62 m/s. 74

33. Schematic Flow Field at an
Angle of Attack Around $\alpha = 0°$ 76

34. Schematic Flow Field at an
Angle of Attack Around $\alpha = 30°$. 76

35. Averaged Lift Coefficient
of Models I Through V at 7.62 m/s 79

A-1. Measured Lift of Model I at 9.1 m/s. 92

A-2. Measured Drag of Model I at 9.1 m/s. 92

A-3. Measured Efficiency of Model I at 9.1 m/s. . . 93

A-4. Measured Lift of Model I at 10.7 m/s 93

A-5. Measured Drag of Model I at 10.7 m/s 94

A-6. Measured Efficiency of Model I at 10.7 m/s . . 94

A-7. Flow Field of Model I. 95

B-1. Measured Lift of Model II at 9.1 m/s 99

B-2. Measured Drag of Model II at 9.1 m/s 99

FIGURE PAGE

B-3. Measured Lift of Model II at 10.7 m/s. 100

B-4. Measured Drag of Model II at 10.7 m/s. 100

B-5. Flow Field of Model II 101

C-1. Measured Lift of Model III at 9.1 m/s. 105

C-2. Measured Drag of Model III at 9.1 m/s. 105

C-3. Measured Lift of Model III at 10.7 m/s 106

C-4. Measured Drag of Model III at 10.7 m/s 106

C-5. Flow Field of Model III. 107

D-1. Measured Lift of Model IV at 9.1 m/s 113

D-2. Measured Drag of Model IV at 9.1 m/s 113

D-3. Measured Lift of Model IV at 10.7 m/s. 114

D-4. Measured Drag of Model IV at 10.7 m/s. 114

D-5. Flow Field of Model IV 115

D-6. Measured Lift of Model V at 9.1 m/s. 116

D-7. Measured Drag of Model V at 9.1 m/s. 116

D-8. Flow Field of Model V. 117

LIST OF SYMBOLS

General Symbols

a	Geometric parameter
A	Area
b	Geometric parameter
B	Width
c	Geometric parameter
c	Non-dimensional coefficient
C	Calibration matrix
d	Geometric parameter
F	Force
g	Component sensibility factor
H	Height
I	Moment of inertia
k	Influence coefficient
K	Normalized calibration coefficient
L	Length
L	Load matrix
M	Moment
R	Balance reading
t	Plate thickness
v	Velocity
x,y,z	Coordinates
α	Angle of incidence
Δ	Symbol indicating a difference

ρ	Density
σ	Stress

Subscripts

a	Surface index
b	Surface index
b	Bending index
D	Drag subscript
i	Channel index
j	Load index
L	Lift subscript
max	Maximal value index
N	Horizontal plate index
P	Pitching subscript
S	Side index
T	Index indicating a tangential term
tot	Total length index
u	Index characterizing an uncorrected quantity
W	Alternate term index
x,y	Indices characterizing the coordinate directions
Y	Yawing subscript
z	Index characterizing the coordinate direction
1N	First horizontal plate index
2N	Second horizontal plate index
1T	First vertical plate index
2T	Second vertical plate index

CHAPTER I

INTRODUCTION

In modern aircraft design, maneuverability and economy have become factors of prime importance. One of the main parameters which influences these factors is the *lift-to-drag* ratio. Various efforts have been made to improve this figure. It has been attempted to adapt the shape of both the profile and the wing to the different flight conditions (supercritical twisting, profiles, etc.). In all these cases, almost all the theoretical analyses were based on a *steady state* concept.

In order to obtain some new ideas about other innovative approaches, it seems to be justified to look more closely at the flight mechanisms which are used in nature, and which were developed over a long time through evolution, in order to get the best possible performance. Nachtigall [1][1] proved that the fur of a Petaurus breviceps papuamus acts as a lift generator within high angles of attack, a result which also was regarded as one means to improve the performance of soaring planes and gliders [2].

Despite the fact that animals and airplanes are usually operating under different conditions (for example,

---

[1]Numbers in brackets refer to similarly numbered references in the Bibliography.

the Reynolds number in animal flight is of a much smaller order than in technical aviation (cp. [3])), it is, however, still promising to examine certain flow patterns in order to gain a basic understanding. Maxworthy pointed out [4], referring to the Kasper-wing [5], that certain aerodynamic effects which can be observed in insect flight are already used in technical application. Due to the fact that insects show extraordinary performances in maneuvering, especially at high angles of attack, this group is of particular interest. In order to explain these performances, often the existence of *unsteady effects* has to be admitted. Weis-Fogh [6], for example, presented an explanation for the behavior of the chalcip wasp Encarsia formosa. Ellington [7] extended this idea insofar as he points out that, even if steady theory is able to present adequate results, the existence of unsteady effects cannot be excluded. Different hypotheses for the nonstationary aerodynamic forces are presented by Nachtigall [8]. Thus, insects seem to be an interesting group for the study of unsteady effects in lift generation. Due to the fact that certain species of the dragonfly operate at Reynolds numbers well above most insects (around $1.5 \cdot 10^4$ (cp. [9])) and due to their extraordinary flight performance (cp. [6] and [10]), the dragonfly seems to be especially suited for research purposes.

In the study of inextensible flexible airfoils, some work has been done recently by S. Greenshalgh, et al., in the wind tunnel of Princeton University (cp. [11] and [12]). Herein, the aerodynamic behavior of a flexible wing structure was investigated. It was possible to measure and calculate the lift and drag coefficients at various angles of attack for different wing shapes. Greenshalgh's observation that unsteady effects may be able to produce a lift enhancement without any apparent increase in drag deserves special interest. Furthermore, some of the presented results give rise to an assumption that a better performance at higher angles of attack can be achieved. Work recently performed by the U.S. Air Force supports these observations [13].

Based on these ideas, various models were built and tested in both the water tunnel and the low-speed wind tunnel of The University of Tennessee Space Institute (UTSI). After having improved the existing smoke generator, it was possible to carry out flow visualization tests. The main purpose of this flow visualization was an investigation of the flow pattern along the wing and in the wake. In order to get quantitative results, a four-component balance was designed and calibrated. Finally, the aerodynamic parameters (lift coefficient, drag coefficient) characterizing the various wing

configurations could be determined so that a comparison and evaluation was possible.

CHAPTER II

EXPERIMENTAL DESCRIPTION

Based on the promising results conducted by Greenshalgh [12], and based on the extraordinarily good flight behavior of some insect species, of which the dragonfly is of particular interest (cp. also Chapter I), the present work has been performed for the aerodynamic investigation of various flexible wing structures. Herein, the flight performances as well as the different flow field structures are determined and evaluated.

In order to accomplish this task, the water tunnel as well as the wind tunnel facilities of The University of Tennessee Space Institute (UTSI) were used.

Related to the problem, but limited by the facilities, various models were built as described below.

In order to examine the flow field, dye was used in the water tunnel, whereas smoke provided by a smoke generator was used in the wind tunnel. Furthermore, the test section of the latter facility had to be adapted to the specific requirements of the test.

A 35mm camera in connection with a flash unit was used for the documentation.

For the evaluation of the flight performance of the different models, the lift coefficients c_L as well as the drag coefficients c_D had to be determined. For this

purpose, a force balance measuring normal forces, side forces, pitching moments and yawing moments was designed. Since the design and calibration of this balance took an important part in this work, a detailed description is given in Chapter III. The data acquisition was accomplished by using a minicomputer, whereas the data reduction and data evaluation were done on the Vax 11/780 computer system belonging to UTSI.

Models

For the investigation in the testing facilities, two series of models were built. The first series, characterized by the letters A through G, were basically used in order to get qualitative results, whereas the models of the second series, characterized by the roman numerals I through V, were also used to obtain qualitative results in the form of lift and drag measurements. Since the tests carried out by Greenshalgh (cp. [11] and [12]) served as a starting point for this work, the basic geometric dimensions of all models were restricted by considerations of the geometric similarity. Furthermore, the maximal size of the models is limited by the dimensions of the facilities, so that the largest model is characterized by a span of 304.8mm (12 inches) and a root chord length of 111.7mm (4.4 inches). Since the insect flight should serve as another basis for this

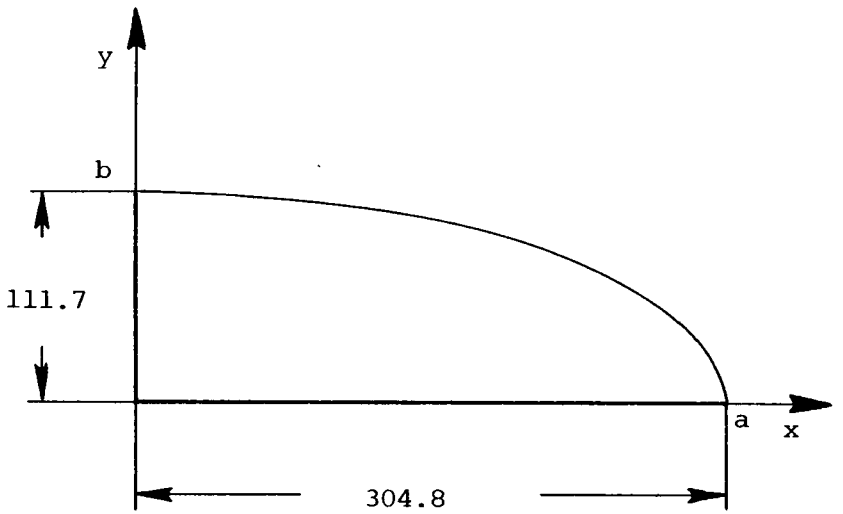
investigation, an elliptical shape was chosen (a wing shape), which seems to come closest to a variety of insects. Thus, the exact geometry of all wings could be calculated by using the following equation:

$$y = \sqrt{b^2 - \left(\frac{b}{a}\right)^2 \cdot x^2} \quad , \tag{2.1}$$

where b is the chord length measured at the root and a is the span of the wing. The coordinates x and y characterize the spanwise direction and chordwise direction, respectively. For the first four models of the first series (later referred to as Models A, B, C and D), the maximal possible values for a and b were chosen, so that the wing shape depicted in Figure 1 results.

Herein, for Model A, a solid rod having 6.35mm (0.25 inch) in diameter was chosen as material for the leading edge as well as for the chord, whereas aluminum foil was used to manufacture the wing planform.

For Model B, a fabric usually used for the design of umbrellas was chosen as wing material. This was necessary because this material combines the advantages of having a lower stiffness than aluminum and of being able to be used in wet surroundings. The leading edge spar was replaced by a tube having



x (mm)	y (mm)	x (mm)	y (mm)
0	111.7	230	73.3
50	110.1	250	63.9
100	105.5	270	51.8
150	97.2	290	34.4
170	92.7	300	19.7
190	87.3	304	8.1
210	80.9	304.8	0.0

Figure 1. Basic Wing Shape.

6.35mm (0.25 inch) in diameter, so that dye could be ejected through five drillings placed along the leading edge.

Model C is identical to Model A other than that the leading edge spar was made from a tube which had 4.76mm (0.1875 inch) in diameter and was pressed to dimensions of 5.6mm (0.22 inch) × 4.2mm (0.167 inch) so that the rate of vortex shedding caused by a leading edge having a circular cross-section could be reduced.

Model D is characterized by a leading edge made from a 4.76mm (0.1875 inch) stainless steel tube which was pressed to the same dimensions as Model C after a 2.38mm (0.938 inch) solid stainless steel rod had been inserted. As material for the wing planform, the same kind of fabrics used for Model B was used. Additionally, the upper wing surface was covered with three rows of tufts which were made from pieces of thread.

The last three models of the first series, referred to as Models E, F and G, were made from wood. The leading edge was in all cases hydrodynamically shaped and all models were painted so that they could be used in the water tunnel. Models E and F are characterized by a span a of a = 152.4mm (6 inches) and a chord length b of b = 55.8mm (2.2 inches), whereas Model G has a span of a = 76.2mm (3 inches) and a chord length of b = 27.9mm (1.1 inches). The wing planform of Model E was made from

the same material already used for Models B and D, whereas for the wing shape of Model F a plastic foil was chosen. Model G is characterized by a wing shape made from an extremely thin plastic foil. Since all models are characterized by a similar shape, only photographs of Model D (Figure 2) and Model E (Figure 3) are presented.

In order to obtain quantitative as well as qualitative results, the five models of the second series were built. All models are characterized by basic dimensions according to Figure 1. For the further design of the models, the wing of the dragonfly (cp. [9]) was used as a reference. This wing is presented in Figure 4. In order to come closest to the geometric relations of this wing, a 2.38mm (3/32-inch) solid stainless steel rod was chosen as basic material for the frame, consisting of the leading edge, trailing edge and eventually other bars. All models were reinforced from the root on by using a 4.76mm (0.1875 inch) outer diameter stainless steel tube with a wall thickness of 0.89mm (0.035 inch), which was pressed around the stainless steel rod so that a close fit could be guaranteed. Since the tube changed its form from a circular cross-section to an elliptical one, the drag coefficient produced by the rod could also be reduced. In order to make the models compatible with the balance mounting, a 6.35mm (0.25 inch)

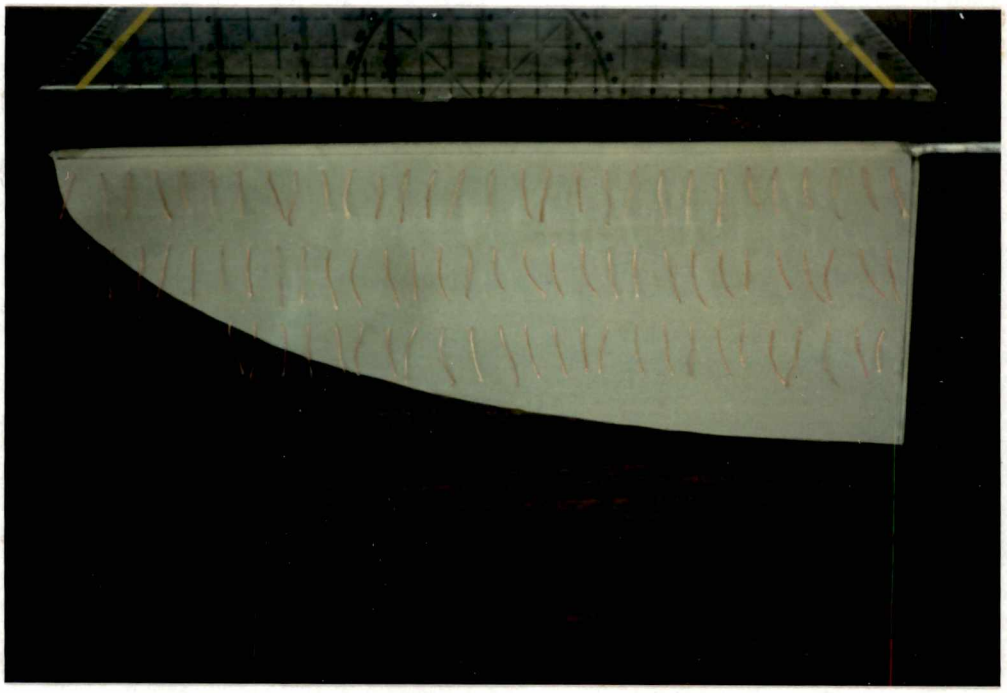


Figure 2. Model D.

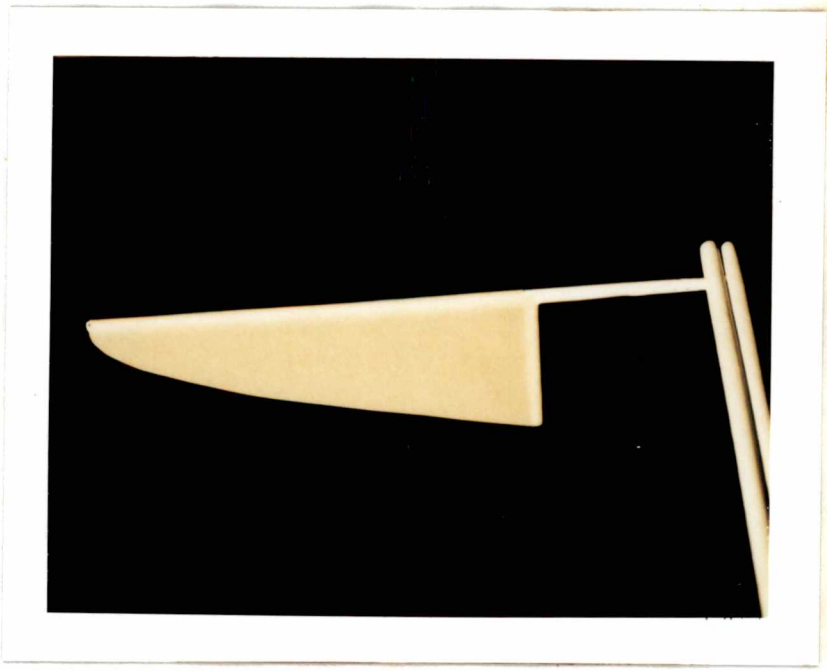


Figure 3. Model E.

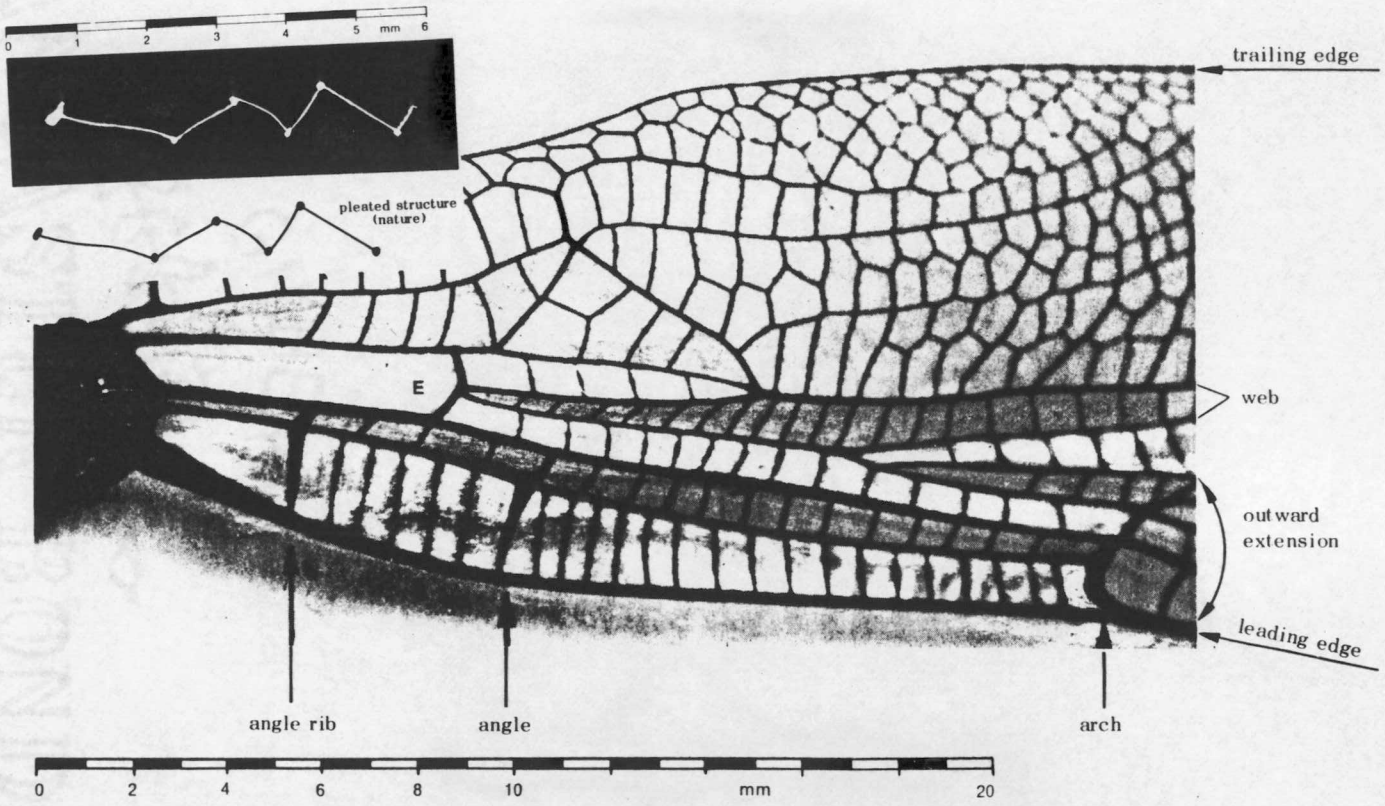


Figure 4. Dragonfly Wing (from Reference [9]).

tube was used, which gave the models an overall length of 508mm (20 inches).

The first model, referred to as Model I, is characterized by a flat plate made from aluminum used as material for the wing. The second model, referred to as Model II, is identical to Model I other than that black fabric was used as material for the wing.

Since, according to Reference [9], the dragonfly wing is not a flat wing but a pleated structure, three more models were built. For all these models, the same fabrics were used as wing material as for Model II. The first model, referred to as Model III, is characterized by one pleat, which is manufactured between the leading edge and the bar, built along the local c/3-line, where c stands for the chord of the wing. The depth of this pleat decreases almost linearly from 8mm at the root to nearly 1mm at the wing tip. The second model, referred to as Model IV, has two pleats between the c/3-line, whereas the third model, referred to as Model V, has three pleats between the c/2-line and the leading edge. This model comes closest to the dragonfly wing. All dimensions of these wings were chosen to be similar to those of the dragonfly and are presented in Figure 5.

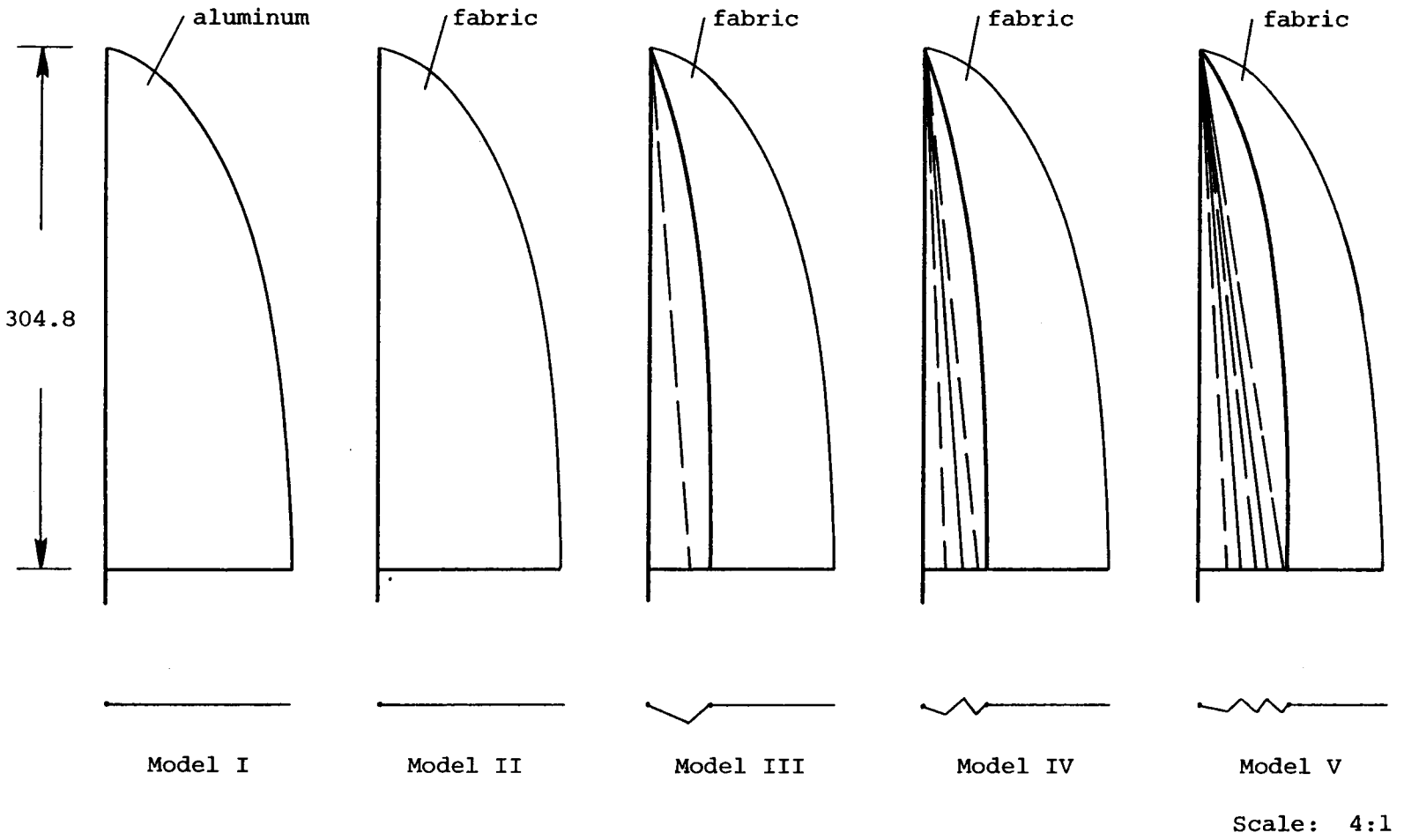


Figure 5. Model I through Model V.

Water Tunnel

All water tunnel tests were carried out in the water tunnel belonging to The University of Tennessee Space Institute (UTSI). This water tunnel, which is presented in Figure 6, is built as a closed circuit and has a test section measuring 305mm × 457mm × 1500mm in height, width and length, respectively. The walls of this test section are made from plexiglass, which allows for observations and taking of photographs during an ongoing test. Furthermore, the upper plexiglass plate can be removed so that the tunnel can be operated with both a closed and an open test section. The power for operating the tunnel is supplied by a 1 HP engine, which drives a two-bladed propeller measuring 250mm in diameter. Since this engine, which is placed at the second bend downstream of the test section, is connected to a continuously variable speed transmission, the water tunnel can be operated continuously between speeds of 2.5 cm/s and 50 cm/s or 25 cm/s, respectively. The first value is valid if a closed test section is used, and the second one is valid for the tunnel operating with an open test section. In both cases higher speed values can be realized, which, however, leads to a higher level of turbulence. If operating with an open test section, a then-occurring surface wave has also been taken into

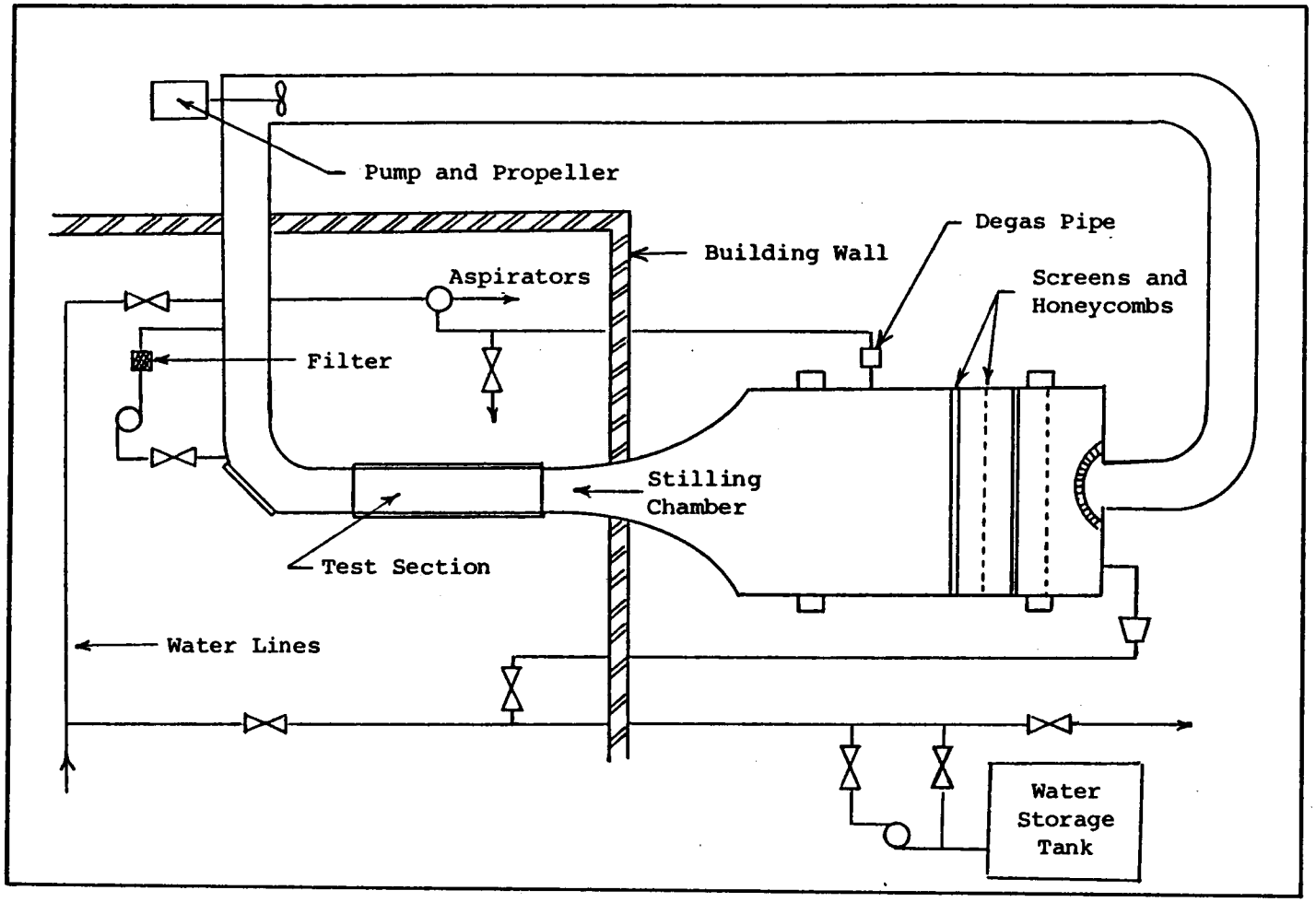


Figure 6. Water Tunnel Facility (from Reference [14]).

account. In order to damp the vibrations caused by the propeller, a long return pipe leading to a stilling chamber is provided. This stilling chamber measures 1.55m in diameter and 2.85m in length. It contains two aluminum honeycombs as well as four stainless steel screens. A bell mouth nozzle connects the circular stilling chamber to the rectangular test section. During the time between two tests, the water of the tunnel, which has a capacity of $7.93m^3$ (2100 gallons), can be stored in a $15.14m^3$ (4000 gallons) underground tank. In order to get the best possible test results, a portion of the main flow is bypassed through a woven propylene cartridge filter which filters water to 10 microns. Furthermore, the water is treated with chemicals to control its conductivity as well as to inhibit corrosion. The control of the tunnel is managed from a master control panel standing close to the test section. Herein, the water speed is measured with an 8mm pitot-static tube meter, which is connected to a pressure transducer having an accuracy of 1.9×10^{-5} psid. A thermocouple measures the water temperature.

In the present series of tests, the open test section was used in order to facilitate the mounting of the models. Furthermore, dye made from a neutrally buoyant mixture of milk, food coloring and alcohol could be injected under pressure from tubes placed in the flow.

Wind Tunnel

Wind Tunnel Description

All wind tunnel tests were carried out at the low-speed wind tunnel belonging to The University of Tennessee Space Institute (UTSI). This wind tunnel can be operated continuously and is built as an open circuit, with an inlet nozzle which is characterized by a contraction ratio of 13:1. Furthermore, it has a closed test section measuring 356mm × 501mm × 1070mm in height, width and length, respectively. A plexiglass window on one side allows observations of the model and the flow field during an ongoing test. In order to improve the illumination during the flow visualization tests, the top of the test section has been provided with a plexiglass window, which measures 114.3mm (4.5 inches) × 304.8mm (12 inches) and is located 686mm (27 inches) away from the beginning of the test section. Moreover, the side walls of this test section were blackened with velvet so that a good contrast for the flow visualization could be provided. The power is applied through a fan, which is driven by an electrical engine so that velocities from 6.1 m/s (20 ft/s) to 20 m/s (66 ft/s) can be realized. The velocities are measured by a meter, which is connected to a pitot tube as well as to a static pressure tap, and which operates within an accuracy of ±5%. In order to determine the

air density, a thermometer and a barometric pressure gage were used. The models or the force balance, respectively, were mounted on a chuck, which allows the realization of angles of attack between +90° and -90° within an accuracy of ±0.25'. The data acquisition was accomplished by using a minicomputer which had been designed for use in the wind tunnel. This computer consists of an amplifier followed by an A/D converter which is characterized by an averaging rate of 81 Hertz.

Smoke Generator

The smoke generator used at the low-speed wind tunnel is a modified version of the smoke generator which was designed earlier at The University of Notre Dame. This modified smoke generator is presented in Figure 7 and consists of the following major parts: an oiler with kerosene drip control, a strip heater on which the dripping kerosene is vaporized, a heat exchanger which cools the kerosene vapor to the tunnel temperature, a filter to remove large droplets before the smoke is introduced to the tunnel and a hose to introduce the smoke into the tunnel. Moreover, control valves, an air entrance blower and the necessary electrical controls are provided. The entire generator stands on wheels in order to improve mobility. The generator was made



Figure 7. Smoke Generator.

mainly from stainless steel and copper, and was manufactured by silver soldering and heli-arc welding.

In order to get better results during the flow visualization tests, part of the heat exchanger was insulated with glass fiber wool, since it turned out that a large portion of smoke was already condensed before entering the tunnel. To remove condensed kerosene, drain screws were provided in the second and fourth bends of the heat exchanger. Furthermore, the original 6.35mm (0.25 inch) hose was replaced by a 12.7mm (0.5 inch) one.

Force Balance Description

For the wind tunnel measurements, a four-component force balance was used. This balance, presented in Figure 8, has an overall length of 140mm (5.512 inches), where the connection parts for the other mounting systems measure 11.43mm (0.45 inch) and 14.3mm (0.562 inch), respectively. The outer diameter of the balance measures 12.7mm (0.5 inch). The inner part of the balance is divided into sections of equal length, consisting of two vertical planes, two horizontal planes and five cylindrical connection parts. Each of these planes has a thickness of 3.5mm and is equipped with one complete Wheatstone bridge providing the output for each channel.

A complete test setup is presented in Figure 9.

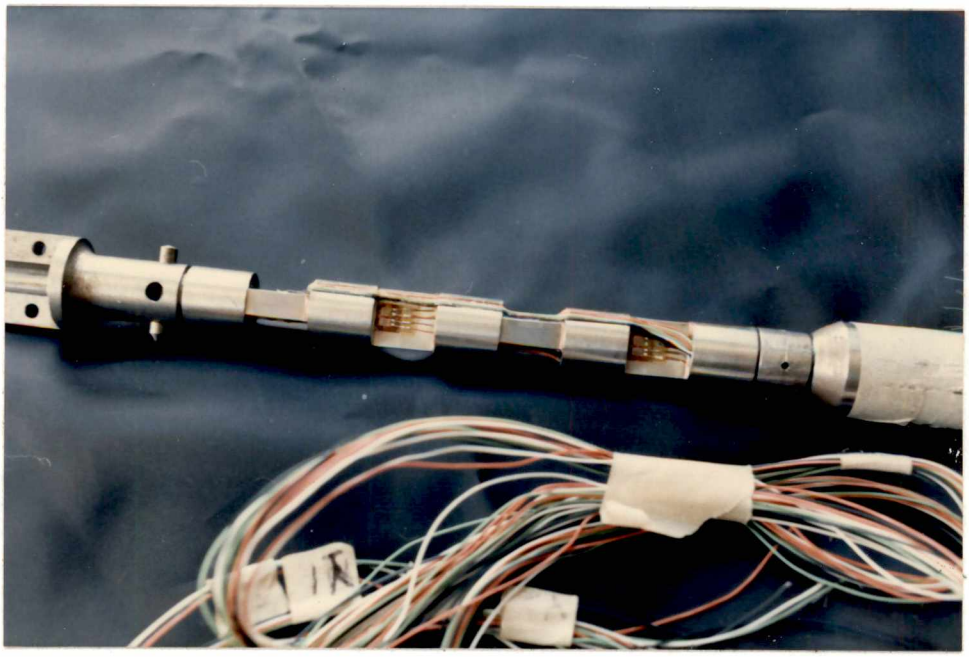


Figure 8. Force Balance.

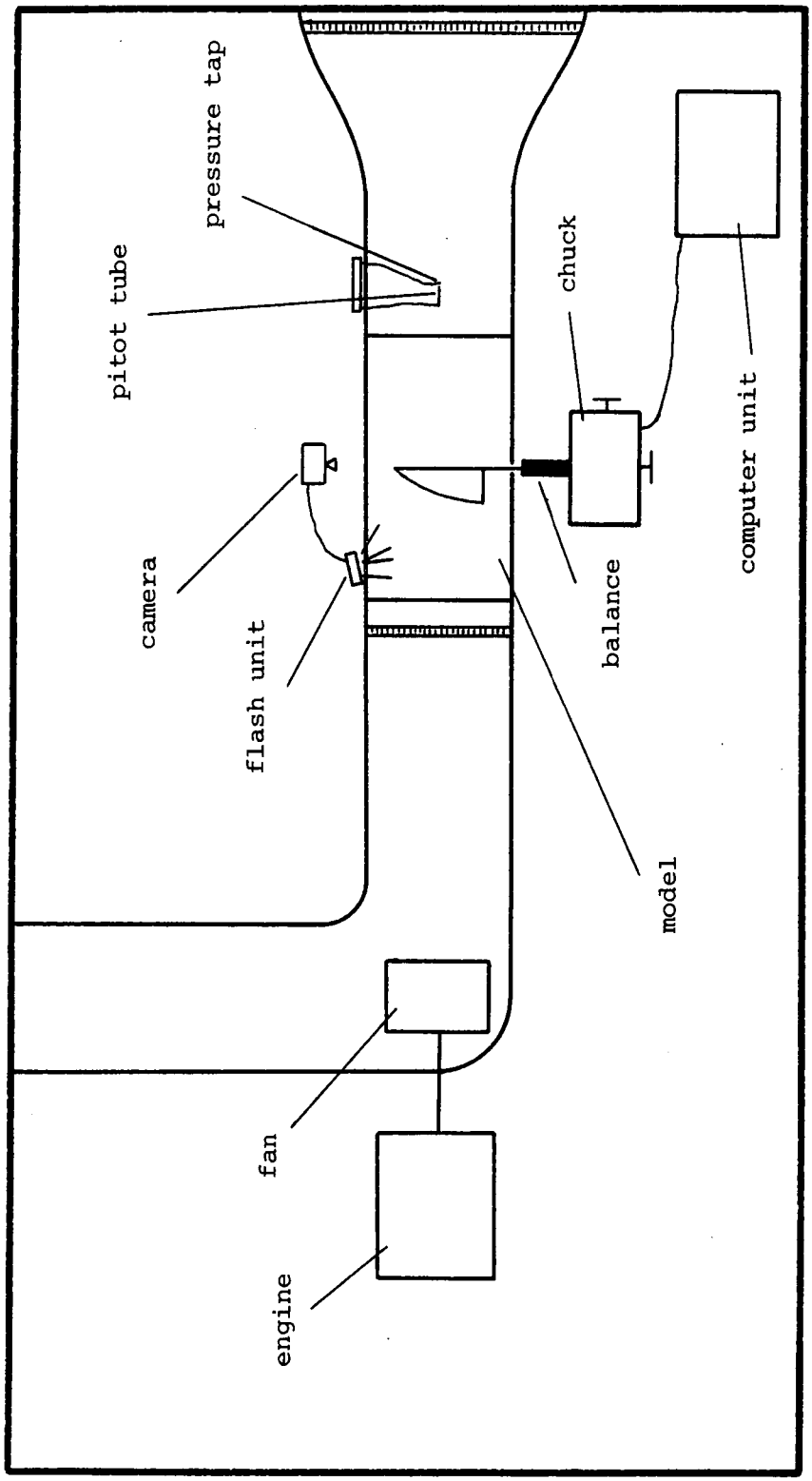


Figure 9. Schematic of the Test Setup.

CHAPTER III

BALANCE DESIGN

Force Balance

Theoretical Description

Since one task of this work was the performance evaluation of the different wing configurations, a four-component balance had to be designed. All parts of the uninstrumented force balance are depicted in Figure 10.

A cantilever balance equipped with strain gages seemed to fit this purpose best. The strain gages were glued on four plates so that the components of the resulting force, as well as its location, could be determined. A general outline of the balance is shown in Figure 11.

The specific dimensions of the balance are based on the following calculation. The first step is the determination of the cutting forces. Since these forces are similar in both planes (x,y) and (y,z), only a presentation for the vertical direction is given. The forces and moments existing along the cantilever beam as well as the sign convention are given in Figure 12. These cutting forces cause bending and shear stresses. The shear stresses could originate either from shearing forces or from torsion. Since the strain gages are

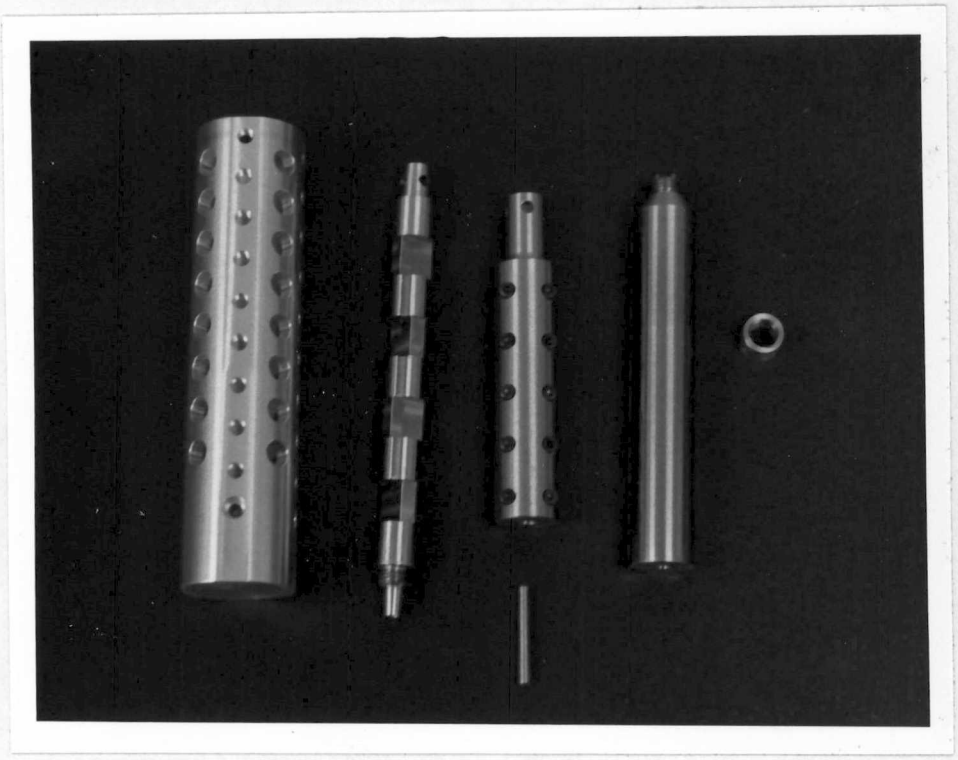


Figure 10. Parts of the Force Balance.

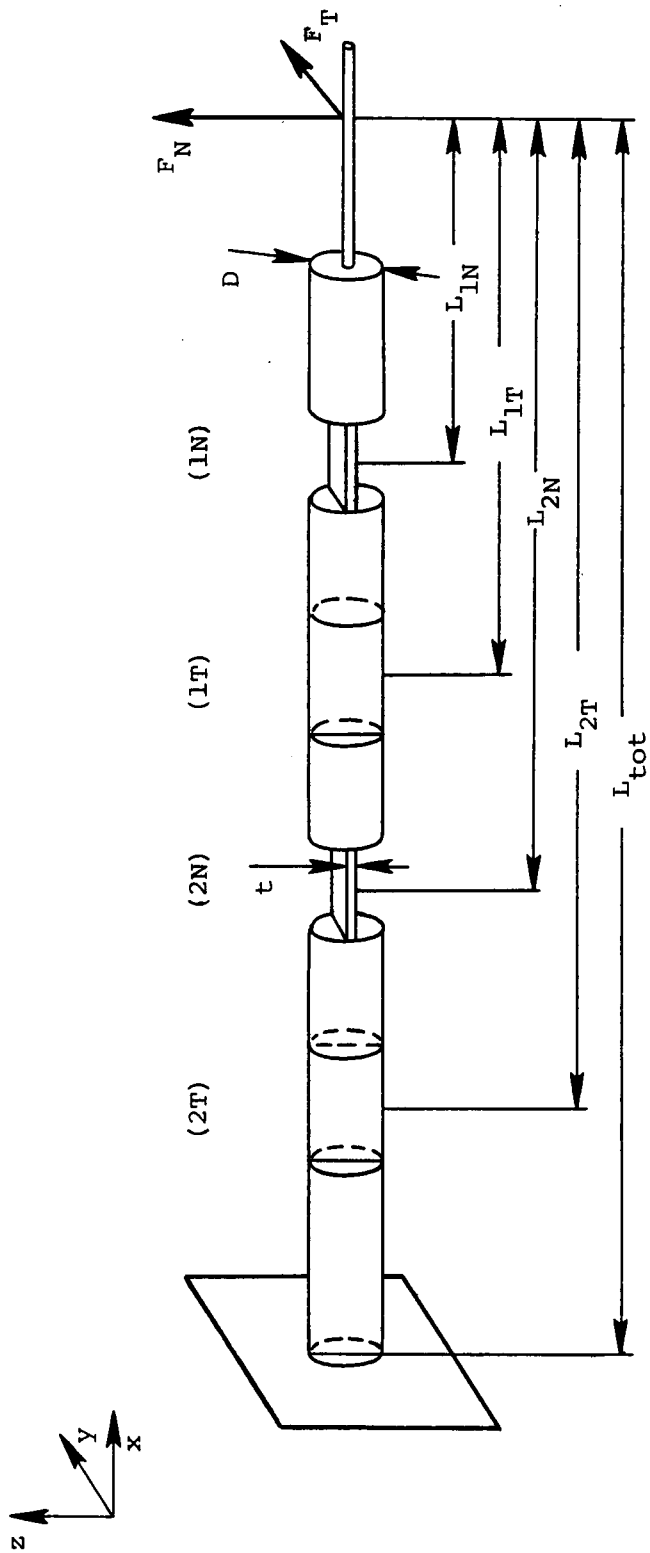
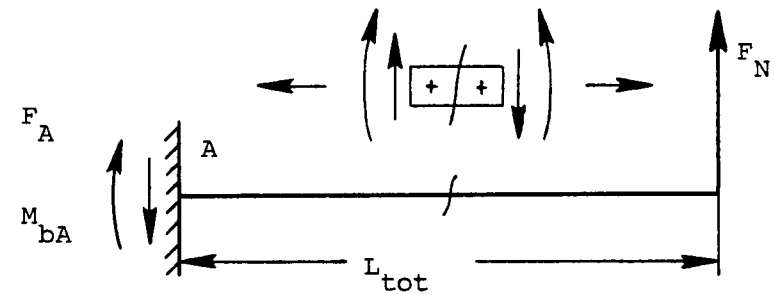
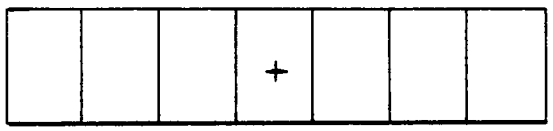


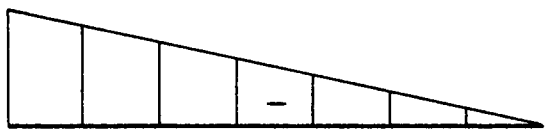
Figure 11. General Outline of the Force Balance.



Force:



Moment:



$$M_{bmax} = F_N \cdot L_{tot}$$

Figure 12. Forces and Moments.

mounted on top of each surface, the shear stresses caused by shearing forces do not have to be considered. The shear stresses due to the torsion can be neglected since their influence on the strain gages is small because of their direction and magnitude. Thus, only the bending stresses have to be considered. These stresses can be described by the relationship:

$$\sigma_{by} = \frac{M_b}{I} \cdot y \qquad (3.1a)$$

and

$$\sigma_{bz} = \frac{M_b}{I} \cdot z \ , \qquad (3.1b)$$

where M_b is the bending moment (cp. Figure 12), I is the corresponding moment of inertia, and y and z are the coordinates passing through the center of gravity and pointing in the horizontal or vertical direction, respectively (cf. Figure 13). Figure 13 also presents the values on which the moment of inertia depends, according to:

$$I_{y_N} = \frac{B_N \cdot H_N^3}{12} \qquad (3.2a)$$

and

$$I_{y_T} = \frac{B_T \cdot H_T^3}{12} \ . \qquad (3.2b)$$

Next, the equations describing the stresses in the vertical planes (1N) and (2N) (cf. Figure 11) are developed. These planes are supposed to indicate

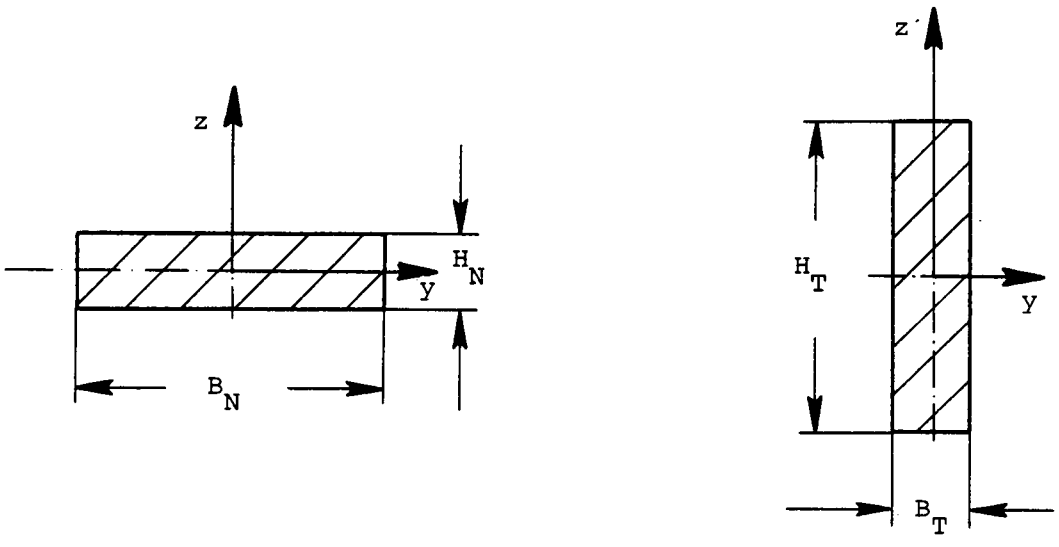


Figure 13. Coordinate System on Strain Gage Mounting Plates.

the normal forces. Combining the Equations (3.1) and (3.2) yields for the plane (1N):

$$\sigma_{b1N} = \frac{6 \cdot F_N \cdot L_{1N}}{B_N \cdot H_N^2} + 12 \cdot \frac{F_T \cdot L_{1N}}{H_N \cdot B_N^3} \cdot y \quad , \qquad (3.3)$$

where the facts are used that the stresses caused by the normal force F_N are constant along both the upper and lower surface, and that stresses pointing in the same direction can be linearly superposed. Taking into account the different signs for both surfaces, one gets for the upper surface which is characterized by the letter "a":

$$\sigma_{b1N_a} = - \frac{6\ F_N \cdot L_{1N}}{B_N \cdot H_N^2} - 12 \cdot \frac{F_T \cdot L_{1N}}{H_N \cdot B_N^3} \cdot y_{1N_a} \quad , \qquad (3.4a)$$

as well as for the lower surface, characterized by the letter "b":

$$\sigma_{b1N_b} = \frac{F_N \cdot L_{1N}}{B_N \cdot H_N^2} - 12 \cdot \frac{F_T \cdot L_{1N}}{H_N \cdot B_N^3} \cdot y_{1N_b} \quad . \qquad (3.4b)$$

The coordinates y_{1N_a} and y_{1N_b} are defined in Figure 14. Using the abbreviation:

$$y_{1N} = y_{1N_a} - y_{1N_b} \qquad (3.5)$$

in connection with Equation (3.4) gives the relationship:

$$y_{1N} = - \frac{H_N \cdot B_N^3}{12\ F_T \cdot L_{1N}} \left(\sigma_{b1N_a} - \sigma_{b1N_b} + \frac{12 \cdot F_N \cdot L_{1N}}{B_N \cdot H_N^2} \right) . \qquad (3.6)$$

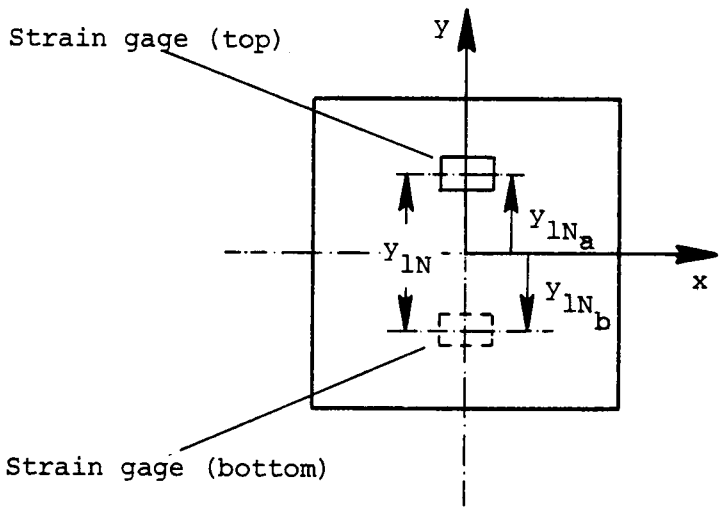


Figure 14. Strain Gage Locations.

The development of relationships similar to the Equations (3.4) and (3.5) for the plane (2N) leads to:

$$y_{2N} = - \frac{H_N \cdot B_N^3}{12 \cdot F_T \cdot L_{2N}} \cdot \left(\sigma_{2N_a} - \sigma_{2N_b} + 12 \frac{F_N \cdot L_{2N}}{B_N \cdot H_N^3} \right) . \qquad (3.7)$$

Taking into account the geometric relationship:

$$L_N = L_{2N} - L_{1N} \quad , \qquad (3.8)$$

the Equations (3.6) and (3.7) can be combined to obtain:

$$- \frac{L_N}{a} = \frac{\Delta \sigma_{1N}}{y_{1N} \cdot F_T + b \cdot F_N} - \frac{\Delta \sigma_{2N}}{y_{2N} \cdot F_T + b \cdot F_N} \quad . \qquad (3.9)$$

Herein, the following abbreviations were used for the geometric parameters:

$$a = \frac{H_N \cdot B_N^3}{12} \qquad (3.10a)$$

and

$$b = \frac{H_N \cdot B_N^3}{B_N \cdot H_N^2} = \frac{B_N^2}{H_N} \quad , \qquad (3.10b)$$

and for the stress parameters:

$$\Delta \sigma_{1N} = \sigma_{b1N_a} - \sigma_{b1N_b} \qquad (3.11a)$$

and

$$\Delta \sigma_{2N} = \sigma_{b2N_a} - \sigma_{b2N_b} \quad . \qquad (3.11b)$$

Following the same procedure used for the planes (1N) and (2N), the stresses of the planes (1T) and (2T), which are indications for the side forces, can be described by:

$$\sigma_{b1T} = \frac{6 \cdot F_T \cdot L_{1T}}{H_T \cdot B_T^{\,2}} + 12 \frac{F_N \cdot L_{1T}}{B_T \cdot H_T^{\,3}} \cdot z \quad , \tag{3.12}$$

which leads to:

$$- \frac{L_T}{c} = \frac{\Delta\sigma_{1T}}{z_{1T} \cdot F_N + d \cdot F_T} - \frac{\Delta\sigma_{2T}}{z_{2T} \cdot F_N + d \cdot F_T} \quad . \tag{3.13}$$

The values for "c" and "d" are given by:

$$c = \frac{B_T \cdot H_T^{\,3}}{12} \tag{3.14a}$$

and

$$d = \frac{B_T \cdot H_T^{\,3}}{H_T \cdot B_T^{\,2}} = \frac{H_T^{\,2}}{B_T} \quad . \tag{3.14b}$$

The new symbols are defined analogous to those already used in Equation (3.9).

In the following, the assumptions were made that $y_{1N} = y_{2N} = 0$ and $z_{1T} = z_{2T} = 0$. Physically, this does not only require that the distance from the strain gages to each other is the same on both planes (1N) and (2N) or (1T) and (2T), respectively, but also that the strain gages are located opposite each other on the corresponding plates.

After rearranging Equations (3.9) and (3.13), this leads to the following relationships:

$$F_N = \frac{a}{b}\left(\frac{\Delta\sigma_{1N} - \Delta\sigma_{2N}}{L_N}\right) \quad ; \tag{3.15}$$

$$F_T = \frac{c}{a}\left(\frac{\Delta\sigma_{1T} - \Delta\sigma_{2T}}{L_T}\right) \quad . \tag{3.16}$$

This assumption seems to be justified insofar as the purpose of this calculation is to get a lead for the actual design parameters and not to calculate the actually existing forces, a task which has to be accomplished by using a calibration process.

Realizing the fact that the height or the width of the plates is identical to the diameter D of the balance and assuming that the thickness t of the plates should remain constant along the balance leads to the identities:

$$B_N = H_T = D \tag{3.17a}$$

and

$$B_T = H_N = t \quad . \tag{3.17b}$$

Combining these equations with the definitions (3.10) and (3.14) yields the final relationship for the forces F_N and F_T :

$$F_N = \frac{D \cdot t^2}{12} \cdot \left(\frac{\Delta\sigma_{1N} - \Delta\sigma_{2N}}{L_N}\right) \quad ; \tag{3.18}$$

$$F_T = \frac{D \cdot t^2}{12} \cdot \left(\frac{\Delta\sigma_{1T} - \Delta\sigma_{2T}}{L_T} \right) \quad . \quad (3.19)$$

Design Details

The most crucial parameter during the design process is the plate thickness t. This thickness is mainly determined by the fact that the maximum stress applied on the strain gages should be around 103 N/mm^2 (15000 psia). These stresses are represented by the Equations (3.3) and (3.12) which are valid for the plates (1N) and (1T). Similar equations hold for the plates (2N) and (2T).

The normal force F_N, the maximum value of which results in maximal stresses, can be approximated by the aerodynamic relationship:

$$F_{N_{max}} = \frac{\rho}{2} \cdot v_{max}^2 \cdot A \cdot c_{L_{max}} \quad , \quad (3.20)$$

where v_{max} is the speed in the test section, ρ is the corresponding density, A is the area of the wing and $c_{L_{max}}$ is the highest expected lift coefficient. The air density can be determined within this speed range from the ideal gas equation, which leads to a value of $\rho = 1.17\ kg/m^3$ if a temperature of 298.15K and atmospheric pressure are assumed. Since the velocity v_{max} is limited

by the wind tunnel facility to approximately 20 m/s , the maximum dynamic pressure q_{max} is limited by a value of $q_{max} \approx 240\ N/m^2$. Due to the fact that all models have an elliptically shaped wing, the area A can be determined by using the relationship:

$$A = 0.25\pi \cdot a \cdot b \quad , \tag{3.21}$$

where a is the length of the major axis and b is the magnitude of the minor axis of the ellipse. Maximum values of a = 304.8mm (12 inches) and b = 111.8mm (4.4 inches) lead to an area of $A = 2.67 \cdot 10^{-2} m^2$ (cp. also Chapter II). A good approximation for the maximum lift coefficient $c_{L_{max}}$ seems to be a value of $c_{L_{max}} = 1.2$. Thus a force of $F_{N_{max}} \approx 8_N$ can be regarded as the maximum normal force. The maximal side force $F_{S_{max}}$ can be approximated by assuming a common value for the aerodynamic efficiency c_L/c_D . Using a value of $c_L/c_D = 8$ results in a side force of $F_T = 1N$.

For the determination of the geometric dimensions L_{1N} , L_{2N} , L_{1T} and L_{2T} , the exact position of the resultant aerodynamic force should be known. Due to the lack of a theory to determine that position, the assumption was

made that the position of the aerodynamic force in spanwise direction is close to the centroid of the wing planform. This coordinate could be described by:

$$x_s = \frac{1}{A} \cdot \frac{b}{a} \cdot \int_0^a x \cdot \sqrt{a^2 - x^2}\, dx \quad , \qquad (3.22)$$

where x_s is the distance between the centroid and the root of the wing. Integration leads to a value of $x_s = 0.424 \cdot a$ or $x_s = 129.3$mm (5.09 inches). The wind tunnel facility requires a displacement of 38mm (1.5 inches) between the root of the wing and the mounting support system. Furthermore, a length of 101.6mm (4 inches) is necessary for the mounting support system to guarantee a fixed position of the wing. Thus, a value of $L_{1N} = 288$mm (11.34 inches) can be calculated. Herein, the various plates of the force balance are not only chosen to be equally spaced at a distance D, but also to have the same length D. Using these dimensions results in values of $L_{1T} = 313.5$mm (12.34 inches), $L_{2N} = 339$mm (13.34 inches) and $L_{2T} = 364.3$mm (14.34 inches).

As one can easily verify, the maximum stresses occur at the position (2N), so that only

this plate has to be considered during the design procedure. Applying the relationship (3.3) for the present case leads to a value of:

$$t = 3.5\text{mm } (0.138 \text{ in.}) \quad . \tag{3.23}$$

Thus, the basic dimensions of the balance are given by a length of 114.3mm (4.5 inches), a diameter of 12.7mm (0.5 inch) and a plate thickness of 3.5mm (0.138 inch). It is important to realize that the choice of the values for the diameter D and the plate thickness t determines the quality of the balance, since the response of this balance to load interactions is dependent on the thickness-to-height ratio of the plates.

Next, it is necessary to verify that a balance having these dimensions is able to withstand the occurring loads. Since it is expected that the models to be tested in the wind tunnel are going to vibrate, the effects of dynamic loading have to be considered. Usually, no additional static load will be superimposed so that all the occurring loads contribute directly to the dynamic stresses. Consequently, the value describing the influence of the alternate stresses is the parameter which characterizes the upper load limit (cp. also Smith or Haigh diagram). In the present case the maximum stresses occur at the outer edges of the various

plates, i.e., at the coordinates $y = 0.5 \cdot D$ or $z = 0.5 \cdot D$, respectively. Since only the plate which carries the maximum load is of interest, again the plate (2N) has to be considered. Applying Equation (3.3) yields a maximum stress value of $\sigma_{2N_{max}} = 107$ N/mm^2 (15000 psia). The maximal allowable alternate stress value characterizing the steel AISI 316L which was used for the balance is given by $\sigma_W = 209$ N/mm^2 (30320 psia). Thus, the condition $\sigma_W \gg \sigma_{2N_{max}}$ is fulfilled with a safety factor of 1.95.

In order to be able to use the balance for various purposes, connection parts have to be supplied at both ends of the balance. In the present case, the balance has to be connected to a mounting chuck as well as to the models to be tested. In order to enable the connection to the mounting chuck, one side of the balance was designed as a right-hand threaded cone with four longitudinal grooves placed around the cone at 90° intervals to guarantee a close fit to the next part. The specific dimensions of this cone are identical to those of the cone of an earlier-designed balance to assure interchangeability. For wiring purposes, several holes had to be drilled in the longitudinal direction.

For the connection to the mounting part holding the models, a tapered cone having a length of 11.43mm (0.45 inch) was chosen for the other end of the balance.

This cone was manufactured with two holes lying normal to the centerline, perpendicular to each other. Therefore, the mounting can be turned without changing the position of the balance. It is important to realize that all connections must not allow for any play between the various parts, since, otherwise, all measurements could be falsified.

Finally, the balance was equipped with 16 strain gages. Two strain gages were mounted on top of each plate surface so that each plate is equipped with one complete Wheatstone bridge circuit, which allows the data acquisition on four different channels.

Mounting Support System

Chuck Mounting

The main part of this mounting is a left-hand threaded portion which is characterized by four tapered pins designed in a way that they fit exactly into the four grooves in the corresponding part of the balance. Since this corresponding part has a slightly tapered cone, the inner section of the mounting also has to be tapered in order to contribute to the stiffness of the connection. To provide for a proper fit to the chuck, the rest of the mounting basically consists of a solid rod having 19mm (0.75 inch) in diameter. A hole at the centerline allows for wire connections needed for the strain gages.

The overall length of the chuck mounting is 122.48mm (4.822 inches).

A nut provides the actual connection between the balance and the chuck mounting. Due to the fact that this nut has both an internal left-handed thread and an internal right-handed thread, a close fit can be easily achieved by tightening.

Wing Mounting

The wing mounting system basically consists of an upper and a lower part.

The upper part can be divided into two regions, where the first region serves as a counterpart to the balance. Therefore, this region has a tapered drilling which corresponds to the tapered cone of the balance, as well as two holes which are placed in the extension of those belonging to the balance. A tapered pin serves as the connection piece. The tapered cone is characterized by a ratio of 20:1.

The second region serves, together with the lower part, as mounting for the various models. Since the extension of all models consists of a tube having a diameter of 6.35mm (0.25 inch), both of these parts together provide a drilling of the same size. A small slot which exists between both parts after having inserted the model, in connection with 10 screws which

are placed within two parallel rows, enables a close fit between all parts. In order to obtain repeatable conditions for each test, each model is equipped with a pin. This pin fits exactly into a hole, which is placed perpendicular to the main drilling and which crosses the fictional centerline of both parts.

The mounting system has an overall length of 101.6mm (4 inches).

Balance Calibration

Calibration Aids

Since during the calibration procedure loads have to be applied to the balance at different positions and in various planes, a special calibration unit had to be designed. Since this calibration unit should allow the application of these loads, this unit mainly has to fulfill two requirements: First, it has to be light so that the direct influence on the balance remains small. Secondly, every play between the calibration unit and the balance has to be avoided so that the load which is applied to the calibration unit can be completely transferred to the balance.

For the actual design, an aluminum pipe with a length of 140mm (5.5 inches) was chosen so that the full length of the balance could be covered. In order to fulfill the second condition, a solid rod of 25.4mm

(1 inch) length was positioned inside the tube, using a press fit. This rod is characterized by a drilling identical to the one of the wing mounting. Since loads should be applied at various positions along the balance as well as in different planes, four rows, each consisting of nine threaded holes, were placed along the calibration tube. To fulfill the first condition, several holes of 7.62mm (0.3 inch) diameter were drilled so that extra weight could be saved.

A screw which fits to the threads was used as a hook-up system. In order to avoid all transmissions of moments, the weights used during the calibration process were fixed to a thread which is attached to the screw.

Theoretical Load Resolution Technique

The basic idea in using a strain gage balance for aerodynamic measurements is the determination of a set of calibration constants which relate known loads applied to the balance to the reading or response of the balance, so that by inverting the procedure any known load taken during a test can be determined from the reading and these calibration constants. Since, in the present case, a four-component balance appears to be sufficient to get the desired results, only the following loads occur:

F_S: side force

F_N: normal force

M_Y: yawing moment

M_P: pitching moment

The model axes are given in Figure 15.

Based on former experience, the assumption seems to be justified that the balance output varies basically only linear with the applied load, so that only first-order load effects have to be considered. These effects are characterized by the following subscripts:

Load	Subscript
F_S	1
F_N	2
M_Y	3
M_P	4

The four output channels of the balance are assigned as follows:

Load	Channel	Symbol
1	F_S	R_1
2	F_N	R_2
3	M_Y	R_3
4	M_P	R_4

Thus, the output of the i^{th} channel can be described by:

$$R_i = k_{i1} \cdot F_S + k_{i2} \cdot F_N + k_{i3} \cdot M_Y + k_{i4} \cdot M_P \quad , \quad (3.24)$$

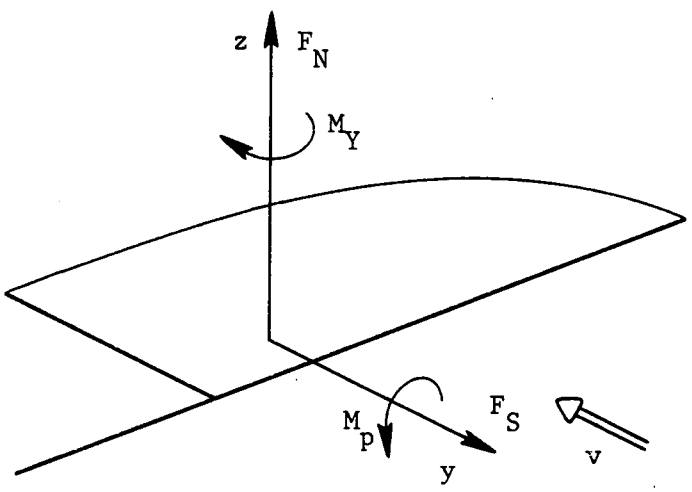


Figure 15. Model Axes.

where k_{ij} (i: channel subscript, j: load subscript) is an influence coefficient, which has to be determined during the calibration. Since every amplifier provides a certain gain, it is useful to divide Equation (3.24) by k_{ij} in order to get the following normalized equation:

$$(L_i)_u = K_{i1} \cdot F_S + K_{i2} \cdot F_N + K_{i3} \cdot M_Y + K_{i4} \cdot M_P \quad , \quad (3.25)$$

where

$K_{ij} = \frac{k_{ij}}{k_{ii}}$ is the normalized calibration coefficient

(note: $K_{ii} = 1$)

and

$(L_i)_u = g_i \cdot R_i$ is the uncorrected load of the i^{th} component [i.e., $(L_1)_u = F_S$]

with:

$g_i = \frac{1}{k_{ii}}$ as the component sensibility factor.

Equation (3.25) is identical to

$$L_u = C \cdot L \quad (3.26)$$

if:

$$L_u = \begin{pmatrix} (F_S)_u \\ (F_N)_u \\ (M_Y)_u \\ (M_P)_u \end{pmatrix} , \quad C = \begin{pmatrix} 1 & K_{12} & K_{13} & K_{14} \\ K_{21} & 1 & K_{23} & K_{24} \\ K_{31} & K_{32} & 1 & K_{34} \\ K_{41} & K_{42} & K_{43} & 1 \end{pmatrix} \text{ and } L = \begin{pmatrix} F_S \\ F_N \\ M_Y \\ M_P \end{pmatrix} .$$

Multiplying Equation (3.26) by C^{-1}, the inverted matrix of C, leads to

$$L = C^{-1} \cdot L_u \quad . \tag{3.27}$$

Thus, the desired loads are a function of the matrix C^{-1}, which is a result of the calibration, and the uncorrected loads L_u, which can easily be calculated from the computer readings.

Actual Calibration

The actual calibration was accomplished by using the calibration aids mentioned above. Several known loads were applied to the bar at different locations and various readings were recorded. The application of Equation (3.25) allows the determination of the calibration matrix C, as can be demonstrated using the side force F_S as an example. If only a side force is applied, all other components drop out of Equation (3.25). Thus, for n known weights, one gets n sets of the following equations, which directly follow from rearranging Equation (3.26):

$$F_S = g_1 \cdot R_1 \quad : \quad \text{applied weight} \tag{3.28}$$

$$F_N = g_2 \cdot R_2 - (K_{21} \cdot F_S) = 0 \tag{3.29}$$

$$M_Y = g_3 \cdot R_3 - (K_{31} \cdot F_S) = 0 \tag{3.30}$$

$$M_P = g_4 \cdot R_4 - (K_{41} \cdot F_S) = 0 \tag{3.31}$$

Since the readings R_i (i = 1 . . . , 4) and the side force F_S are known, the factor g_1 can be determined directly from Equation (3.28). In a similar way, the other factors g_i (i = 1 . . . , 4) follow from applying the remaining pure loads to the balance, so that the calibration constants characterizing the side force can be directly calculated from the Equations (3.29) through (3.31). The missing calibration constants follow, then, in a similar way from the other sets of equations corresponding to the pure application of these loads. Finally, the matrix C has to be inverted in order to get the matrix C^{-1}.

Existing computer codes were used for both tasks--determining the matrix C as well as inverting C.

This balance calibration was done in accordance with Reference [15], which describes the calibration of a six-component strain gage balance, where also second-order interactions are taken into account.

CHAPTER IV

TESTING PROCEDURE

The testing procedure of the qualitative tests is described together with the corresponding results in Chapter V. The flow visualization tests and the performance evaluation tests, however, are described below.

At the beginning of each flow visualization test the smoke generator was turned on so that the heating element could warm up. After having obtained a continuous flow, the wind tunnel could be started. During all flow visualization tests, the tunnel was operated at a speed of 6.1 m/s (20 ft/s). This speed was determined in a preceding test as the maximum speed for clear visualization results. As a result of a preceding test series, a 35mm camera, which was mounted on a tripod and placed in front of the model perpendicular to the flow field, was connected to a flash, whose aperture value was chosen to be 1/16000 second. This flash was placed during the test in front of the right lower corner of the test section so that the illumination of the model and the wake was possible. Alternatives of light sources which gave less acceptable results had been a halogen lamp and a stroboscopic light. During the flow visualization tests, the Models I through V (cp. Chapter II) were investigated

at various angles of attack ranging from 0° up to 60°. A step size of 5° seemed to be accurate enough for a detailed documentation. Since different atmospheric conditions occurring at the inlet of the wind tunnel influenced the smoke stream direction, several pictures were taken at each position. The pictures were developed at the photographic laboratory of The UT Space Institute.

During the performance evaluation tests, the Models I through V were tested at speeds of 7.62 m/s (25 ft/s), 9.1 m/s (30 ft/s) and 10.7 m/s (35 ft/s). The lower speed was given by the error band of the balance, whereas the upper speed was limited by the wing structure. All models were tested within an angle of attack range of -2° to 45° following the example of Reference [12], where tests were conducted up to angles of attack of 30°. At the beginning of each test, various electronic parameters (e.g., excitation voltage) were checked in order to ensure conformity between the test conditions and the balance calibration conditions. In order to take into account the weight of the models as well as the nonlinear behavior of the computer system, the zero reading value of each position was recorded. This led to the following typical test sequence. After having stopped the wind tunnel for one minute, three zero values were taken. Then the wind tunnel was started again, and after another minute three force values were measured. The interval of one minute

had been determined in a preceding test as being sufficient enough to ensure steady conditions. Three values were taken to improve the averaging process as well as being able to check single values against each other. In order to check the repeatability of the data, all models were tested several times under the same conditions.

CHAPTER V

RESULTS AND DISCUSSION

Qualitative Testing

Water Tunnel Testing

The purpose of the water tunnel tests was to generate an unsteady flow situation and to examine the flow field using flow visualization techniques. Model A was used for the first test. This test gave unsatisfactory results since fluttering was not observed at any speed. The testing of Model B turned out the same unsatisfactory result despite the fact that the stiffness of the wing foil changed from Model A to Model B to lower values. The maximum dynamic pressure q obtained in both tests was $q = 32\ N/m^2$.

Since in the study documented in Reference [12] all models were tested in a wind tunnel, where a dynamic pressure of $240\ N/m^2$ was obtained, Model B was also investigated in the low-speed wind tunnel. Fluttering of the trailing edge could already be observed at a speed of 7.62 m/s (25 ft/s), which corresponds at atmospheric conditions to a dynamic pressure of $q \approx 34\ N/m^2$. Thus in both cases--wind tunnel and water tunnel testing--the condition of similar dynamic pressure values was satisfied for Model B. The Strouhal number, which is the relevant

aerodynamic parameter for unsteady problems, was determined in the present case with the chord length of the airfoil measured at the root, the wind tunnel speed and the fluttering frequency of the wing membrane. It revealed that the chord of the water tunnel model and, consequently the wing size, had to be reduced. This follows directly from the fact that the speed attained in the water tunnel is lower than the speed in the wind tunnel. Thus, the Models E and F were built. Testing of these models resulted once again in no observed flutter and, therefore, Model G was constructed. Investigation of this model even at a speed of 46 cm/s (18 in/s) showed only small fluttering of the trailing edge, an effect which could be enhanced by using cylinders as vortex generators. These cylinders were placed upstream of the models perpendicular to the flow direction as well as to the wing leading edge. The level of turbulence and disturbances in the flow, however, was so high that the flow visualization tests did not lead to any further information.

Despite the fact that the speed, as well as the model size, had already exceeded those limits which allow a reasonable investigation, the maximum velocity which could be attained in the water tunnel was still too low to match the Strouhal number occurring in the wind tunnel for the same model. Thus all further investigations

were carried out in the low-speed wind tunnel. Aeroelasticity effects were not regarded since they do not appear to have any significant impact during the water tunnel tests.

Wind Tunnel Testing

Testing of Model G revealed the interesting fact that the membrane did not flutter as long as it was covered with water but started fluttering after the water had evaporated. This phenomenon shows the importance of inertia effects. Similar observations could be made by testing Model C. The aluminum foil membrane did not flutter at low speeds but started fluttering immediately after a higher dynamic pressure was reached. This fluttering was so heavy that it led to immediate damage of the wing. Therefore, further investigation was not possible. It is interesting to note that a similar effect occurred during a test documented in Reference [12]. Moreover, a hysteresis behavior could be observed. The behavior is characterized by the fact that the wind tunnel speed had to be reduced below the value where fluttering started in order to get a motionless membrane. The testing of Model D seemed to reveal the fact that the flow separation at the motionless membrane starts first at the inner part of the wing. No observations could be made during the states where fluttering occurred. Since

a vibration of the leading edge was seen during all the preceding wind tunnel tests, an additional test with a fixed leading edge tip was carried out. This test, however, did not show any significant changes in the earlier observed behavior.

Measurements and Flow Visualization

Model I (Flat Plate)

The investigation of the flat plate in the wind tunnel was conducted for two reasons: First, it is necessary to check the quality of the balance as well as the quality of the complete test setup. Secondly, a state of reference for other models should be established.

Some typical results of the testing procedure are given in Figures 16 through 20, whereas the complete set of the results is presented in Appendix A. In Figures 16 through 18 or in Figures A-1 through A-6 (Appendix A), respectively, the behavior of the lift coefficient c_L, the drag coefficient c_D and the wing efficiency c_L/c_D versus the angle of attack are presented. Figure 19, Figure 20 and Figure A-7 (Appendix A) show the result of the flow visualization test. In order to check the quality of the test setup, both the actual data scatter and the compatibility with existing theory as well as other tests have to be considered. Concerning the first point, it can be stated that the reproducibility is

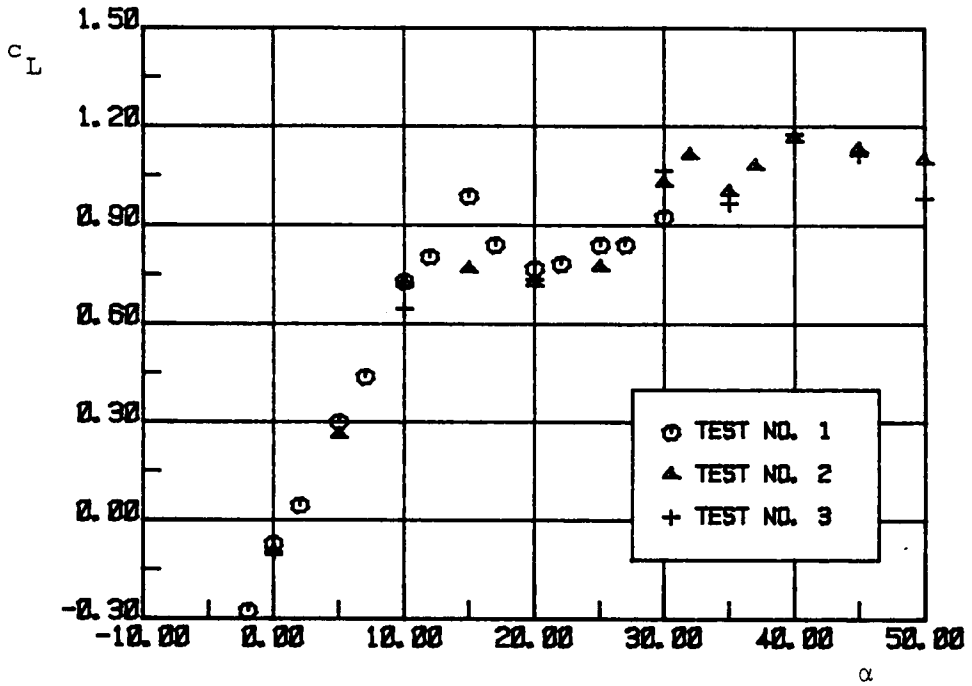


Figure 16. Measured Lift of Model I at 7.62 m/s.

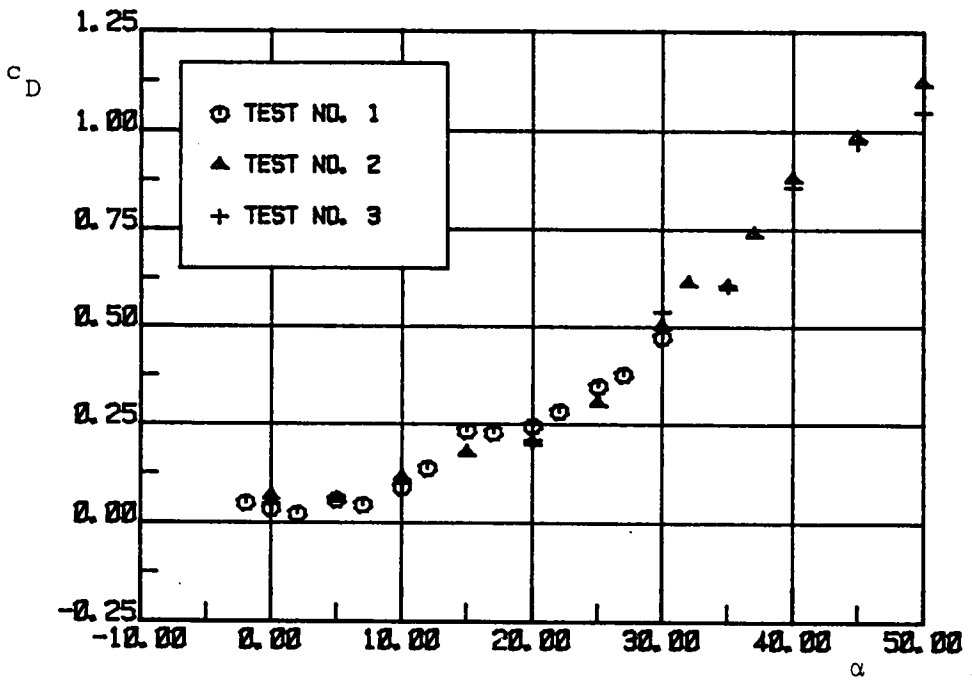


Figure 17. Measured Drag of Model I at 7.62 m/s.

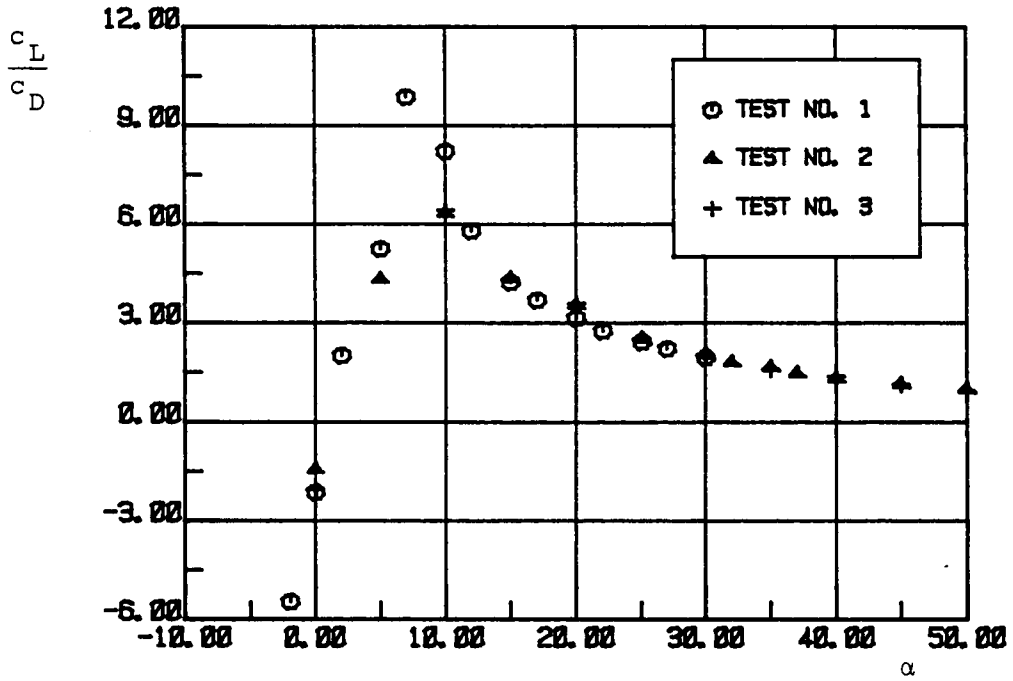


Figure 18. Measured Efficiency of Model I at 7.62 m/s.

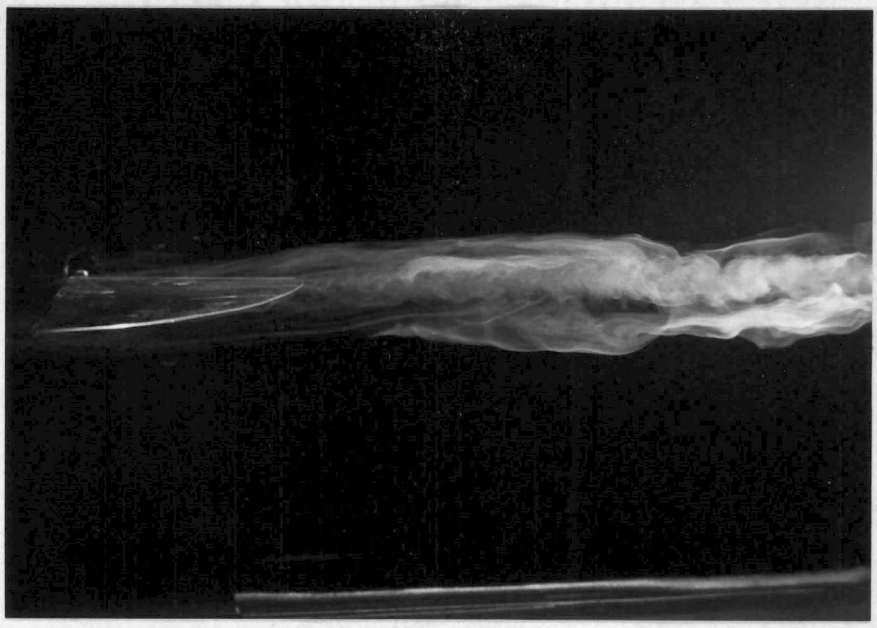


Figure 19. Flow Field of Model I at $\alpha = 0°$.

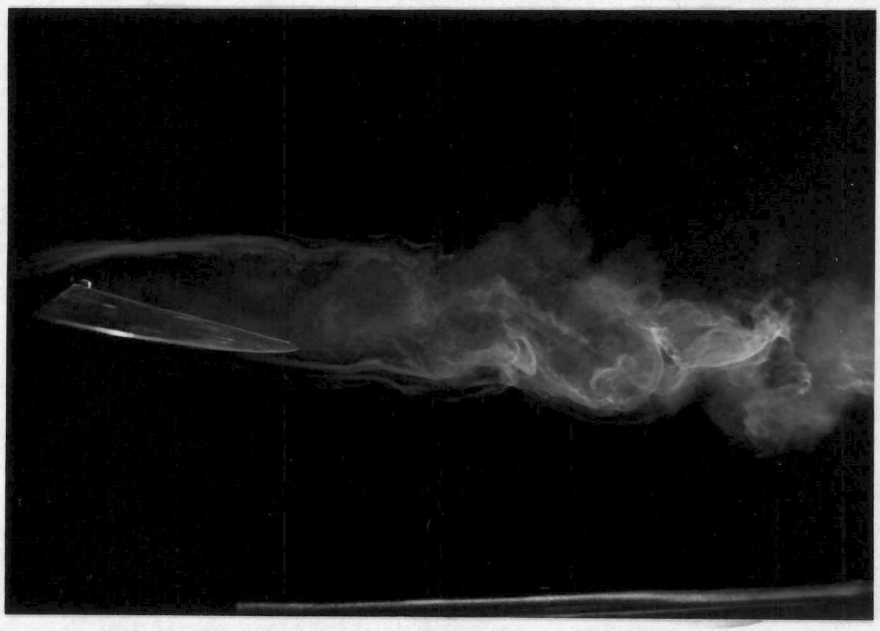


Figure 20. Flow Field of Model I at $\alpha = 15°$.

excellent at angles of attack up to 15°. At higher angles of attack a larger level of scattering was observed. This could be explained by the fact that turbulence and disturbances occurred at the wing surface after the flow separated, as can be observed on the figures presenting the flow visualization results. These disturbances may cause the slight vibrations of the wing which were observed during the ongoing test at those angles of attack. Since the model is directly connected to the balance, some slight deviations among the resulting values follow. The level of scattering increases with speed (cp. Figure A-7 in Appendix A), which appears to be due to the fact that the load put on the wing structure increases with increasing values of the dynamic pressure so that instabilities result in larger vibrations of the wing.

Another influence may be due to Reynolds number effects. In the present case, the Reynolds numbers corresponding to the test speeds are: $Re_1 = 5.7 \cdot 10^4$ for 7.62 m/s , $Re_2 = 6.8 \cdot 10^4$ for 9.1 m/s and $Re_3 = 8 \cdot 10^4$ for 10.7 m/s . Herein, the Reynolds number was defined with the wind tunnel velocity, the chord length of the wing measured at the root and the kinematic viscosity at atmospheric conditions, a value which comes close to the test conditions.

A qualitative outline of the aerodynamic parameters reveals that all values are in good agreement with the well-known tests published in the literature (cp., e.g., [16]). The lift coefficient increases at first almost linearly with the angle of attack, decreases after having reached the angle characterizing flow separation, and increases again due to the pressure difference between the upper and lower surfaces. The drag coefficient shows the expected almost quadratic dependence on the angle of attack. The aerodynamic efficiency c_L/c_D increases, reaches its maximum value and decreases finally with increasing angles of attack towards a value of 1 at $\alpha = 45°$, as predicted by the theory. The other quantitative figures show that the lift coefficient which occurs at an angle of attack of $\alpha = 11°$ at a Reynolds number of $Re = 8.4 \cdot 10^4$ is almost identical to the coefficient which is presented in Reference [16] at the same angle of attack and a Reynolds number of $Re = 4.0 \cdot 10^5$. The slopes $dc_L/dc_D\big|_{\alpha = 0}$, which are presented in Table 1, show a uniform trend and a quite good agreement with the theoretically predicted value of 2π and an even better agreement with the value of 5.02 given by Reference [16] for the profile NACA 0012 at a Reynolds number of $7 \cdot 10^5$.

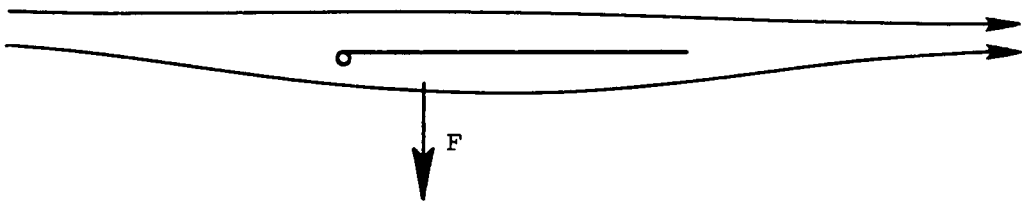
Table 1. Lift Coefficient Gradient as a Function of the Reynolds Number.

Re	$\left.\frac{dc_L}{dc_\alpha}\right\|_{\alpha = 0}$
$5.7 \cdot 10^4$	4.35
$6.8 \cdot 10^4$	4.46
$8 \cdot 10^4$	4.72

Thus, the obtained data also seem to be realistic concerning their order of magnitude. The same can be noted with regard to the Reynolds number influence, since both the slopes and the maximum lift coefficients increase with increasing Reynolds numbers.

A deviation from the published flat plate data, however, occurs at the angle of attack which characterizes the point of flow separation. This angle is given in the present case by values of approximately 15° to 17°, whereas in published tests flow separation occurs at smaller angles down to approximately 12°. The geometric shape of the model appears to be one reason for this behavior, since a sharp leading edge favors separation more than a circular one. This feature could also be one reason that the obtained values for the slopes are closer to those of profiles than to the theoretical one.

Another reason for the delayed flow separation appears to be the rough connection between the leading edge and the flat plate forcing the boundary layer flow to become turbulent, which allows the flow to remain attached longer. Another deviation which can be observed is the negative lift coefficient at zero angles of attack. This phenomenon seems to be a result of the circular leading edge, which causes a larger deviation of the streamlines along the lower than along the upper surface, as shown below.



Thus, a negative lift results. Yet another reason for deviations could be the three-dimensional shape of the model which leads, for example, to induced drag effects.

Model II

The test results of this model are given in Figures 21 through 24 and in Appendix B, where Figures 21 and 22 show, together with the Figures B-1 to B-4, the result of the performance evaluation. Figures 23, 24 and B-5 present the flow visualization photographs.

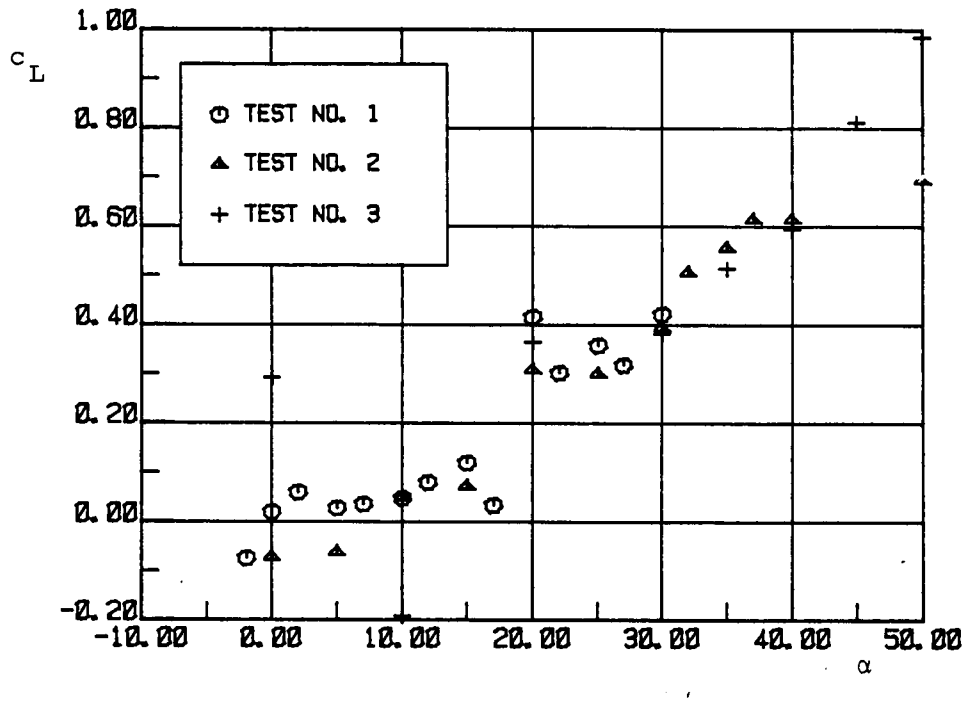


Figure 21. Measured Lift of Model II at 7.62 m/s.

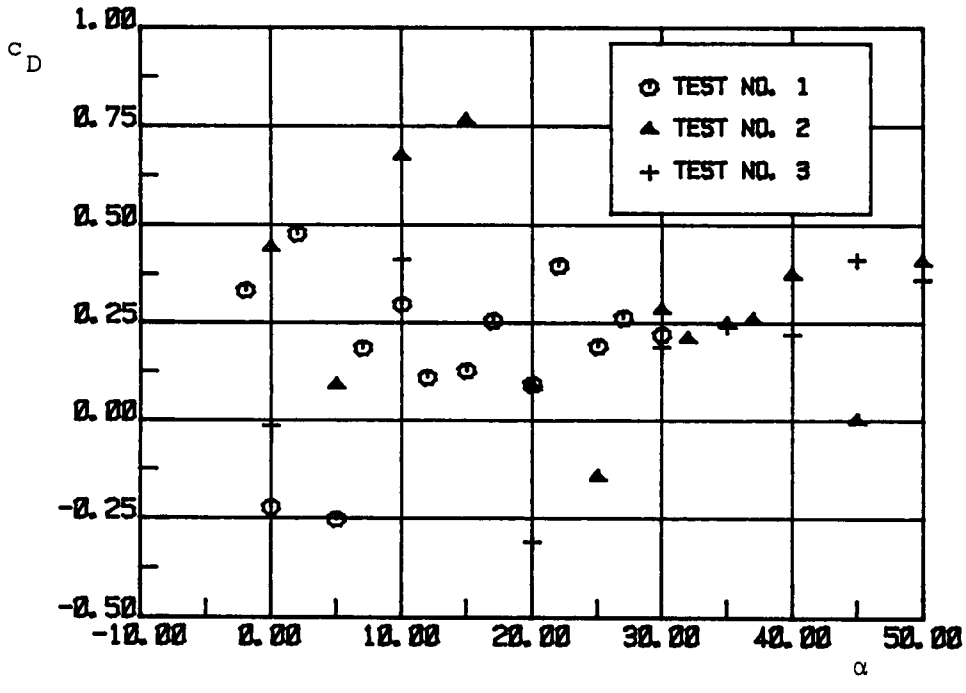


Figure 22. Measured Drag of Model II at 7.62 m/s.

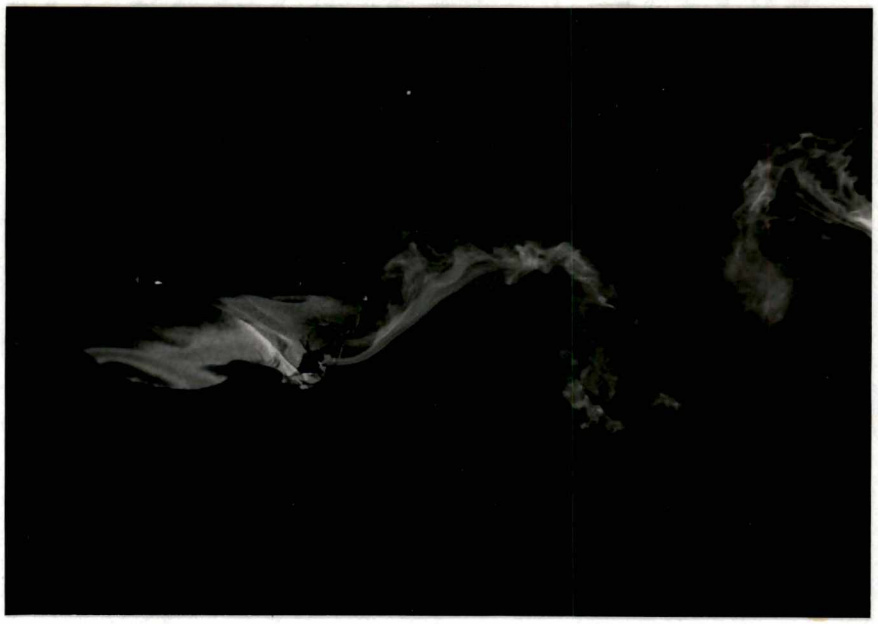


Figure 23. Flow Field of Model II at $\alpha = 0°$.

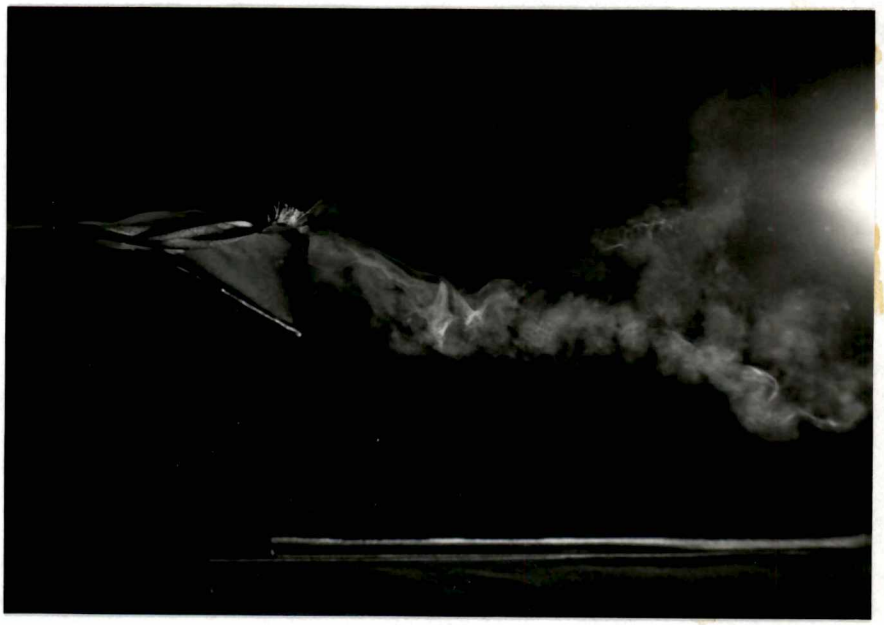


Figure 24. Flow Field of Model II at $\alpha = 30°$.

The figures describing the behavior of the aerodynamic coefficients c_L and c_D versus the angle of attack α show scattered values between -2° and approximately 20° to 25° and angles larger than 40°. This becomes especially evident in figures describing the drag coefficients c_D . An explanation for this phenomenon could be given by the fact that a membrane spread between two axes and having only one degree of freedom is able to move freely between two well-defined angles. If the angle of the oncoming flow falls within this range, the membrane starts to flutter, an effect which can often be observed on sailboats (cp. also [17]). In the present case, observations confirm (cp. also flow visualization pictures) that the membrane flutters heavily at lower angles of attack and has almost stopped at angles around 25°. A small portion of the membrane, however, vibrates at even higher angles of attack. This portion can be located at the outer part of the wing close to the tip. This part represents a portion where tensions caused by the frame show almost no influence. Due to the close connection between membrane and frame, the fluttering of the membrane also induces a vibration of the leading edge which leads to the scattered values being observed. The fact that the leading edge vibrates at small angles of attack more in the horizontal direction than in the vertical one may explain why the drag values

are more widely scattered than the lift values. Another reason for this behavior appears to be the fact that the absolute values of the drag coefficient are usually smaller than those of the lift coefficient, so that the drag coefficient is more affected by the error band of the balance than the lift coefficient. The higher level of scattering at large angles of attack (40° and higher) could have its origin in the flow separation process, where disturbances of the turbulent flow caused by the rough leading edge could influence the membrane (cp. also Model I).

Increasing lift coefficients up to angles of attack of approximately 50° characterize the qualitative behavior of the aerodynamic parameters. It is interesting to note that the slope of the curves describing the lift coefficient versus the angle of attack has signicantly smaller values at angles between -2° and approximately 20° to 25° than at higher angles (cp., for example, Figure 21, page 64). This phenomenon could be explained by the fact that a free-moving membrane is not able to carry loads.

Model III

The results of testing Model III are presented in Figures 25 through 28, as well as in Appendix C. In Figures 25 and 26 or in Figures C-1 to C-4, respectively,

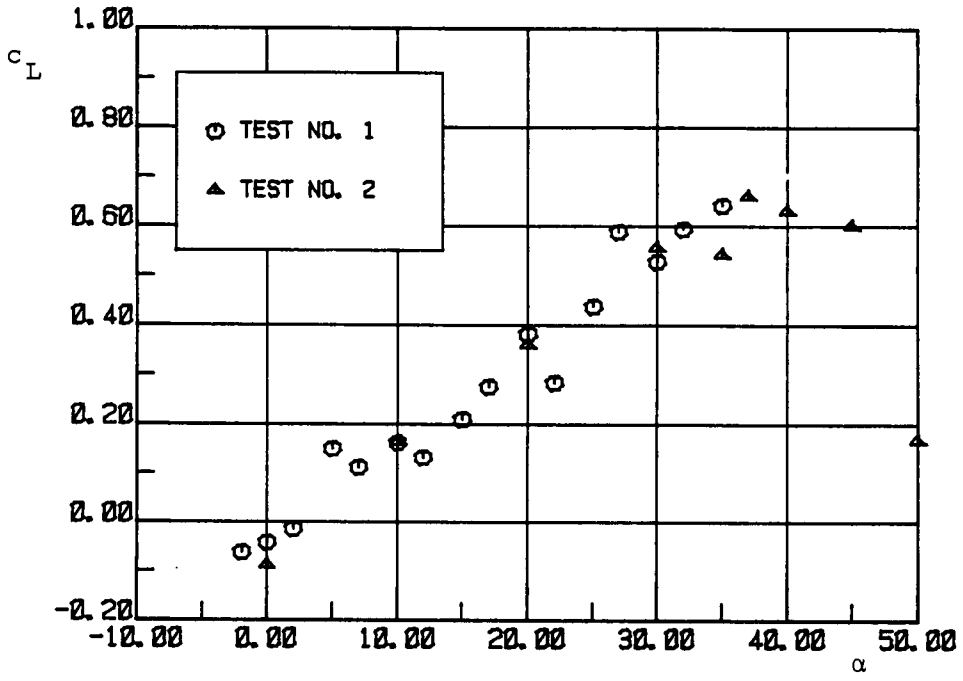


Figure 25. Measured Lift of Model III at 7.62 m/s.

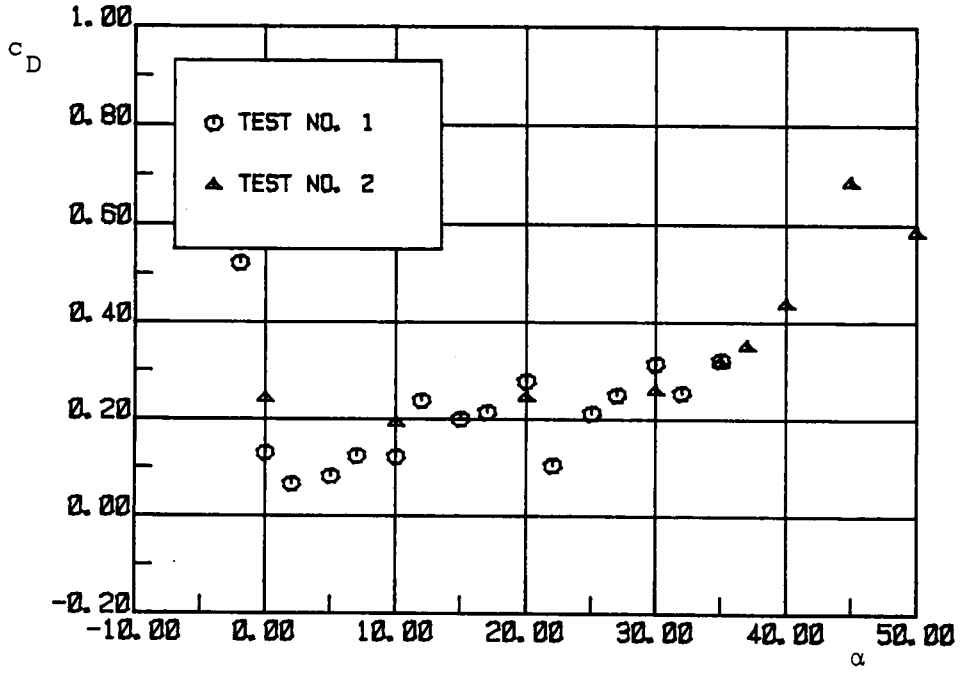


Figure 26. Measured Drag of Model III at 7.62 m/s.

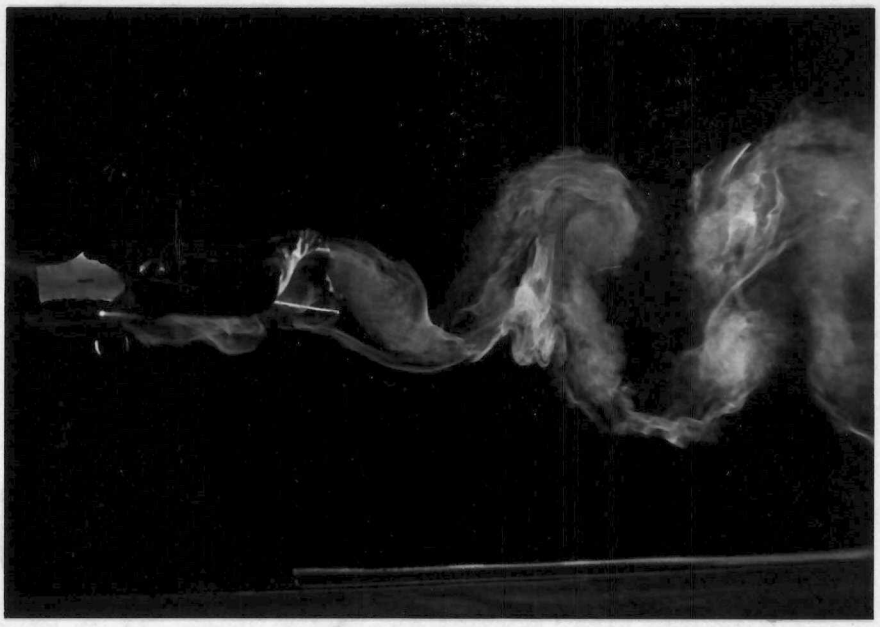


Figure 27. Flow Field of Model III at α = 10°.

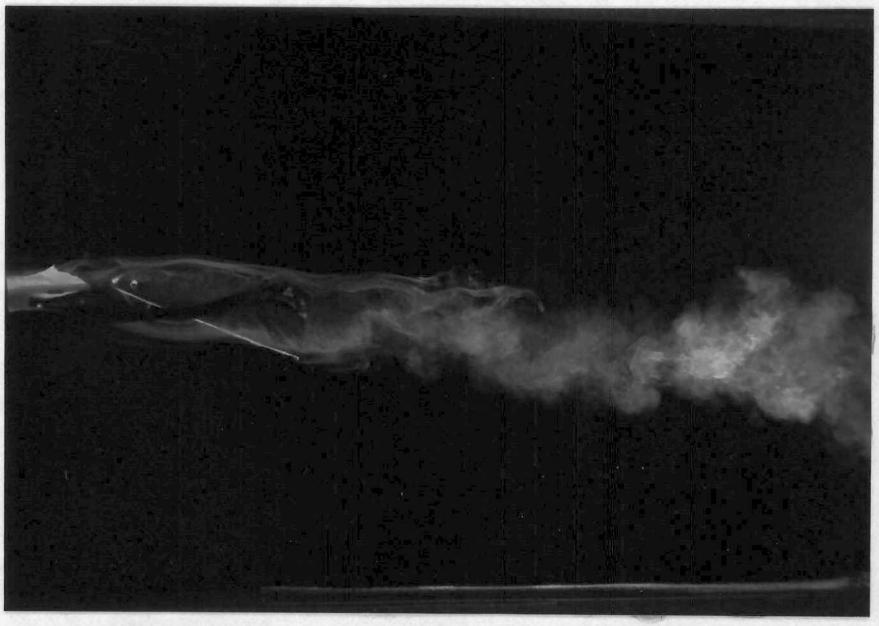


Figure 28. Flow Field of Model III at α = 20°.

the performance evaluation is given, whereas in the Figures 27, 28 and C-5 photographs taken during the flow visualization test are shown.

All the figures which are related to the performance evaluation show a small level of scattering up to angles of attack of approximately 20°. One major reason for this positive effect seems to be the geometry of the model, since the second bar located along the c/3-line increases the stiffness of the frame. This stiffer frame allows vibrations of the leading edge only at higher frequencies and lower amplitudes. The first of these effects prevents larger deviations from the mean value, whereas the second one favors the averaging process done by the computer. Thus, less scattered values result. The higher level of scattering which occurs at larger speed values could be due to the larger dynamic pressure (cp. flat plate).

The figures presenting the lift coefficient c_L as a function of the angle of attack α reveal almost linearly increasing values at lower angles of attack. This phenomenon appears to be the result of several factors. First, it seems to be important that the second bar which is placed along the local c/3-line provides an extra area which is able to carry loads. Secondly, the fact that the first portion of the pleat already has a positive angle of incidence, even if the wing is still

at zero angle of attack, may contribute to these higher lift values. Thirdly, a vortex could develop in the pleat and provide lift, since the drag components would cancel each other out (cp. Kasper wing [5]) at lower angles of attack.

At angles of attack greater than approximately 20°, the values for the drag coefficients decrease, as is shown in the corresponding figures. This appears to be due to the fact that the membrane has almost completely stopped fluttering (cp. description of Model II in Chapter II). Since flow separation always enhances the drag, and since an extraordinarily high level of flow separation exists within the range of the angles of attack which characterizes the fluttering membrane, decreasing drag values could be expected at those angles which characterize the almost motionless membrane. Figure 25 shows a further increase of the lift coefficients up to an angle of incidence of approximately 35°. This increase may be supported by a vortex which could be developed at the inner part of the wing. It is interesting to note that the second portion of the pleat which is characterized by negative angles at zero angle of attack is almost tangential to the membrane within the range of angles of incidence being considered. This vortex could also be responsible for the increasing level of drag. Another reason for the almost continuously increasing drag

appears to be the fact that the drag component of the resulting force increases with increasing angles of attack (cp. flat plate).

A severe flow separation obviously takes place at around an angle of 37°, which leads to decreasing lift coefficients and further increasing drag coefficients. The vortex which may have developed at the inner part of the wing could separate and induce the membrane vibrations (cp. also vortex shedding around a cylinder). The slight difference between curves of different velocities could be due to the Reynolds number influence (cp., for example, effect on vortices).

The flow visualization pictures seem to be in good agreement with this interpretation. The fact has been taken into account that the visualization of a vortex core is hard to accomplish (cp. [18]).

Model IV and Model V

The results of the performance evaluation of Model IV are given in Figure 29, Figure 30, and in Figures D-1 through D-4 in Appendix D, whereas those of Model V are presented in Figure 31, Figure 32, and in Figures D-6 and D-7. The pictures resulting from the flow visualization tests are included in Appendix D (Figure D-5 refers to Model IV and Figure D-8 characterizes Model V).

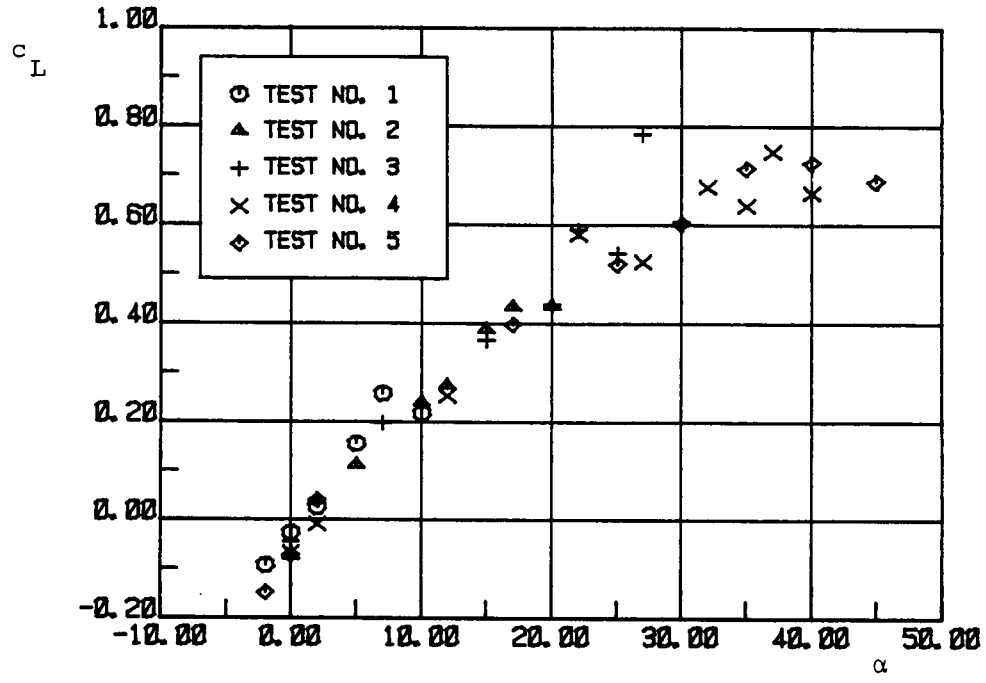


Figure 29. Measured Lift of Model IV at 7.62 m/s.

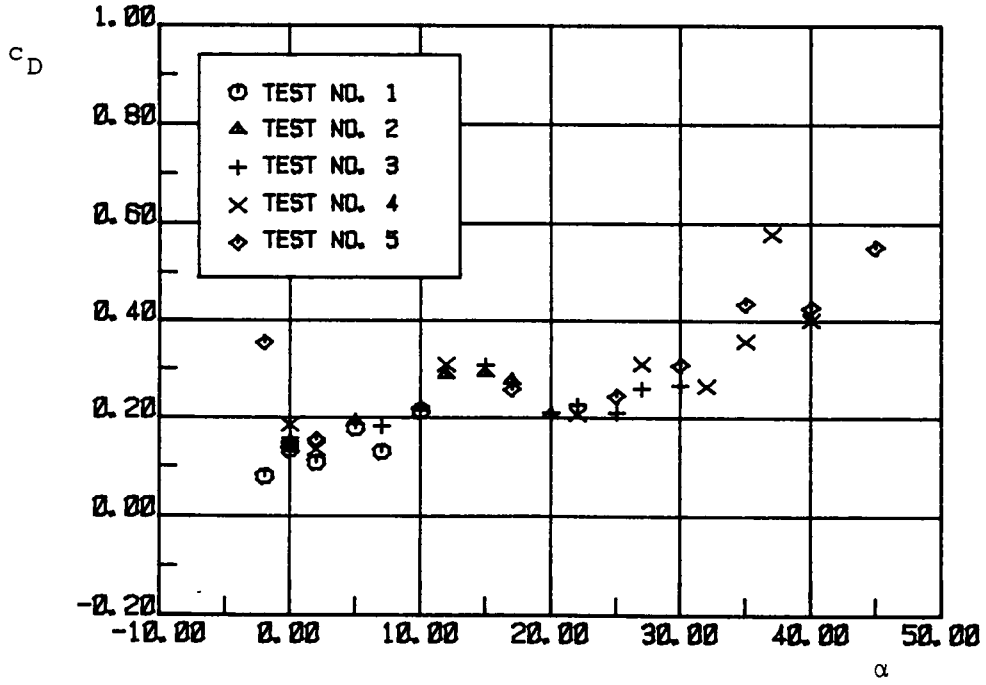


Figure 30. Measured Drag of Model IV at 7.62 m/s.

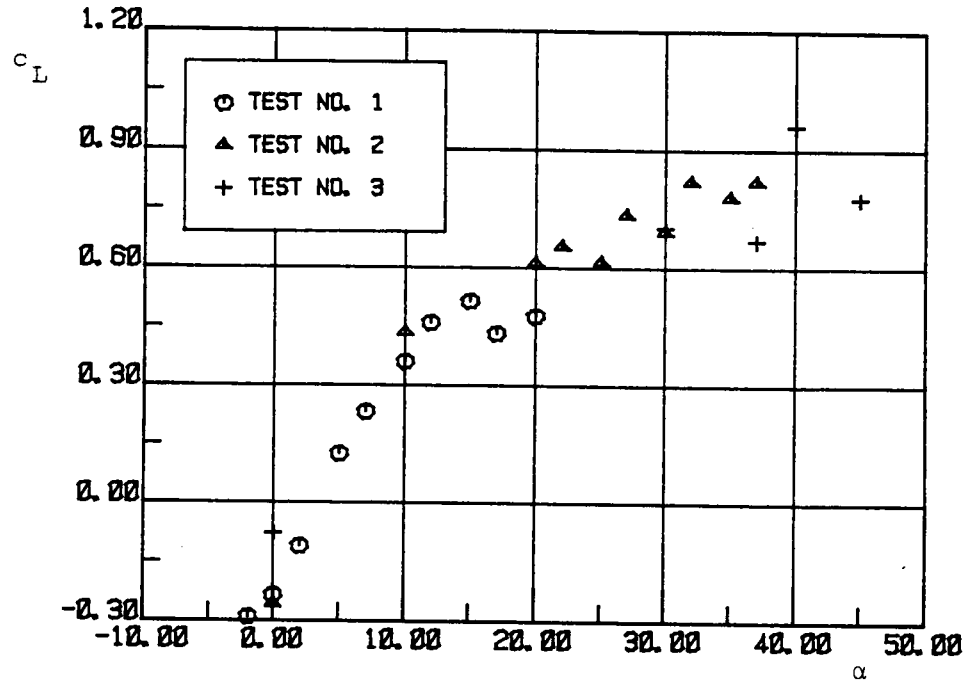


Figure 31. Measured Lift of Model V at 7.62 m/s.

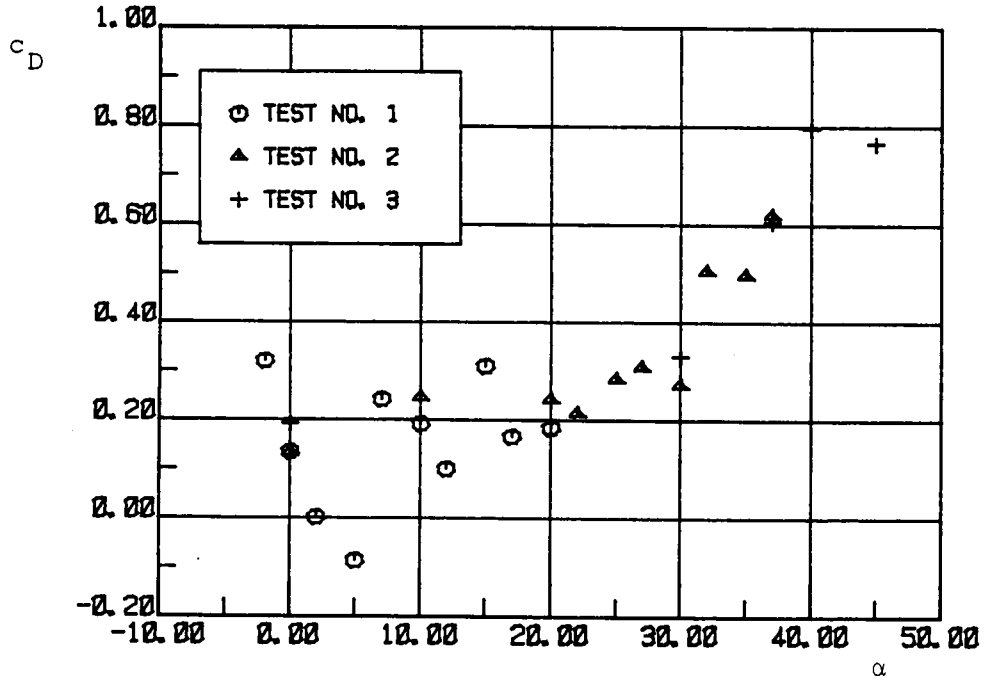


Figure 32. Measured Drag of Model V at 7.62 m/s.

Since the photographs of the flow visualization tests are similar to those taken while testing Model III, only a few representative figures were chosen.

The curves characterizing the lift and drag performance over the various angles of attack also show a similar behavior to those describing Model III, so that the description given for Model III is probably valid for Model IV and Model V in an analogous way. The slight differences which occur appear to be due to the different geometries.

Comparative Evaluation

Comparing the level of scattering among all models reveals that usually a higher level of scattering occurs at angles of attack around and higher than 35°. Furthermore, the level of scattering increases with increasing speed values. The first observation appears to be due to the higher level of unsteadiness at these angles, whereas the second phenomenon could be due to increasing values of the dynamic pressure (cp. also flat plate).

The flow visualization results reveal that the Models II through V are characterized by similar flow fields. This observation leads to the two representative schemes which are presented in Figure 33 and Figure 34. In the first drawing (Figure 33), a wake is shown which

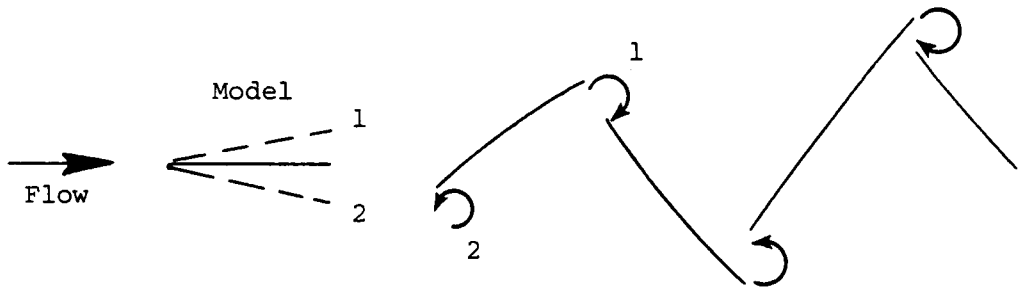


Figure 33. Schematic Flow Field at an Angle of Attack Around $\alpha = 0°$.

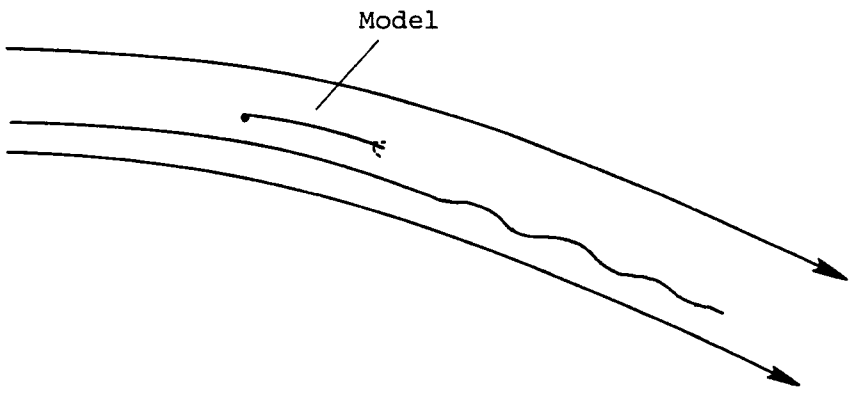


Figure 34. Schematic Flow Field at an Angle of Attack Around $\alpha = 30°$.

appears to be typical of all configurations at lower angles of attack (cp., for example, Figure D-8 in Appendix D). This flow field is similar to a Kármán vortex street and is mainly dominated by the fluttering membrane. The second drawing (Figure 34) presents a typical flow field characterizing these models at angles of incidence between approximately 20° and 30°. Since the membrane is almost motionless at these angles (cp. also the section describing Model II in Chapter II), the picture shows a more uniform wake with downward-moving streamlines (cp. also Figure C-5, Appendix C). The fact that a wave-like pattern occurs in the lower portion of the wake (cp. also Figure C-5) confirms the observation that a small part of the membrane is still vibrating (cp. section describing Model II).

The lowest lift coefficients as well as the highest level of scattering occur at all speeds up to angles of incidence of approximately 20° for Model II. The fluttering occurring at these angles is, in connection with the frame, one possible reason for these phenomena. A detailed explanation is given in the sections describing the Models II and III, respectively. The angle at which the flutter discontinues was nearly the same for all models and characterizes dropping values for the drag coefficient. This phenomenon could be due to a lower

level of flow separation, as explained in the portion describing Model III.

Figure 35 shows the approximate behavior of the curves describing the lift coefficient versus the angle of attack at a velocity of 7.62 m/s. Comparison among the Models III through V reveals that the slope of the curves describing the lift coefficient versus the angle of attack increases in the same sequence. This is interesting to note, since the flow is disturbed by an increasing number of pleats. A steady vortex which may develop in these pleats appears to be one of the reasons (cp. also section describing Model III) for this phenomenon. Herein, the fact has to be taken into consideration that locked vortices are extremely sensitive to the angle of attack and the geometric configuration (cp.[19]). This behavior may also be a reason for the slight drop of the lift coefficients which seems to appear at almost all configurations at the same angle which characterizes the stopping of the membrane oscillations. There is a possibility that the local lift coefficient characterizing the pleats decreases at higher angle of incidence, whereas the local lift coefficient characterizing the motionless membrane increases. These effects may lead to the presented curves.

A direct comparison of the Models II through V with the flat plate reveals that none of these models

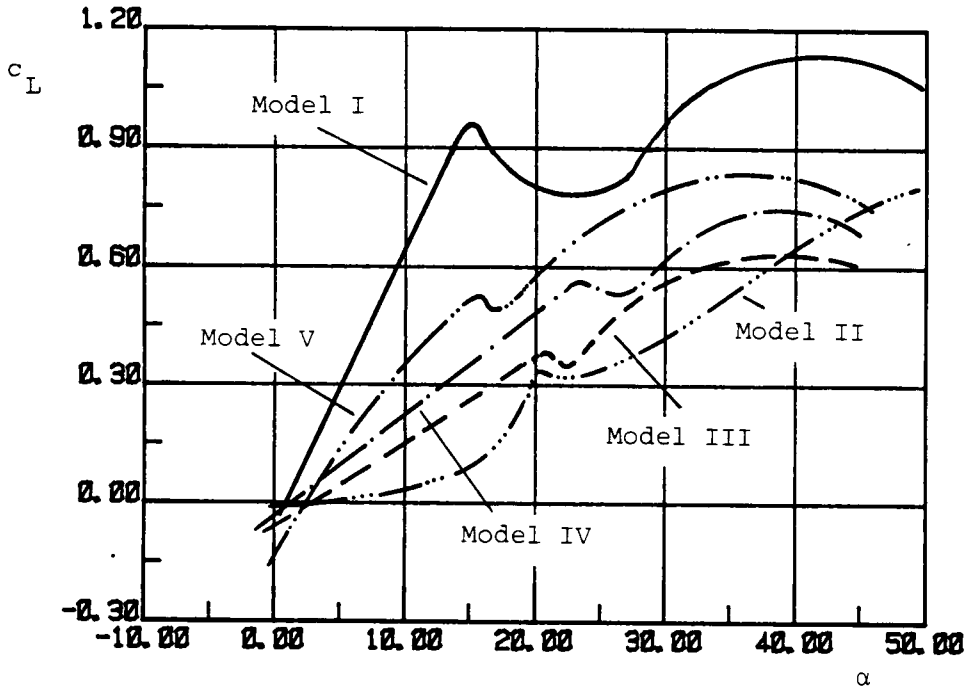


Figure 35. Averaged Lift Coefficient of Models I Through V at 7.62 m/s.

achieves a higher lift coefficient. The porous structure of the wing surface could be one reason for this phenomenon. Certain advantages, however, may be given at higher angles of attack concerning the aerodynamic efficiency c_L/c_D as shown in Table 2. Only selected values of the performance c_L/c_D are given, due to the large distortions which are caused by the scattering of the lift and drag coefficients. Moreover, the angle of incidence measured at the root is not identical to the local angles which occur in spanwise direction. Actually, the effective angle is smaller than the angle measured at the root, since the local angle decreases from the value forced by the root to a value of almost zero degrees measured at the wing tip. This effect results in a higher degree of twisting at the root of the wing than at the wing tip. Another advantage of the Models II through V is the fact that a stall only occurs at high angles of attack around 40°.

Comparison with the Literature Data

In Reference [12], values around 3.75 are presented for the lift coefficient gradient of an elliptical planform. A value of 1.05 characterizes a local maximum of the lift coefficient which occurred at an angle of attack around 15°, whereas the absolute maximum is given at 30° by a value of 1.27. In the present work, the lift

Table 2. Aerodynamic Efficiency (c_L/c_D) at a Speed of 7.62 m/s (25 ft/s).

Alpha \ Model	I	II	III	IV	V
10°	6.99*	0.11*	1.08*	1.05*	1.82*
20°	3.42*	4.01*	1.43*	2.1*	2.57*
30°	1.99*	1.77*	1.91*	2.11	2.33*
40°	1.35*	2.17*	1.44	1.68*	1.2
50°	1.15*	2.22*	0.28	1.25	1.01

*Averaged values.

coefficient gradient has values around 4.5 (see Table 1, page 62), whereas the maximum lift coefficient $c_{L_{max}}$ is characterized by values around 0.85 at angles around 45°. Thus, these values are characterized by the same order of magnitude. However, this comparison has to take into account that the models documented in Reference [12] have a plane surface and not a pleated structure. Further differences occur in the model mounting, since in Reference [12] the models are fixed along the root as well as at the wing tip.

Investigation of the data available in the literature reveals that the hysteresis behavior discussed in the section describing the results of the qualitative testing in the wind tunnel was also observed by Greenshalgh, Reference [11].

Comparison with the data available for the dragonfly reveals that the values for the averaged maximum lift coefficient are ranging from 2 to 3 (cp. [6] and [10]). For hovering conditions, even a value of 6.1 is predicted (cp. [10]). These values are significantly higher than those achieved during the present tests. This indicates that the vertical displacement of the wing also has to be taken into consideration. Another difference from the present test setup represents the fact that the interactions of the front wing with the rear wing of the dragonfly are important for the creation

of lift (cp. [10]). Both arguments should be taken into account during further investigations.

CHAPTER VI

COMMENTS AND CONCLUSIONS

A systematic study has been performed on various flexible wing models with different size, structure and profiles. This study was conducted in a water tunnel and a low-speed wind tunnel to provide qualitative flow visualization to understand the flow physics and quantitative data in order to evaluate the performance of these various shapes. The wind tunnel free stream speed was in the range of 7.62 m/s (25 ft/s) to 10.7 m/s (35 ft/s) and the Reynolds number based on the root chord was $5.7 \cdot 10^4$ to $8 \cdot 10^4$. As a conclusion of the work, the following statements can be made:

1. The tests in the water tunnel gave unsatisfactory results, since the speed values realizable in this facility were too low.
2. A four-component force balance was designed which enabled accurate and repeatable measurements within the tested speed range.
3. Measurement on the flat plate model showed a good agreement with experimental and theoretical values available in the literature.
4. Measurements of the flexible wing models revealed:

a. Lower values for the maximum lift coefficients were obtained for the flexible wings than for the flat plate.
b. Slightly higher values for the aerodynamic efficiency c_L/c_D characterizes the flexible wing models at higher angles of attack than the flat plate models.
c. A considerable benign or delayed stall can be observed for the flexible wing models.
d. Pleated structure leads to improvements in the aerodynamic performance.
e. The presence of unsteady effects leading to lift enhancement is very likely but could not be proven.

Despite the fact that the results of the present work do not prove any extraordinary advantages of the flexible wings compared with the flat plate at lower angles of attack, the possible existence of unsteady effects which allow a lift enhancement should justify further investigations.

The present test setup could be improved by using an electronic system which allows the averaging of more data values so that the level of scattering could be reduced. Using a more sensitive force balance could serve the same purpose since it would allow lower speed values to be recorded. It should be noted that, in this study,

a set of firm mounted wings which are able to generate unsteady motions was used in connection with an electronic system which evaluates the data points by an averaging process. Thus, a "steady" mounted wing being able to produce "unsteady" motions was examined by using a "steady" data acquisition system. Therefore, an improvement of this test setup could be achieved if instantaneous force values were taken. This also would allow a further comparison with insect data available in the literature. The next step could be a test setup which allows a direct influencing of the model so that controlled unsteady movements of the wing are possible.

Another approach could be the use of two models. A flexible model could generate the unsteady motions for another stiff wing. Following these tests, two flexible wings could be used with the objective that the unsteady flow field generated by the first model would influence the second model in a way that a lift enhancement results.

BIBLIOGRAPHY

BIBLIOGRAPHY

1. Nachtigall, Werner. "Gliding Flight in Petaurus-Breviceps-Papuamus. III. Model Measurements of the Influence of Fur Cover on Flow and Generation of Aerodynamic Force Components," Journal of Comparative Physiology, 133, No. 4, 1979, pp. 339-350.

2. Reder, J. "Nylon-Pelzflügel für Segelflugzeuge? Mit Zusätzlichen Bemerkungen Von E. Ufer," Aerokurier, 535-536, 1969.

3. Nachtigall, Werner. "On the Significance of the Reynolds Number and the Fluid Mechanical Phenomena Connected to It in Swimming Physiology and Flight Biophysics," Physiology of Movements --Biomechanics, Stuttgart, New York, 1977.

4. Maxworthy, T. "The Fluid Dynamics of Insect Flight," Ann. Rev. Fluid Mech., 1981, 13, pp. 325-350.

5. Kruppa, Edward W. "A Wind Tunnel Investigation of the Kasper Vortex Concept," AIAA 77-310, 13th Annual Meeting, Washington, D.C., Jan. 1977.

6. Weis-Fogh, Torkel. "Unusual Mechanisms for the Generation of Lift in Flying Animals," Scientific American, Nov. 1975.

7. Ellington, C. P. "Vortices and Hovering Flight," Instationäre Effekte an schwingenden Tierflügeln: Beiträge zu Struktur und Funktion biologischer Antriebsmechanismen, Mainz 1977, pp. 782-819.

8. Nachtigall, Werner. "Quick Changes in Beating and Twisting Movements of Oscillating Fly Wings and Their Possible Role in Generation of Unstationary Aerodynamic Forces," Journal of Comparative Physiology, Vol. 133, 1979, pp. 351-355.

9. Hertel, Heinrich. Structure, Form and Movement. New York, 1963, pp. 78-87.

10. Somps, C.; Luttges, M. "Dragonfly Flight: Novel Uses of Unsteady Separated Flow," Science, Vol. 228, 14 June 1985, pp. 1326-1329.

11. Greenshalgh, S.; Curtis, H. C.; Smith, B. "Aerodynamic Properties of a Two-Dimensional Inextensible Flexible Airfoil," AIAA Journal, Vol. 22, No. 7, July 1984, pp. 865-870.

12. Greenshalgh, S.; Curtis, H. C. "Aerodynamic Characteristics of a Membrane Wing," AIAA 84-2168, 2nd Applied Aerodynamics Conference, Seattle, Washington, Aug. 21-28, 1984.

13. U.S. Air Force, Unpublished Report, 1985.

14. Gilliam, Jr., F. T. An Investigation of the Effects of Discrete Wing Tip Jets on Wake Vortex Roll Up, Ph.D. dissertation, University of Tennessee, Knoxville, 1983.

15. Holmes, John E. "Static Multiple-Load Measurement Technique as Utilized in the Naval Surface Weapons Center's Wind Tunnels." NSWC/WOL/TR 76-26, April 30, 1976.

16. Schlichting, Truckenbrodt. Aerodynamik des Flugzeuges, Vol. 1, Springer-Verlag, Berlin, Heidelberg, New York, 1967.

17. Marchaj, C. A. Aero-Hydrodynamics of Sailing, Dodd-Mead, 1979.

18. Dunham. "The Static Pressure in a Vortex Core," Aeronautical Journal, Paper No. 623, October 1979, pp. 402-406.

19. Little Jr., B. H., and Whipkey, R. R. "Locked Vortex Afterbodies," J. Aircraft, Vol. 16, No. 5, Article No. 78-1179.

APPENDIXES

APPENDIX A

RESULTS OF MODEL I

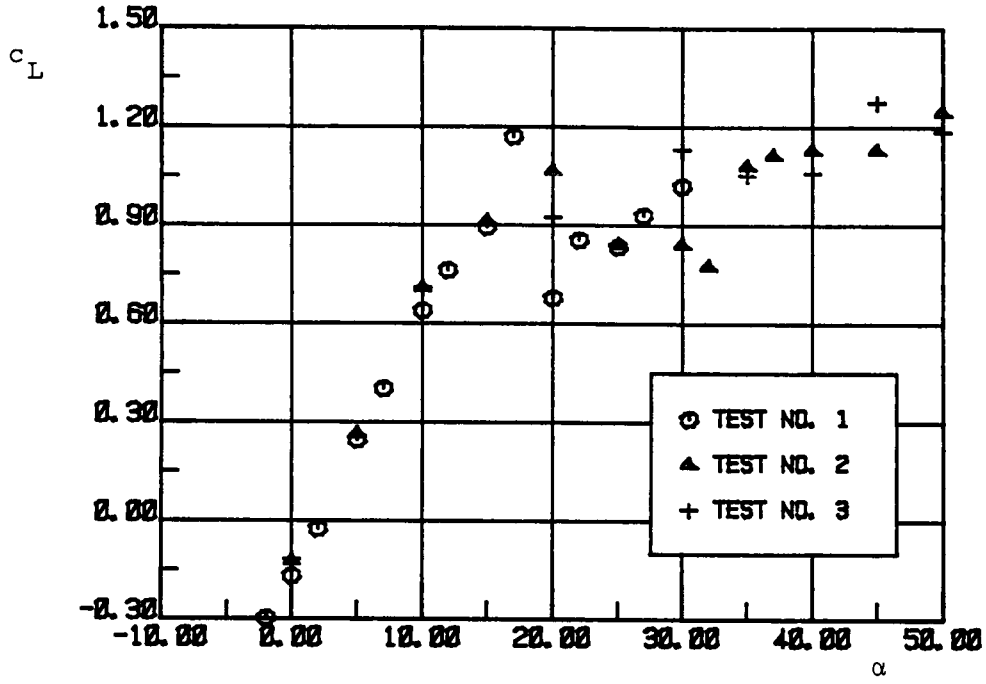


Figure A-1. Measured Lift of Model I at 9.1 m/s.

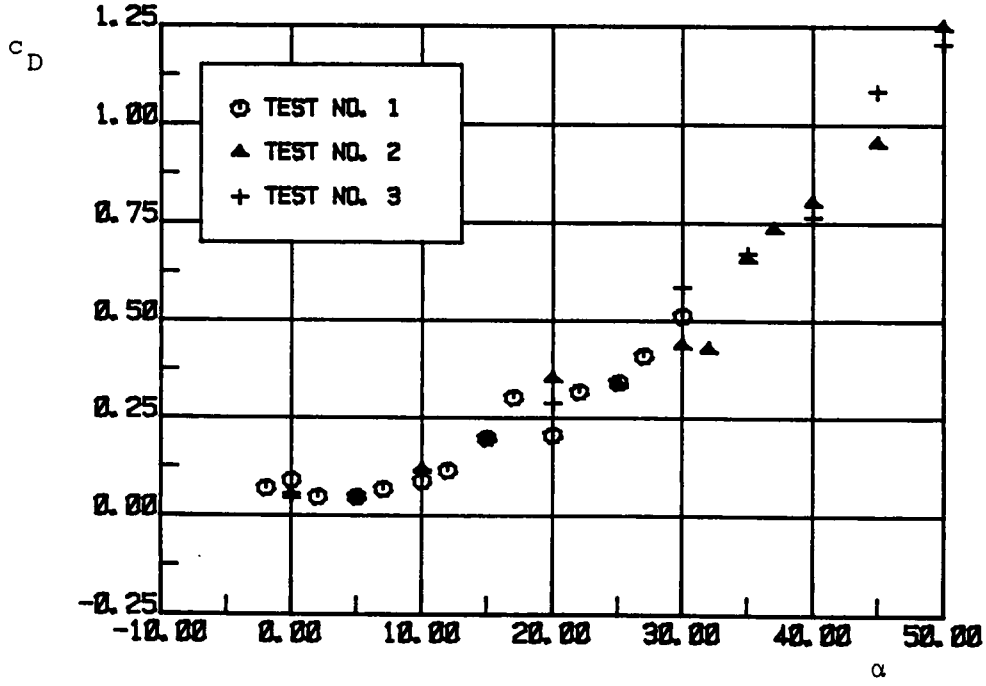


Figure A-2. Measured Drag of Model I at 9.1 m/s.

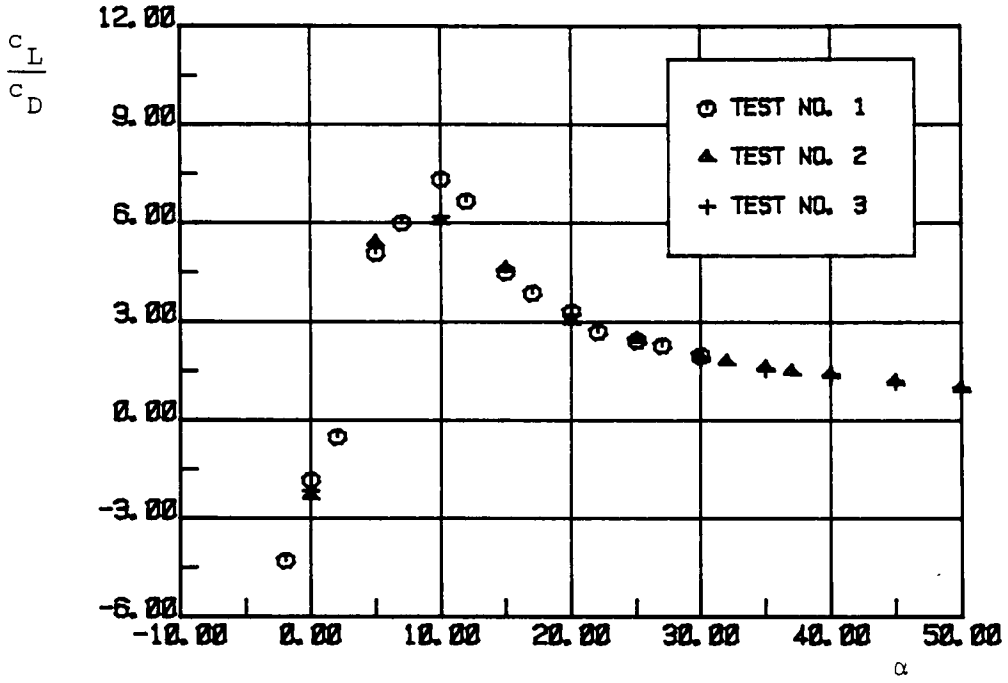


Figure A-3. Measured Efficiency of Model I at 9.1 m/s.

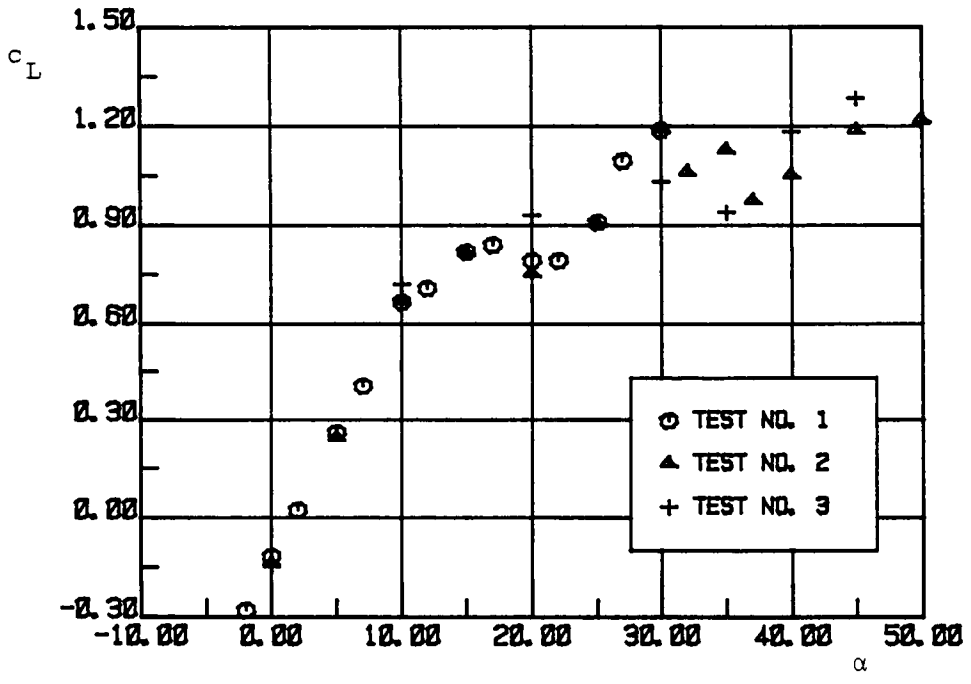


Figure A-4. Measured Lift of Model I at 10.7 m/s.

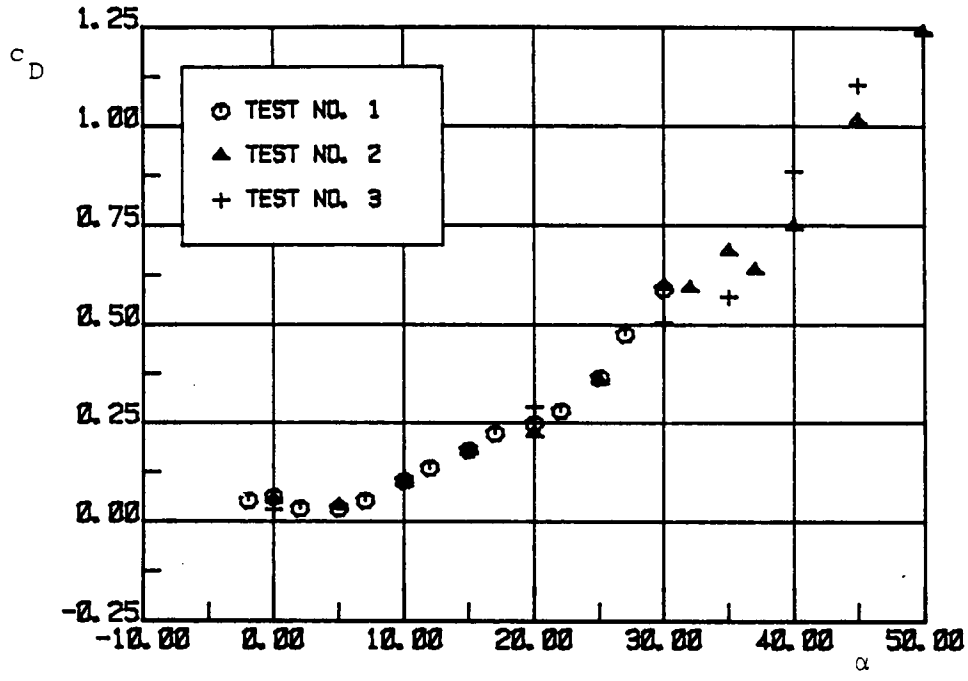


Figure A-5. Measured Drag of Model I at 10.7 m/s.

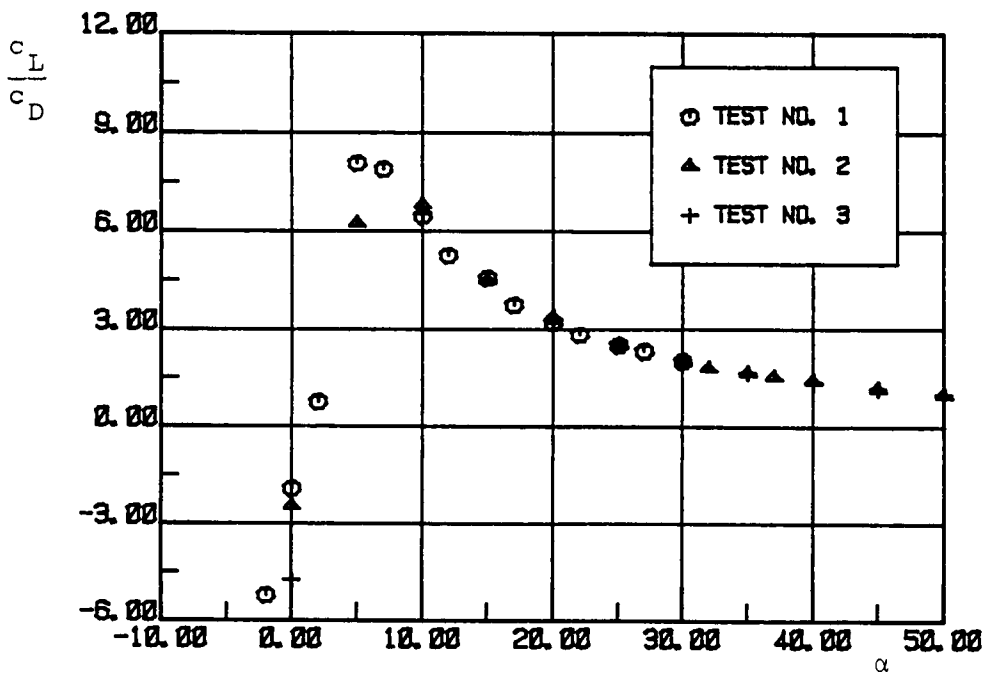
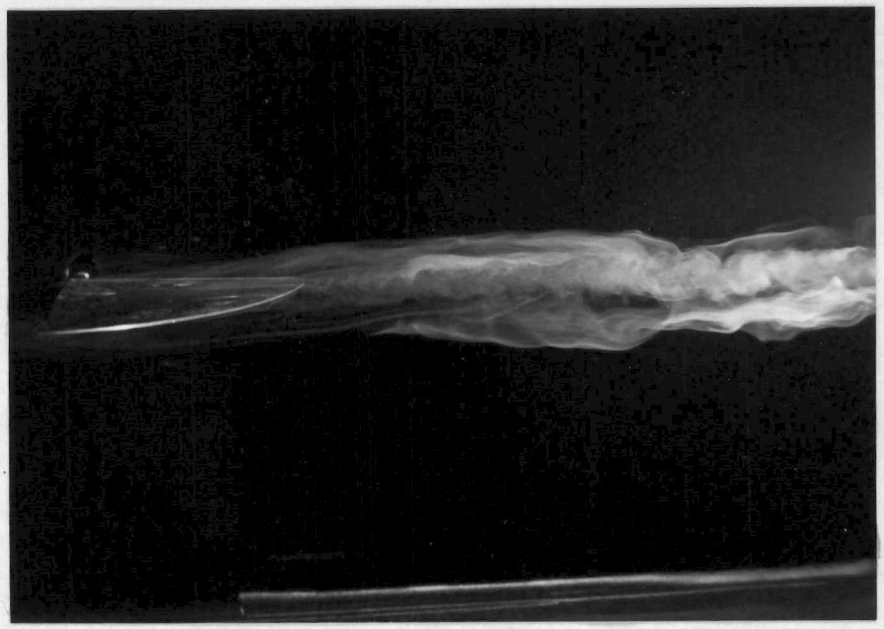


Figure A-6. Measured Efficiency of Model I at 10.7 m/s.

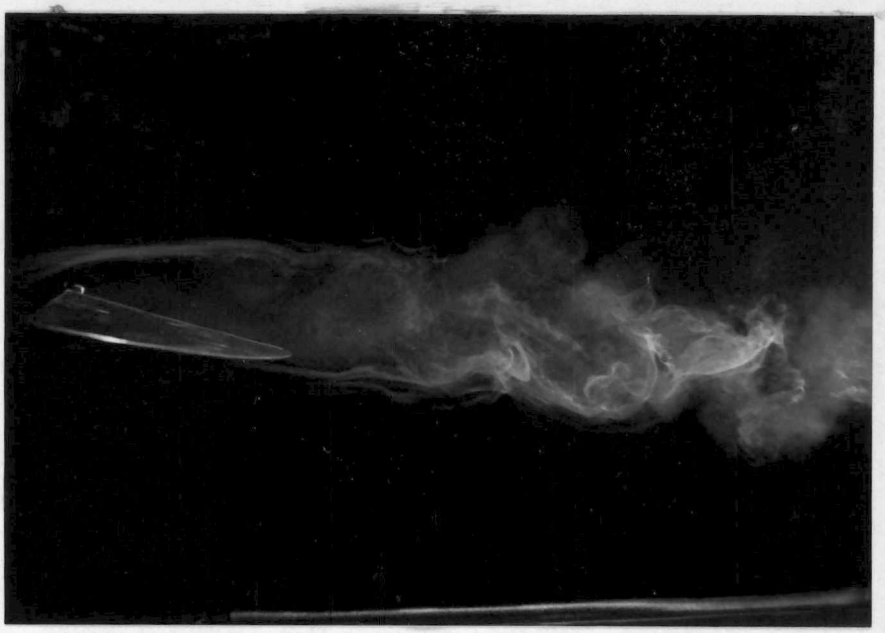


$\alpha = 0°$

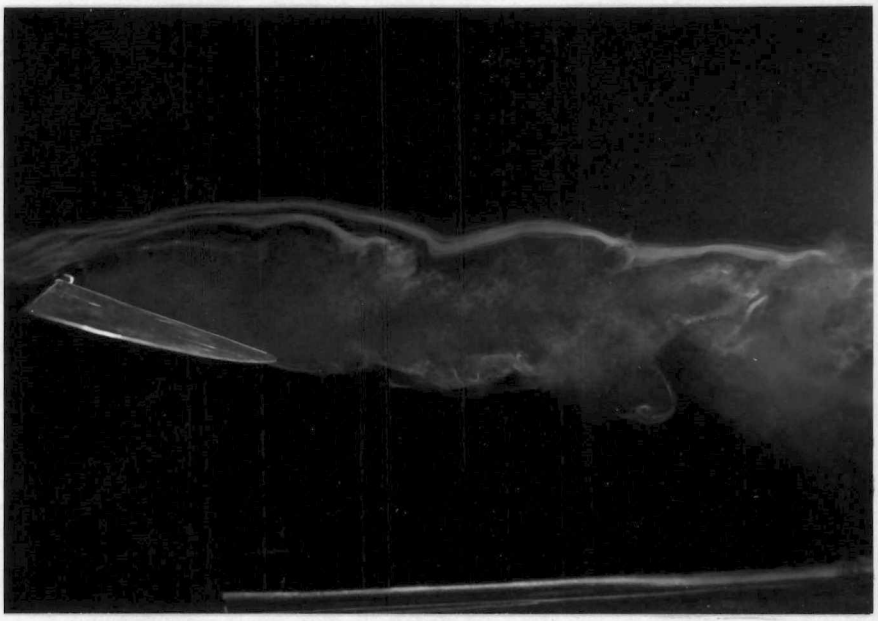


$\alpha = 10°$

Figure A-7. Flow Field of Model I.

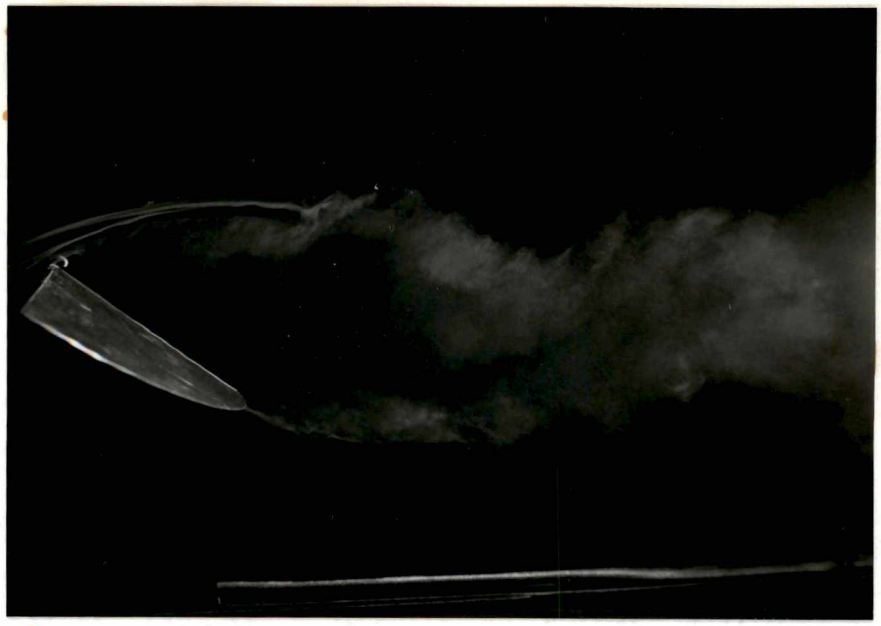


$\alpha = 15°$



$\alpha = 20°$

Figure A-7 (continued)



$\alpha = 35°$



$\alpha = 40°$

Figure A-7 (continued)

APPENDIX B

RESULTS OF MODEL II

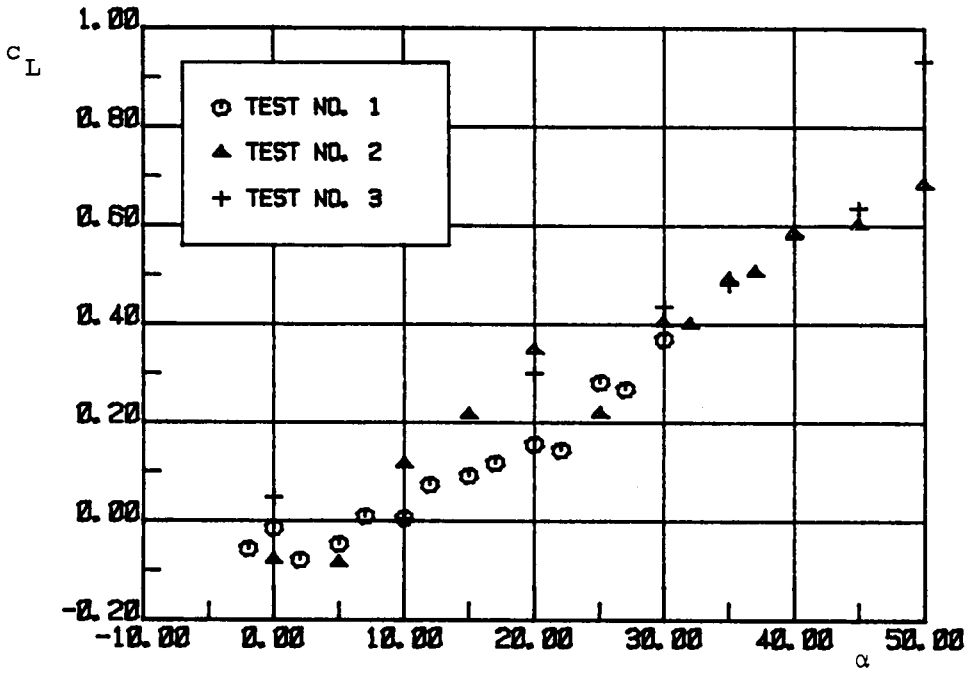


Figure B-1. Measured Lift of Model II at 9.1 m/s.

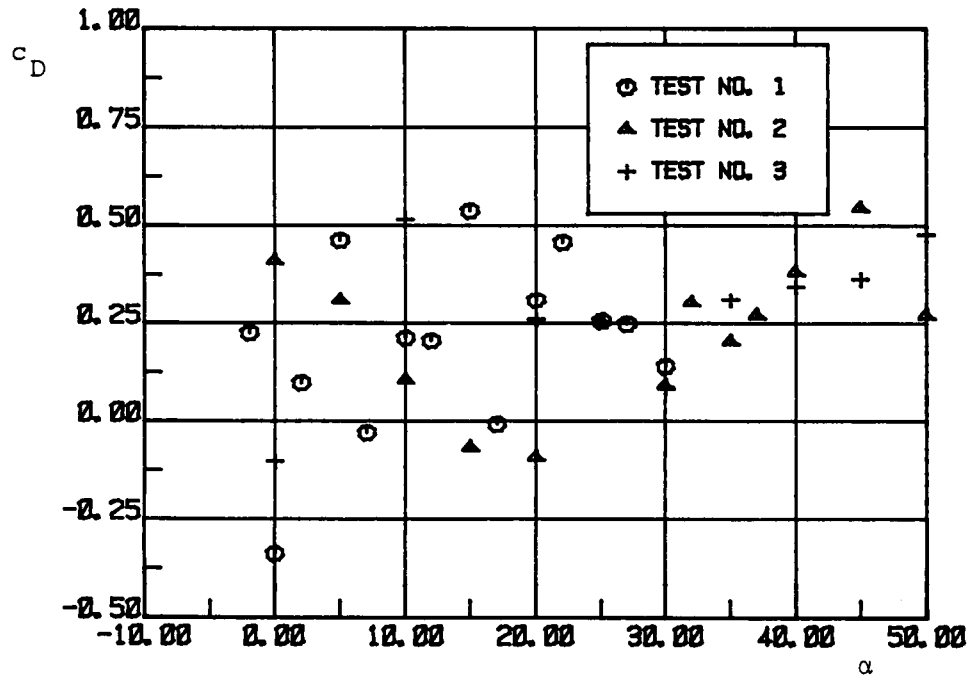


Figure B-2. Measured Drag of Model II at 9.1 m/s.

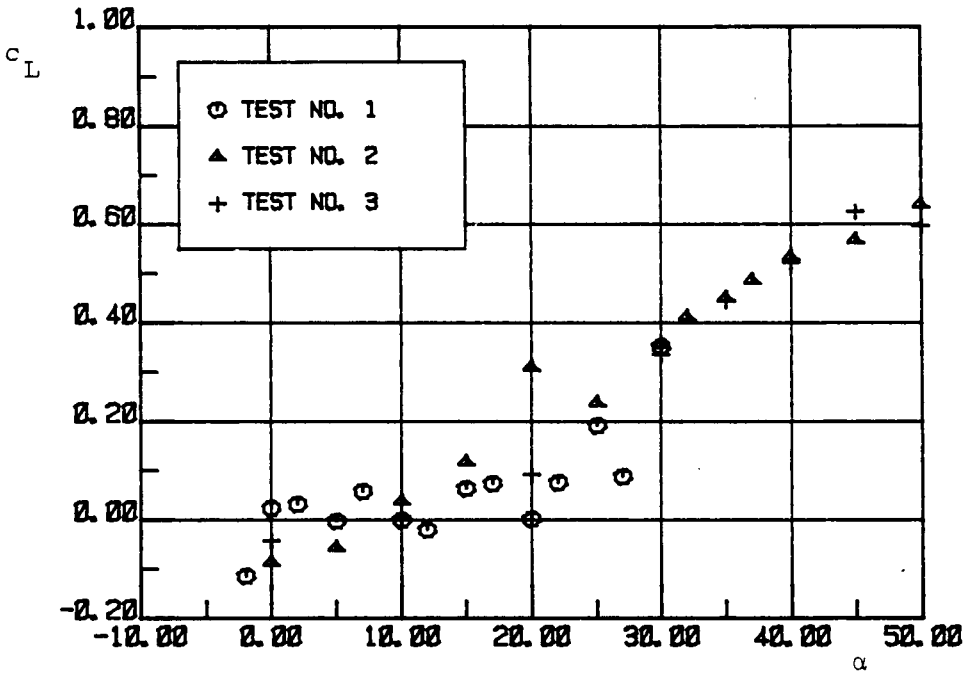


Figure B-3. Measured Lift of Model II at 10.7 m/s.

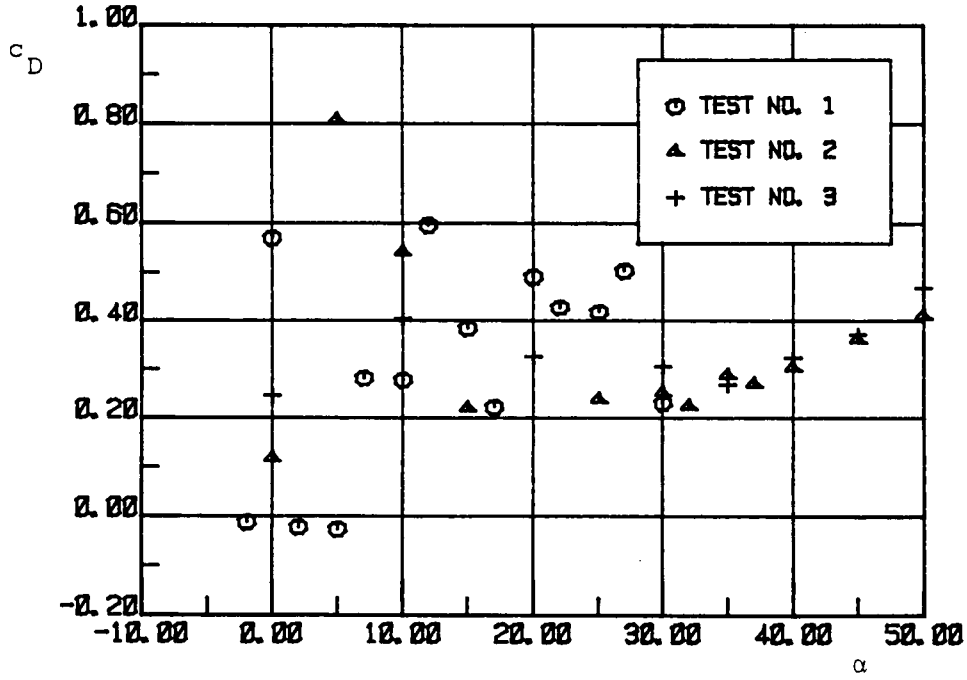
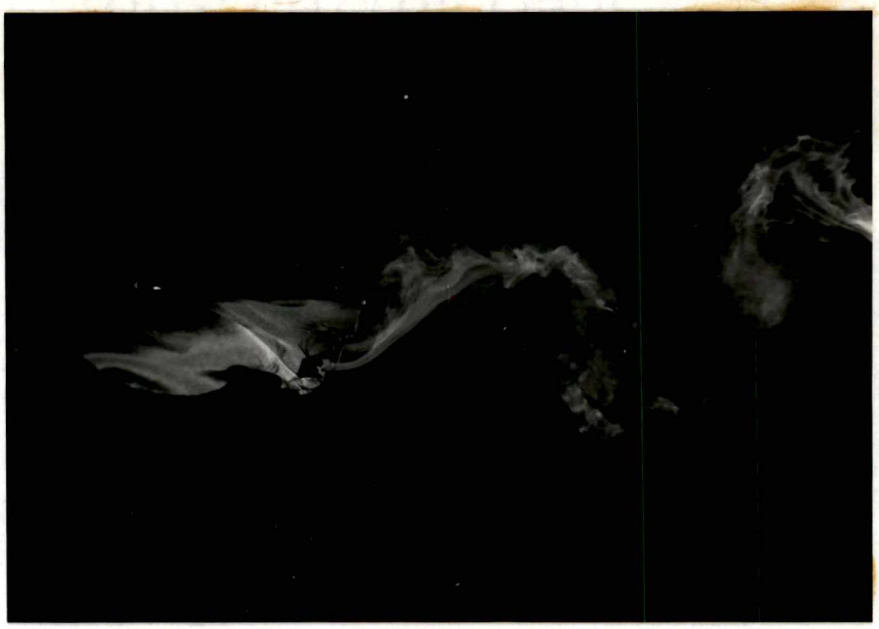
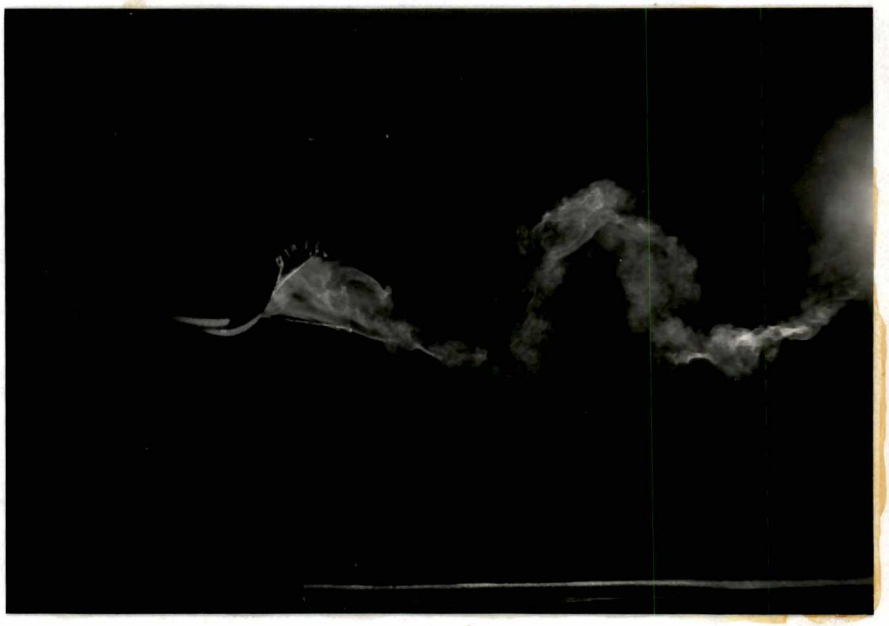


Figure B-4. Measured Drag of Model II at 10.7 m/s.



$\alpha = 0°$

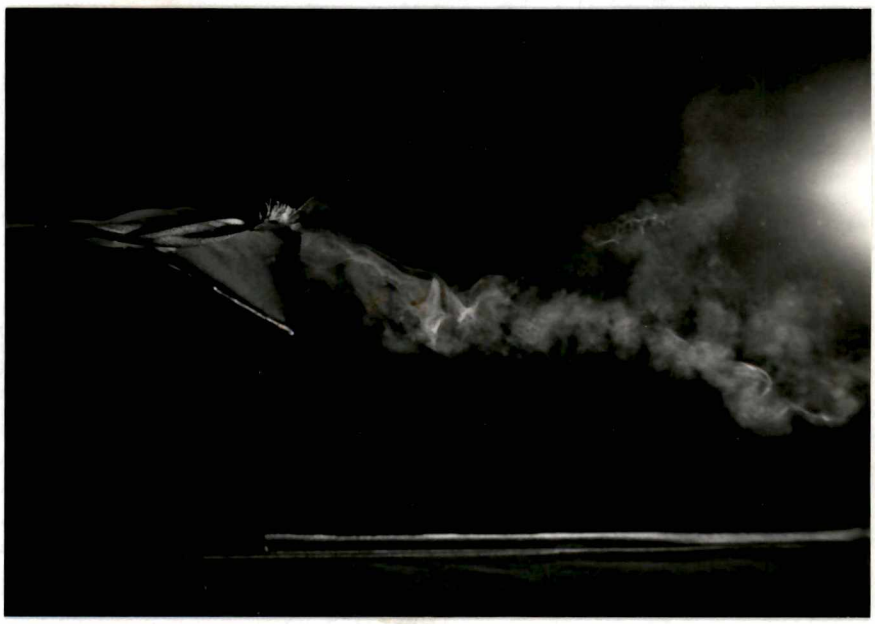


$\alpha = 10°$

Figure B-5. Flow Field of Model II.

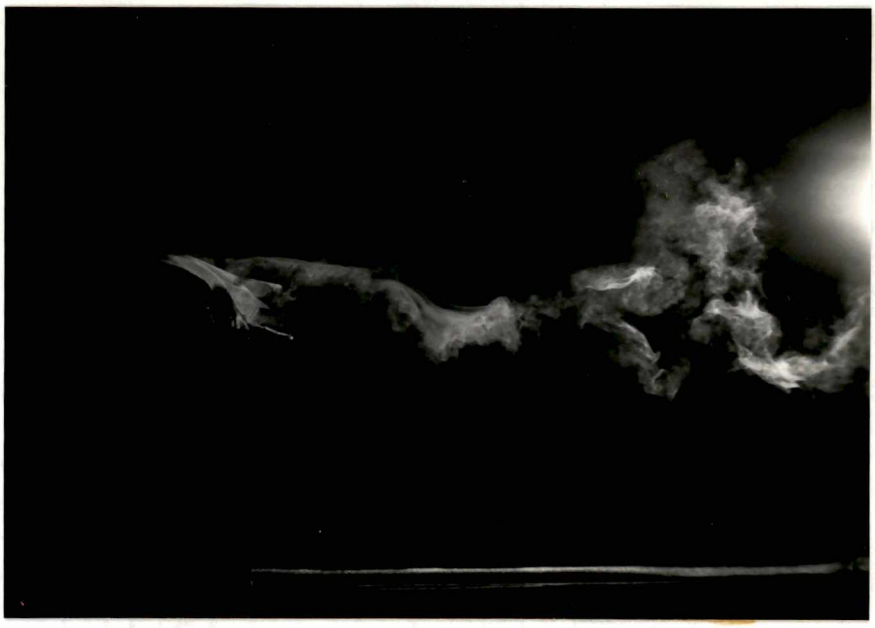


$\alpha = 25°$



$\alpha = 30°$

Figure B-5 (continued)



$\alpha = 40°$



$\alpha = 45°$

Figure B-5 (continued)

APPENDIX C

RESULTS OF MODEL III

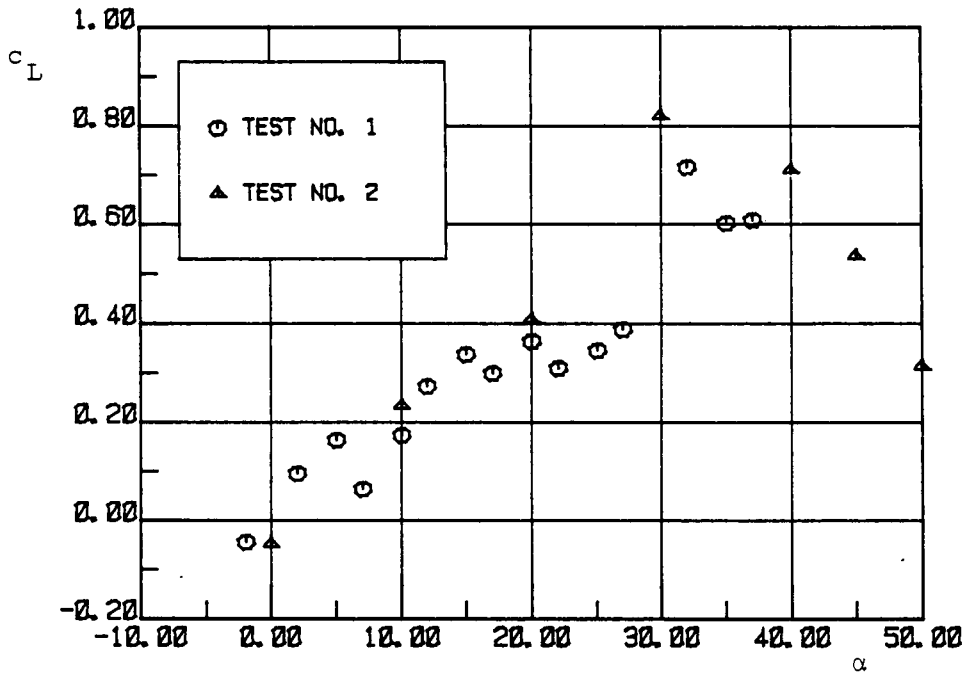


Figure C-1. Measured Lift of Model III at 9.1 m/s.

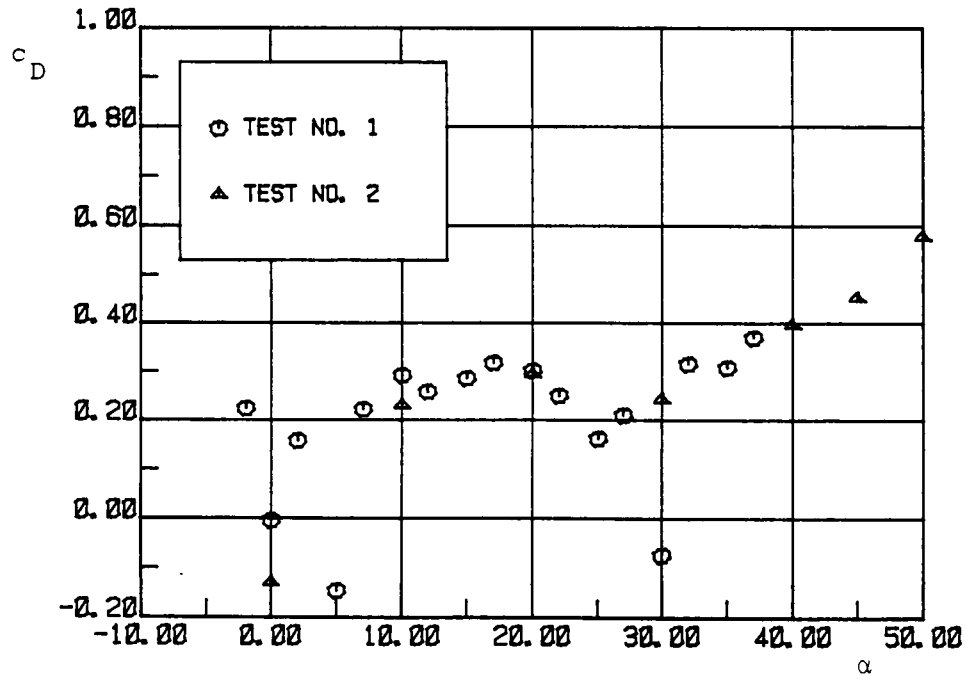


Figure C-2. Measured Drag of Model III at 9.1 m/s.

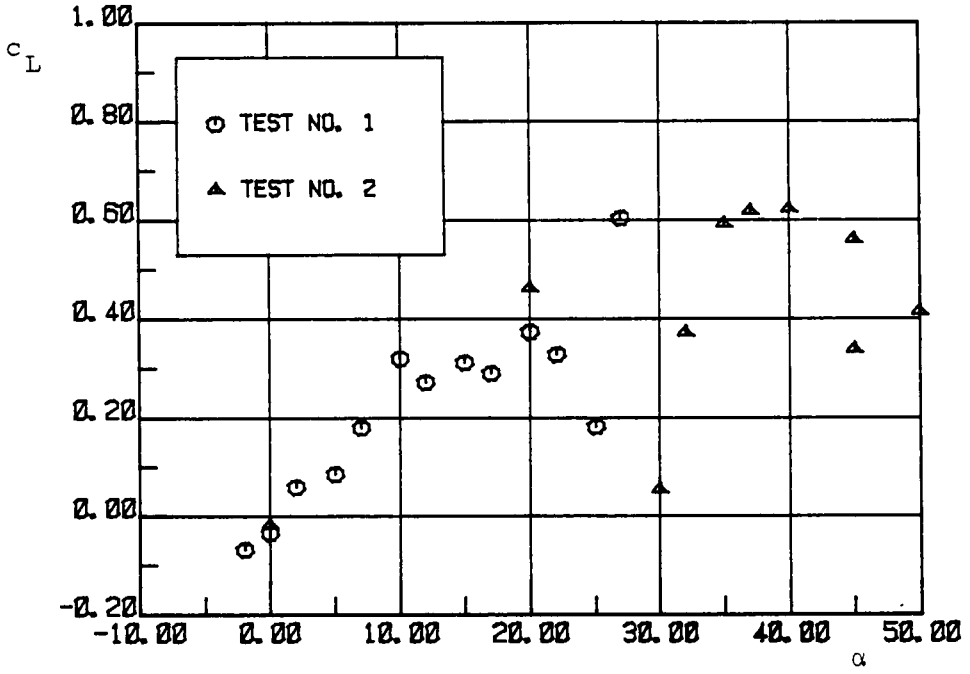


Figure C-3. Measured Lift of Model III at 10.7 m/s.

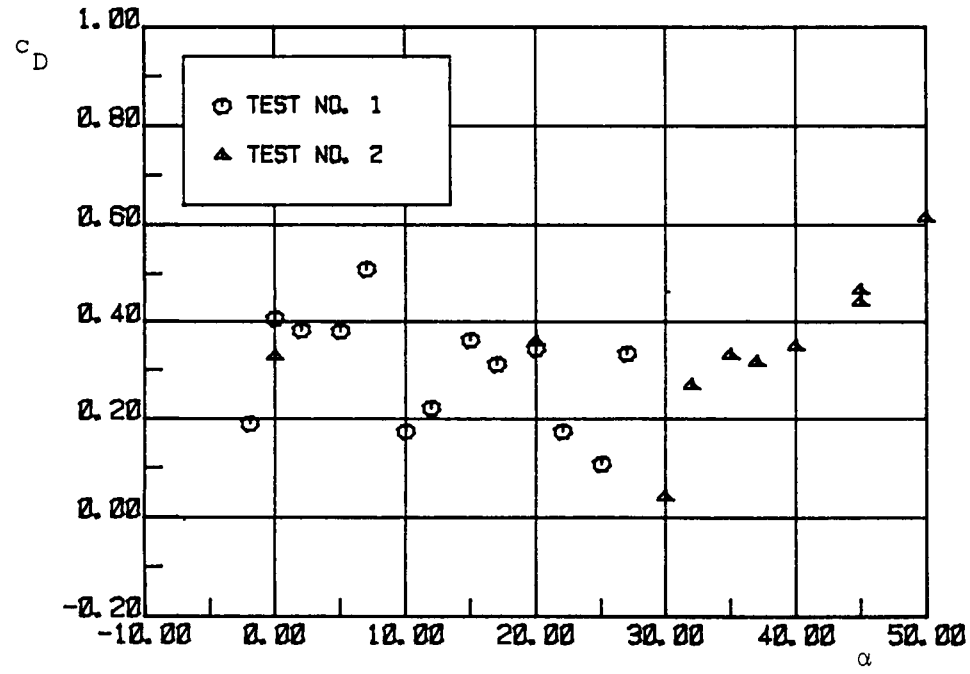
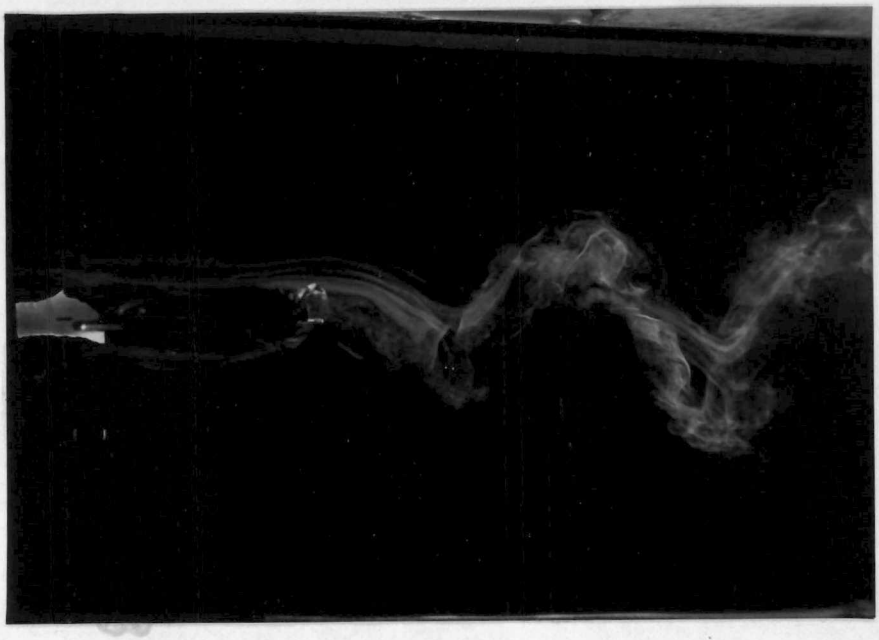
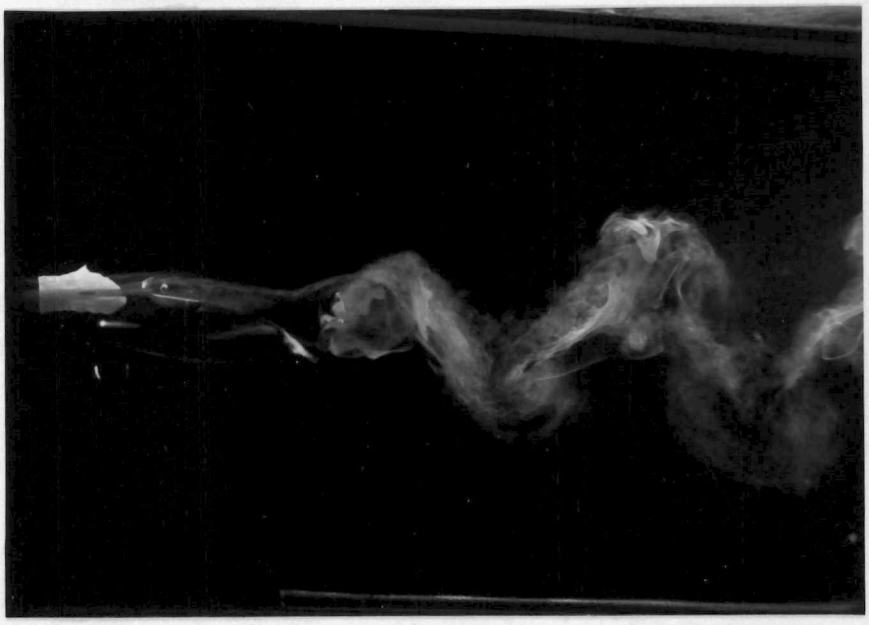


Figure C-4. Measured Drag of Model III at 10.7 m/s.



$\alpha = 0°$

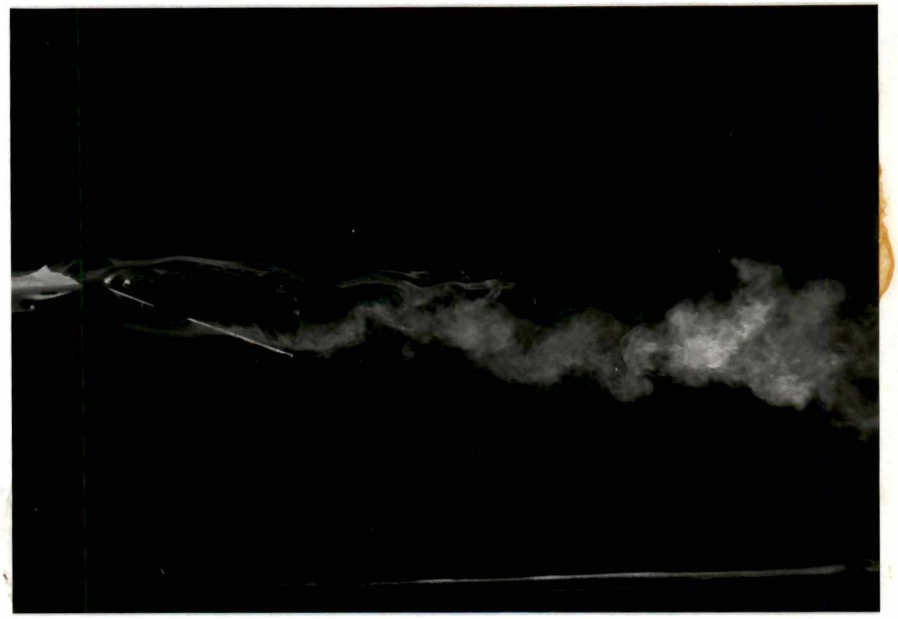


$\alpha = 5°$

Figure C-5. Flow Field of Model III.

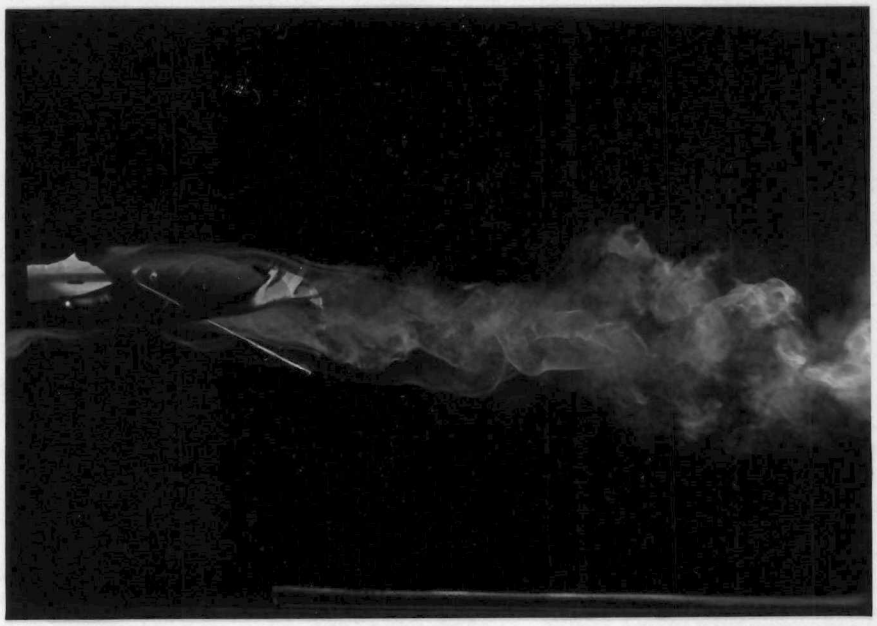


$\alpha = 10°$



$\alpha = 20°$

Figure C-5 (continued)

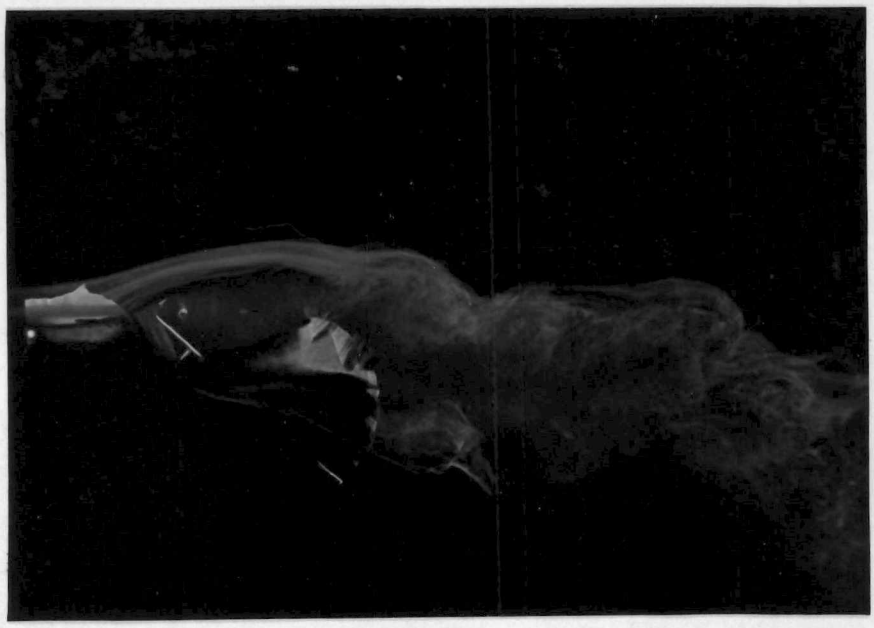


$\alpha = 25°$

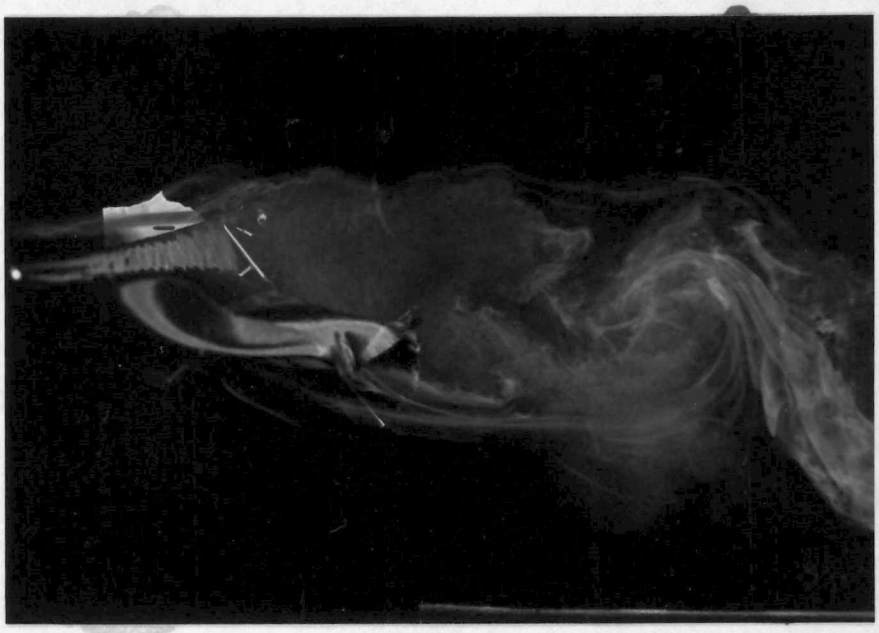


$\alpha = 30°$

Figure C-5 (continued)



$\alpha = 40°$



$\alpha = 50°$

Figure C-5 (continued)



$\alpha = 55°$



$\alpha = 60°$

Figure C-5 (continued)

APPENDIX D

RESULTS OF MODELS IV AND V

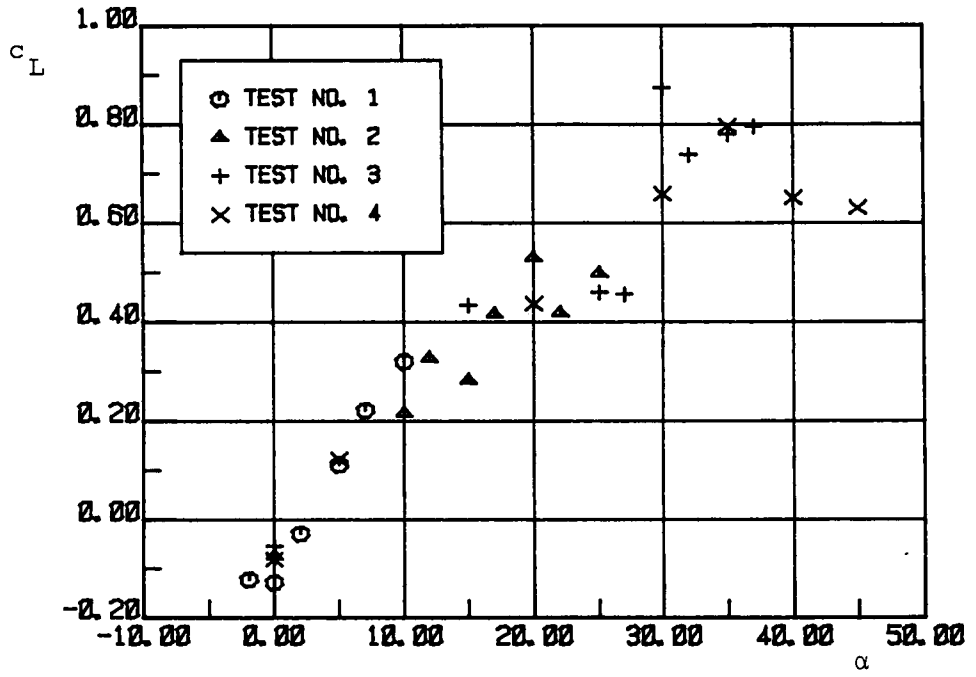


Figure D-1. Measured Lift of Model IV at 9.1 m/s.

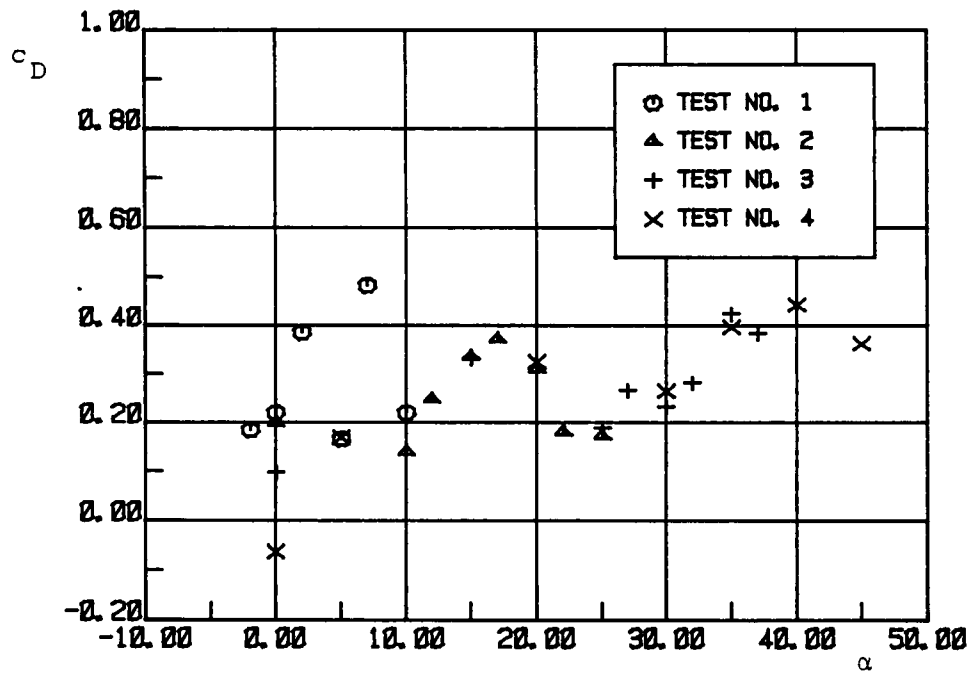


Figure D-2. Measured Drag of Model IV at 9.1 m/s.

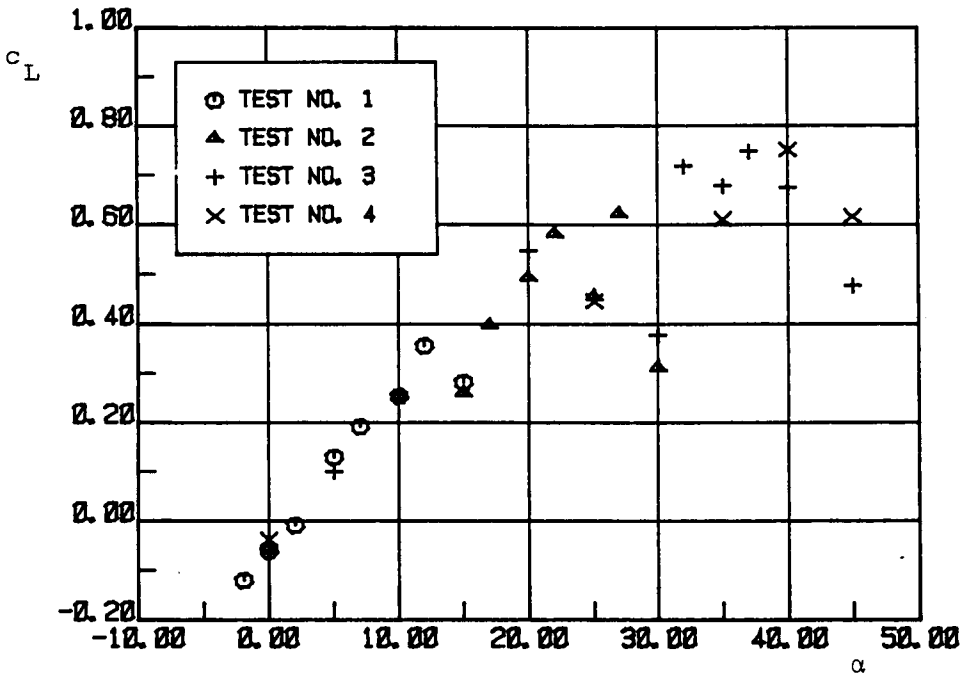


Figure D-3. Measured Lift of Model IV at 10.7 m/s.

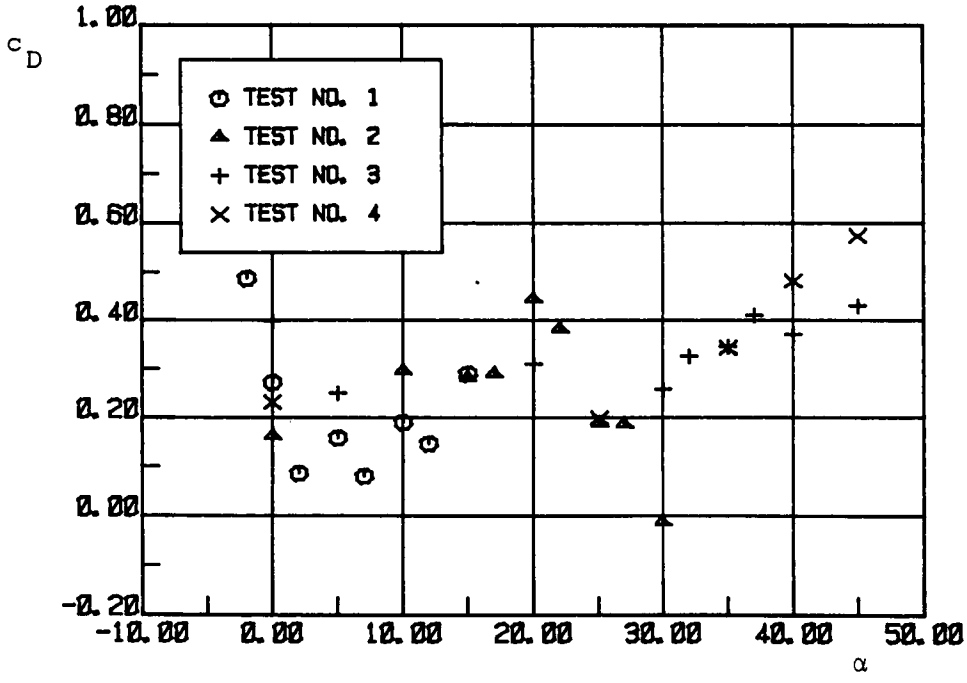
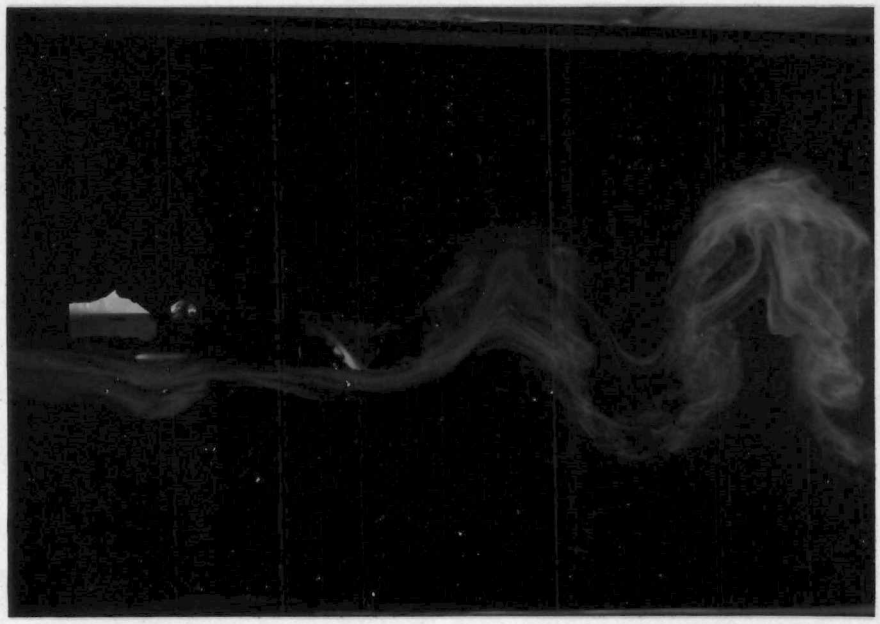
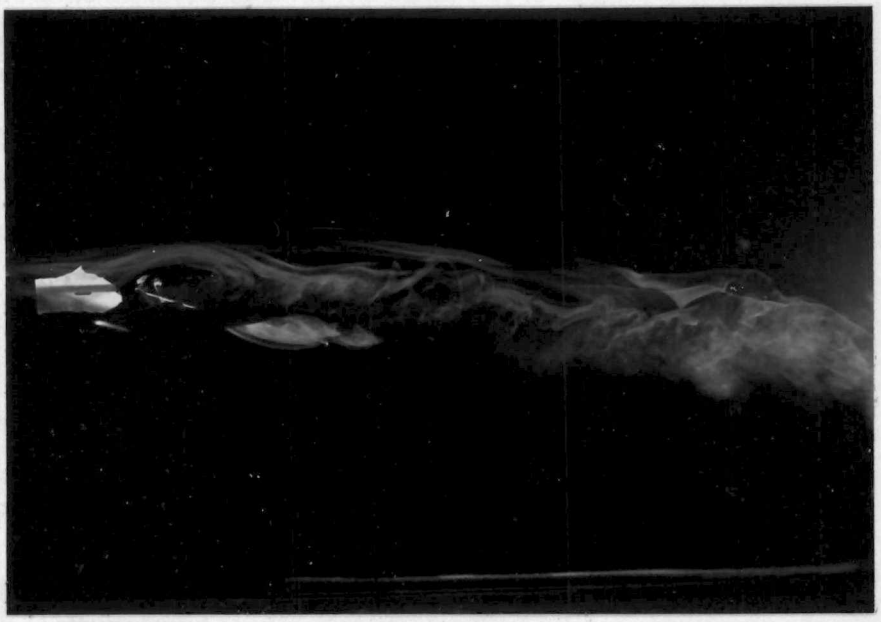


Figure D-4. Measured Drag of Model IV at 10.7 m/s.



$\alpha = 0°$



$\alpha = 15°$

Figure D-5. Flow Field of Model IV.

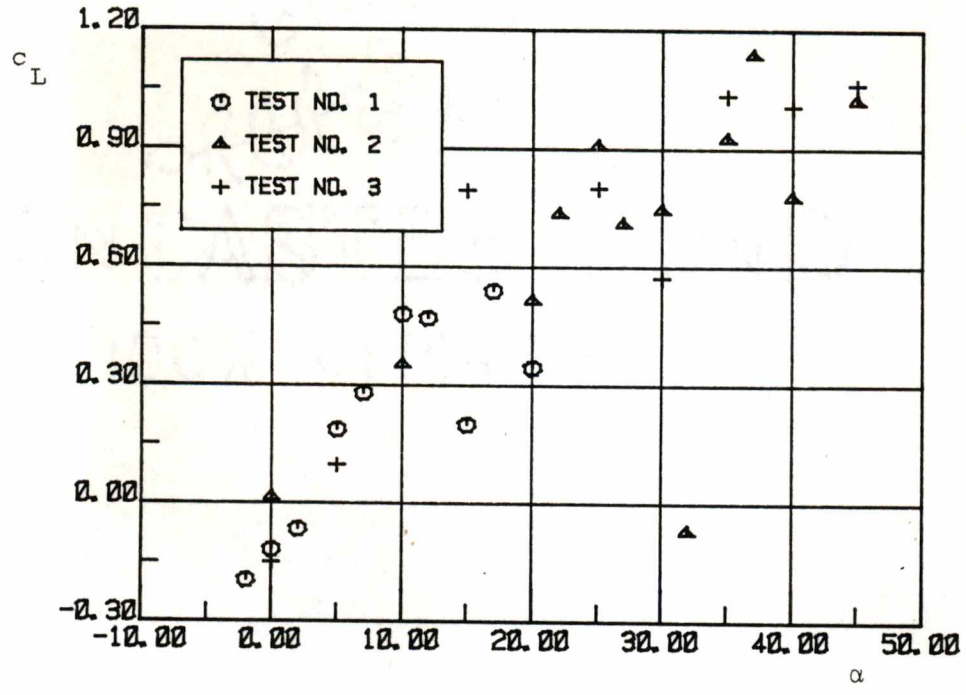


Figure D-6. Measured Lift of Model V at 9.1 m/s.

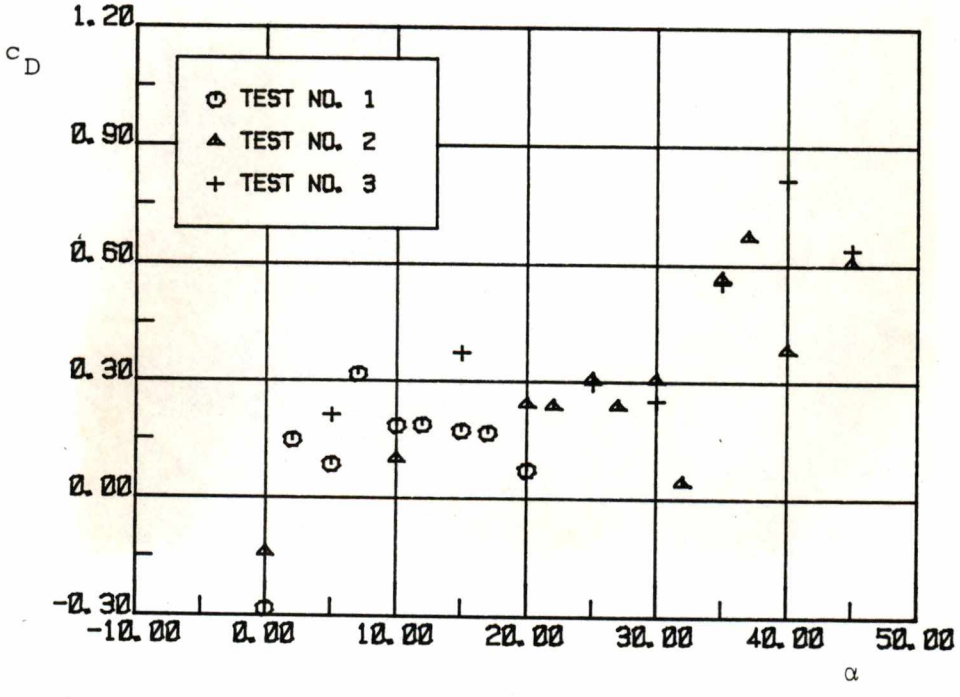
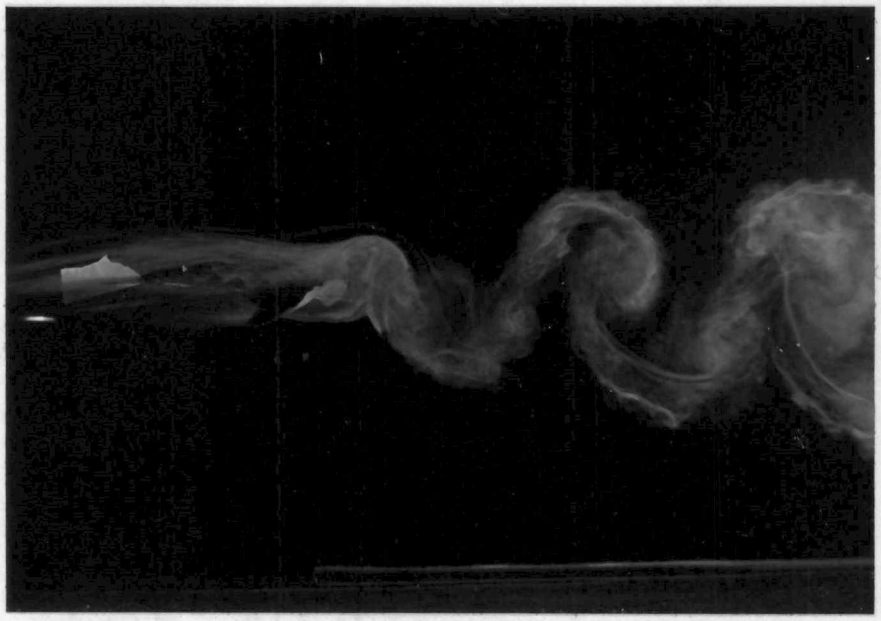


Figure D-7. Measured Drag of Model V at 9.1 m/s.

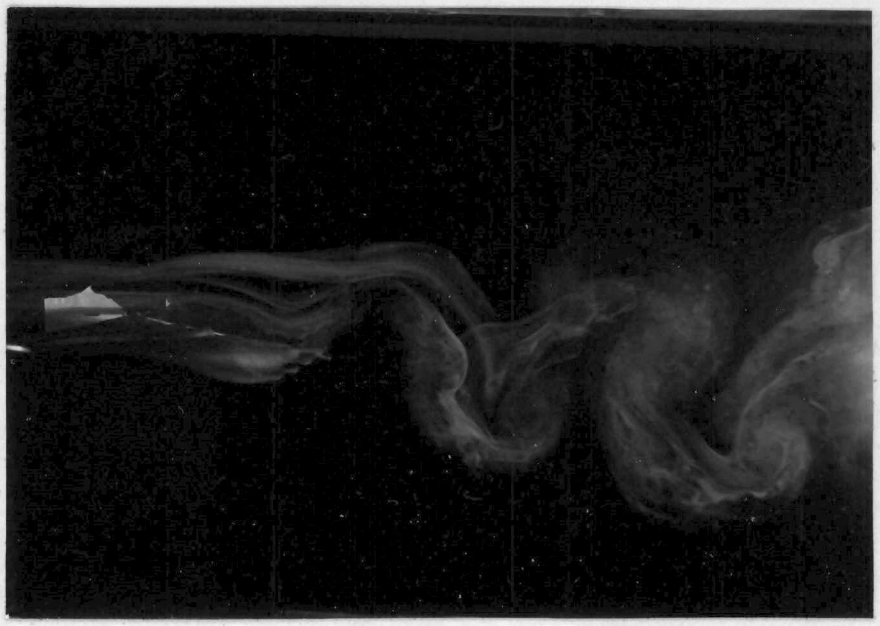


$\alpha = 0°$

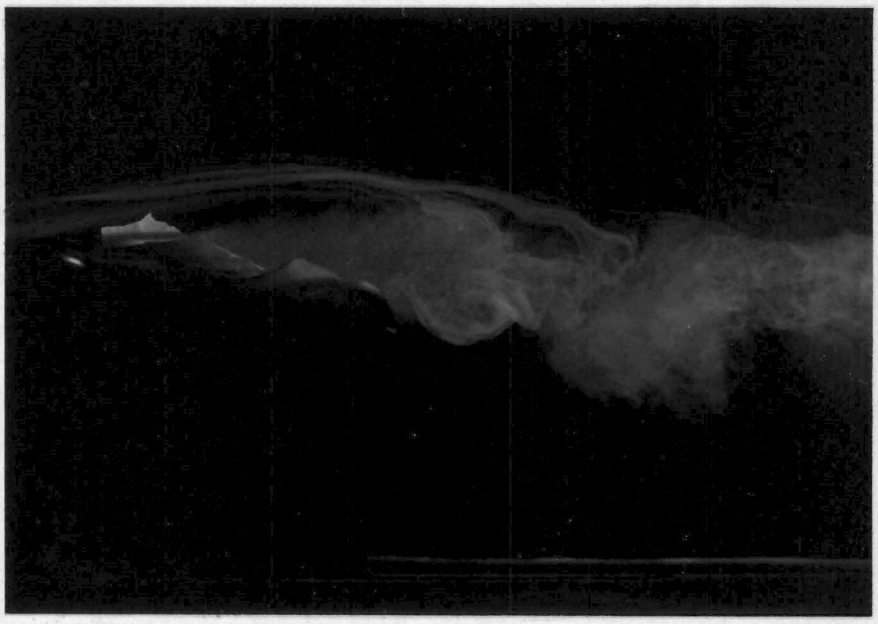


$\alpha = 5°$

Figure D-8. Flow Field of Model V.



$\alpha = 10°$



$\alpha = 25°$

Figure D-8 (continued)

VITA

Thomas Andreas Tietz was born in Trier, Germany, on July 2, 1960. He attended elementary school in Düsseldorf and was graduated from the Städtische Görresgymnasium in that city in May 1979. He then attended the Technical University of Aachen and was awarded the degree "Diplom-Ingenieur" in Mechanical Engineering in October 1984. In fulfillment of the requirements for this degree, he worked at the SNECMA, France, and in several other companies in the industry. Furthermore, he took part in an exchange program with the Queen's University of Belfast, Northern Ireland.

In the fall of 1984, he entered The University of Tennessee Space Institute, Tullahoma, Tennessee, as a Graduate Research Assistant and studied as a full-time student towards his Master's degree in Aerospace Engineering. This degree was awarded in March 1986.